Tropical atmospheric circulation changes under global warming

Dissertation
zur Erlangung des Doktorgrades
der Mathematisch-Naturwissenschaftlichen Fakultät
der Christian-Albrechts-Universität zu Kiel
vorgelegt von

Dipl.-Met.
Tobias Bayr

September 2013

Maritime Meteorology
GEOMAR Helmholtz Centre for Ocean Research Kiel

Referent: Prof. Dr. Mojib Latif
Koreferent: Dr. Dietmar Dommenget

Tag der mündlichen Prüfung: 22. November 2013
Zum Druck genehmigt: 22. November 2013

gez. Prof. Dr. Wolfgang J. Duschl, Dekan

Für Nobody

This is a story about four people
named Everybody, Somebody, Anybody, and Nobody,
and about climate conferences.
There was an important job to be done
and Everybody was sure that Somebody would do it.
Anybody could have done it, but Nobody did it.
Somebody got angry about that,
because it was Everybody's job.
Everybody thought Anybody could do it,
but Nobody realized that Everybody wouldn't do it.
It ended up that Everybody blamed Somebody
when Nobody did what Anybody could have done.

Contents

Zusammenfassung

Die vorliegende Dissertation besteht aus drei wissenschaftlichen Publikationen. In der ersten Publikation werden die Veränderungen des Luftdrucks auf Meeresniveau (SLP) im anthropogenen Klimawandel in einem Multimodell Ensemble (MMEns) aus Klimamodellen der dritten Phase des Coupled Model Intercomparison Project (CMIP3) und in ERA Interim Reanalysedaten untersucht. Wir folgen dabei der Idee, das Erwärmungssignal in einen räumlich homogenen und räumlich inhomogenen Anteil aufzuteilen. Obwohl die inhomogene Erwärmung ungefähr zehnmal kleiner ist als die homogene, sind die Veränderungen im tropischen SLP stark mit der inhomogenen Erwärmung der troposphärischen Temperatur (T_{tropos}) verknüpft. Dieser starke Zusammenhang kann mit dem Bjerknes Zirkulations Theorem erklärt werden: zwischen einer warmen und einer kalten Luftsäule entsteht in den Tropen aufgrund der geringen Corioliskraft eine nahezu direkte Zirkulation, mit aufsteigender Luft und niedrigem Luftdruck in der warmen Luftsäule und absinkender Luft und hohem Luftdruck in der kalten Luftsäule. Die unterschiedlich starke Erwärmung von Land und Ozean dominiert die inhomogene T_{tropos} Erwärmung im Klimawandel. Die Veränderungen im SLP zeigen durch die starke Verknüpfung mit T_{tropos} auch einen ausgeprägten Land-Ozean Kontrast, mit sinkendem SLP über Südamerika und Afrika und steigendem SLP über dem Indo-Pazifik. Diese Ergebnisse konnten in einem idealisierten Sensitivitätsexperiment bestätigt werden. Die Trends des SLP und T_{tropos} in ERA Interim zeigen im Zeitraum von 1989 bis 2010 ebenfalls einen starken Zusammenhang. Allerdings ist hier der Land-Ozean Kontrast nicht der dominante Antrieb der T_{tropos} Erwärmung, so dass die Trends in diesem Zeitraum vermutlich durch natürliche Variabilität verursacht wurden.

In dem zweiten Artikel wird eine Methode zum Vergleich räumlicher Variabilitätsmuster auf der Grundlage von Empirical Orthogonal Function (EOF) Moden vorgestellt. Diese Methode nennt sich Distinct Empirical Orthogonal Function (DEOF) Analyse und eignet sich, um den Unterschied in den Mustern der Variabilität zwischen z.B. vergangenem und zukünftigem Klima oder Beobachtungen und Modellen herauszufinden. Dabei wird die gesamte multivariate Struktur von zwei Datensätzen verglichen, um die Muster mit der größten Differenz in der erklärten Varianz zwischen den beiden Datensätzen zu bestimmen. Wir erläutern in wohldefinierten Beispielen wie diese Methode Veränderungen in den Moden der Variabilität (eine Verstärkung, eine Verlagerung oder ein multivariate Veränderung) darstellt. Desweiteren vergleichen wir unseren Ansatz mit Beispielen aus der Literatur. Dies umfasst die Veränderungen aufgrund des Klimawandels in den Variabiltätsmoden des atlantischen und europäischen SLP, des SLP der Südhemisphäre, der Oberflächentemperatur der Nordhemisphäre, der Meeresoberflächentemperatur im Nordpazifik und des Niederschlags über den tropischen Indo-Pazifik.

Der dritte Artikel befasst sich mit den Veränderungen der zonalen äquatorialen Zirkulation und ihrem bekanntesten Vertreter, der Walker Zirkulation, im Klimawandel. Diese Veränderungen untersuchen wir in einem MMEns aus CMIP3 und CMIP5 Klimamodellen. Die zonale Zirkulation schwächt sich im mittleren Zustand ab und die Walker Zirkulation verlagert

sich darüber hinaus nach Osten. Die Trends im Klimawandel haben eine ähnliche Struktur wie die mit dem El Nino Southern Oscillation (ENSO) Phänomen verbundene Variabilität und tatsächlich können zwei Drittel der Veränderungen der Walker Zirkulation mit dem Trend zu mehr El Nino ähnlichen Bedingungen erklärt werden. In Übereinstimmung mit dem Trend zu mehr El Nino ähnlichen Bedingungen und einer Nichtlinearität in der mit ENSO verbundenen Variabilität zeigen die Muster der Variabilität im Klimawandel eine ostwärtige Verlagerung des dominanten Modes. Die MMEns von CMIP3 und CMIP5 zeigen in fast allen Aspekten sehr ähnliche Ergebnisse. Dies unterstreicht die Robustheit der Ergebnisse. Die Trends in ERA Interim zeigen über den Zeitraum von 1979 bis 2012 eine westwärtige Verlagerung und Verstärkung der Walker Zirkulation, also im Gegensatz zu den CMIP MMEns einen Trend zu mehr La Nina ähnlichen Bedingungen. Hier können drei Viertel der Änderungen der Walker Zirkulation mit dem Trend im dominanten Mode der Variabilität erklärt werden. Auch wenn die Trends in den Beobachtungen und den Klimaprognosen sich in unterschiedliche Richtungen entwickeln, folgt in Beiden ein großer Teil des langfristigen Trends der Walker Zirkulation dem dominierenden Mode der internen Variabilität.

Abstract

This PhD thesis consists of three scientific articles. In the first one the tropical sea level pressure (SLP) response under global warming is investigated in a multi-model ensemble (MMEns) of climate models from the 3rd phase of the Coupled Model Intercomparison Project (CMIP3) and in ERA Interim reanalysis data. In this article we follow the idea to split up the tropical warming into a spatial homogeneous part and a spatial inhomogeneous part. Even though the inhomogeneous warming is roughly 10 times smaller than the homogeneous warming, the tropical SLP changes are strongly related to the inhomogeneous tropospheric temperature (T_{tropos}) changes under global warming. According to the Bjerknes Circulation Theorem, this strong relationship can be explained with a nearly direct circulation between a warmer and a colder air column, due to weak Coriolis force in the tropics, with rising air and low SLP in the warmer air column and sinking air and high SLP in the colder air column. The inhomogeneous T_{tropos} warming is dominated by the land-sea warming contrast. Also SLP trends show a land-sea contrast due to the strong link with T_{tropos}. It is charactericsed by a SLP decrease over South America and Africa and a SLP increase over the Indo-Pacific. This result is confirmed in an idealised sensitivity experiment. The trends of SLP and T_{tropos} in ERA Interim over the period from 1989 until 2010 are also strongly linked to each other, but here the land-sea warming contrast is not the dominant driver of T_{tropos} warming, indicating that the trends over the last decades are mostly due to internal variability.

The second article presents a method for comparing the spatial patterns of variability on the basis of Empirical Orthogonal Function (EOF) modes. This method is called Distinct Empirical Orthogonal Function (DEOF) analysis and can be used to find differences in the patterns of variability e.g. between past and future climate or between models and observations. It compares the whole multivariate structure of two datasets and finds the patterns with the largest difference in explained variance between those. We illustrate in well-defined artificial examples how changes in the modes of variability (an intensification, a shift or a multivariate change) can be revealed with this method. Further we compare our approach with examples from the literature. This includes changes in the modes of variability under global warming in SLP over the North Atlantic and Europe, SLP of the Southern Hemisphere, surface temperature of the Northern Hemisphere, sea surface temperature of the North Pacific and precipitation in the tropical Indo-Pacific.

In the third article the changes in the equatorial zonal circulation cells, with its most prominent part the Walker Circulation, are investigated in a MMEns of CMIP3 and CMIP5 models under global warming. In the mean state we found a weakening of the zonal circulation cells as well as an eastward shift of the Walker cell. The global warming trend has a similar structure to the variability in zonal stream function that is associated with El Nino Southern Oscillation (ENSO). Indeed, two third of the Walker Circulation changes be explained by a trend towards more El-Nino-like conditions. Under global warming the modes of variability

show an eastward shift of the dominant mode, which is consistent with the El-Nino-like trend and a spatial non-linearity found in ENSO associated variability. The CMIP3 and CMIP5 MMEns show in nearly all aspects very similar results, which underlines the robustness of these results. The trends in ERA Interim reanalysis data over the period from 1979 to 2012 show a westward shift and a strengthening of the Walker Circulation, hence in contrast to the CMIP MMEns a trend towards more La-Nina-like conditions. The trend in dominant mode of variability can here explain three quarter of the Walker Circulation changes. Thus long-term trends of the Walker Circulation seem to follow, to a large part, the pre-existing dominant mode of internal variability.

Chapter 1

Introduction

Differences in the local temperature are an important driver of the atmospheric circulation, as the atmospheric circulation tries to balance the differences by heat transports. This can be observed on different spatial scales: on local scale in the land-sea breeze, on continental scale in the monsoonal circulation or on planetary scale in the large scale circulation like Hadley Circulation. The basic law which describes these circulations is the Bjerknes Circulation Theorem, that was already described in *Bjerknes et al.* (1898) and points out a contrary relation between temperature and pressure. Due to a weak coriolis force in the tropics, heating at one place and cooling at another will induce a nearly direct circulation, with rising air and low pressure at the heat source and descending air and high pressure at the heat sink.

The large scale circulation in the tropics is a thermal direct circulation and can be split up in the meridional Hadley Circulation cells and the zonal circulation cells, whose most prominent part is the Walker Circulation. The meridional Hadley Circulation is driven by the temperature contrast between the tropics and the higher latitudes whereas the zonal circulation cells are driven by the land-sea distribution and the zonal differences in the sea surface temperature: As land heats stronger than the ocean the three main convection regions in the tropics are located over Africa, the Maritime Continent and South America. The air descends over the nearby oceans, particularly strong over the cold coastal upwelling regions.

Mean state and variability of the atmospheric circulation in the tropics are important for the precipitation distribution within the tropics and have therefore a large socio-economical impact. It is of great interest how the tropical circulation will respond to global warming. *Knutson and Manabe* (1995) indicate two mechanisms for the changes of the tropical large scale circulation. The first mechanism works with a spatial homogeneous warming that increases with height. Under global warming the enhanced hydrological cycle causes such a warming: With increasing temperature the atmosphere can take up more water vapour following the Clausius-Clapeyron-Equation. As in the tropics nearly all of the water vapour is rained out, the additional latent heat release warms the atmosphere, strongest around the 250hPa level (*Held*, 1993), which increases the static stability (see Fig. 1.1). This mechanism was further investigated by *Held and Soden* (2006) and *Vecchi and Soden* (2007) and acts to weaken the tropical circulations in a warmer climate.

The second mechanism works with the spatial inhomogeneous warming and can, in general, weaken or strengthen the tropical circulations. Several factors can cause an inhomogeneous

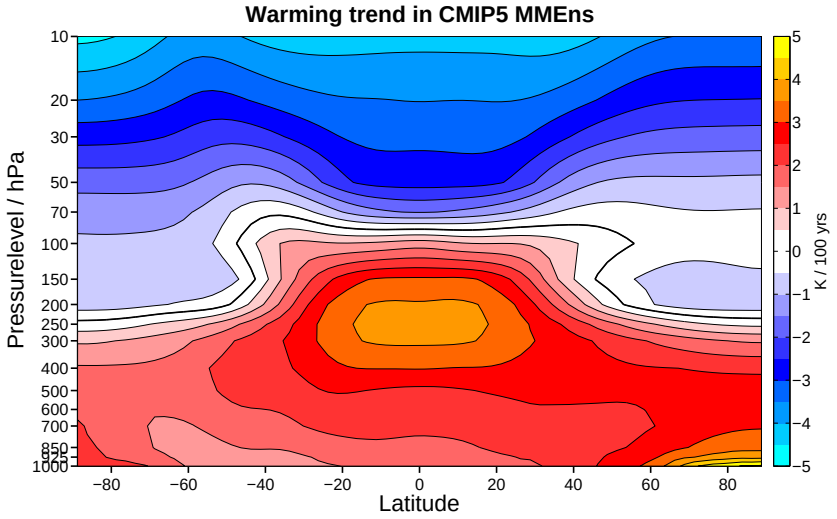

Figure 1.1: *Zonally averaged trend of atmospheric temperature in a multi-model ensemble of the 5th phase of the Coupled Model Intercomparison Project in the RCP4.5 scenario over the period from 1950 until 2099.*

warming, such as differences in evaporative cooling (*Knutson and Manabe*, 1995), the ocean dynamical thermostat (*Clement et al.*, 1996), the land-sea warming contrast (*Sutton et al.*, 2007) and cloud cover feedbacks (*DiNezio et al.*, 2009). In our work we follow this idea to split up the warming signal into the spatial homogeneous part and the spatial inhomogeneous part (see Fig. 1.2) to investigate their effects on the tropical circulations.

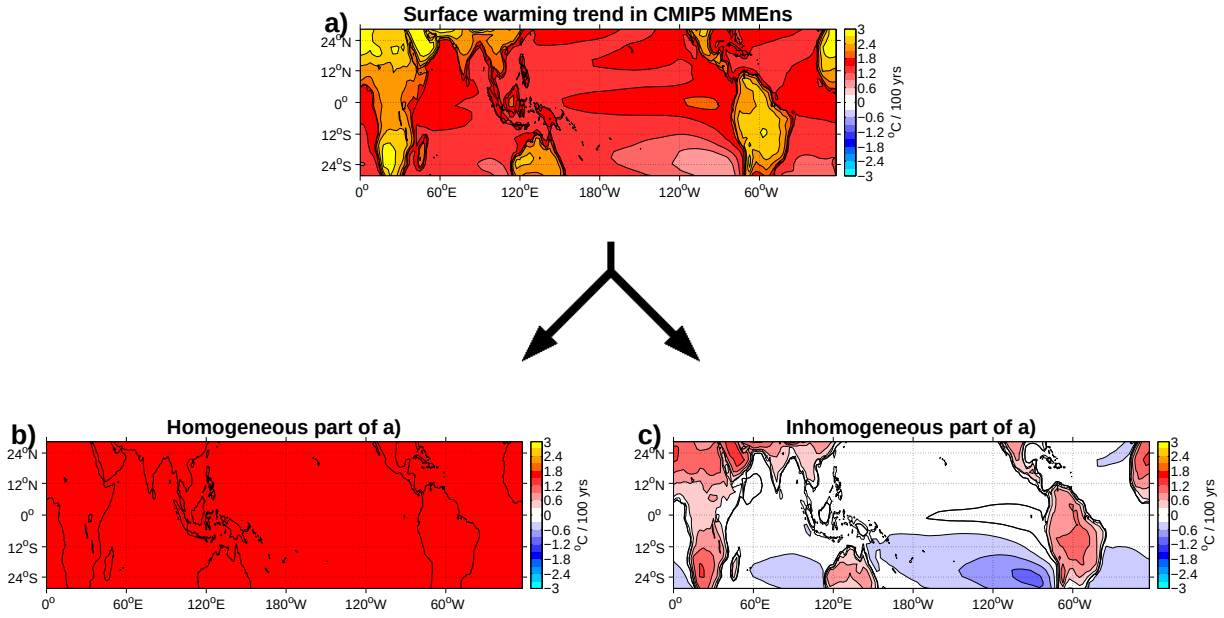

Figure 1.2: *Surface temperature trend in a multi-model ensemble of the 5th phase of the Coupled Model Intercomparison Project in the RCP4.5 scenario over the period from 1950 until 2099, (a) total warming, (b) homogeneous warming (area mean of (a)) and (c) inhomogeneous warming ((a) − (b)).*

The mean state and variability of sea level pressure (SLP) is one important indicator of the atmospheric circulation. In the recent years tropical SLP trends were discussed in the context of the expected weakening of the tropical circulation caused by the spatial homogeneous warming that increases with height (*Vecchi and Soden*, 2007). In chapter 2 the large scale pattern of the tropical SLP changes under global warming is discussed in a CMIP3 MMEns in relation to the inhomogeneous tropospheric warming. A strong relationship between the SLP trends and the inhomogeneous tropospheric warming is found, consistent with the Bjerknes Circulation Theorem. Further, it is shown that the land-sea warming contrast dominates the inhomogeneous tropospheric warming, and hence the large scale SLP response under global warming. A simple physical model is introduced, that can explain a large part of the large scale tropical SLP changes with the inhomogeneous tropospheric warming.

Climate variability is often organised in quasi-stationary spatial patterns, also called modes of variability. Changes in these modes of variability under global warming can have large socio-economical impacts, thus are as important as changes in the mean state. In chapter 3 a method for comparing the spatial structure of variability in two datasets is presented, which can be used to identify the changes in the modes of variability under global warming. This method is called Distinct Empirical Orthogonal Function (DEOF) analysis and is a generalisation of the method introduced in *Dommenget* (2007). The method is illustrated on the basis of several well defined artificial examples and compared with results from the literature.

Chapter 4 presents an analysis about the global warming response of the zonal circulation cells and its most prominent part, the Walker Circulation. For the representation of the zonal circulation cells the zonal stream function is used. The focus of the analysis is on the eastward shift of the Walker Circulation under global warming and its relation to El Nino Southern Oscillation (ENSO) variability. Further, the non-linearity of the zonal stream function in ENSO variability is investigated and the changes of the modes of variability are analysed using the DEOF method described in chapter 3.

1.1 Multi-model ensemble

In the 3rd and 5th phase of the Coupled Model Intercomparison Project (CMIP3, *Meehl et al.*, 2007a and CMIP5, *Taylor et al.*, 2012) all climate model runs are collected that were carried out for the 4th and 5th assessment report (AR4 and AR5) of Intergovernmental Panel on Climate Change (IPCC, AR4: *Meehl et al.*, 2007b, AR5: will be published Januar 2014), respectively. We use multi-model ensembles (MMEns) of this broad data base of 24 models in CMIP3 and 36 models in CMIP5 for the analysis of climate change. Using a MMEns instead of a single climate model follows the basic idea of *Galton* (1907), who revealed that the average over many individual (biased) guesses is quite close to the true value. Indeed, *Reichler and Kim* (2008) found that in the CMIP3 data base the MMEns of all individual models represent the observed climate better than any individual climate model (see their Fig. 1). The model biases seem to average out in a MMEns. We therefore use a MMEns for analysing climate change predictions to base our results on a comprehensive ground.

Chapter 2

The Tropospheric Land-Sea Warming Contrast as the Driver of Tropical Sea Level Pressure Changes

This chapter is a reprint of the paper "The Tropospheric Land-Sea Warming Contrast as the Driver of Tropical Sea Level Pressure Changes" published in Journal of Climate.

Citation: Bayr, T., and Dommenget, D. (2013a), The Tropospheric Land–Sea Warming Contrast as the Driver of Tropical Sea Level Pressure Changes, Journal of Climate, 26(4), 1387–1402, doi:10.1175/JCLI-D-11-00731.1.

Abstract

This article addresses the causes of the large-scale tropical sea level pressure (SLP) changes during climate change. The analysis presented here is based on model simulations, observed trends and the seasonal cycle. In all three cases the regional changes of tropospheric temperature (T_{tropos}) and SLP are strongly related to each other (considerably stronger than (sea) surface temperature and SLP). This relationship basically follows the Bjerknes Circulation Theorem, with relatively low regional SLP where there is relatively high T_{tropos} and vice versa. A simple physical model suggests a tropical SLP response to horizontally inhomogeneous warming in the tropical T_{tropos}, with a sensitivity coefficient of about -1.7 hPa/K. This relationship explains a large fraction of observed and predicted changes in the tropical SLP.

It is shown that in climate change model simulations the tropospheric land-sea warming contrast is the most significant structure in the regional T_{tropos} changes relative to the tropical mean changes. Since the land-sea warming contrast exists in the absent of any atmospheric circulation changes it can be argued that the large-scale response of tropical SLP changes is to first order a response to the tropical land-sea warming contrast. Further, as land-sea warming contrast is mostly available moisture dependent, the models predict a stronger warming and decreasing SLP in the drier regions from South America to Africa and a weaker warming and increasing SLP over the wetter Indo-Pacific warm pool region. This suggests an increase in the potential for deep convection conditions over the Atlantic Sector and a decrease over the Indo-Pacific warm pool region in the future.

2.1 Introduction

The Fourth Assessment Report of the Intergovernmental Panel on Climate Change (IPCC) predicts a substantial global warming with a well-defined 3-dimensional spatial pattern in atmospheric temperatures for future anthropogenic climate change. How the tropical sea level pressure (SLP) and atmospheric circulation changes in response to these atmospheric temperature changes is the focus of this study.

The atmospheric temperature response to increasing greenhouse gas concentrations in the tropics has two important large-scale features: a vertical increase in warming of the troposphere and a land-sea warming contrast. The vertical increase in warming in the tropical troposphere is associated with the enhanced hydrological cycle (*Held*, 1993; *Held and Soden*, 2006) and is accompanied by a weakening of the large-scale tropical circulation (*Vecchi et al.*, 2006; *Vecchi and Soden*, 2007; *Vecchi et al.*, 2008). The second feature, which is not restricted to the tropical regions, is the marked land-sea contrast of surface and low-level warming, i.e. a (stronger) heating over land relative to the oceans. This is not just a transient effect caused by difference heat capacities of land and oceans, but is due to differences in feedbacks related to the available moisture (*Sutton et al.*, 2007; *Joshi et al.*, 2008; *Dommenget*, 2009).

How land-sea contrast is generated is illustrated in *Joshi et al.* (2008): Above a certain level in the middle troposphere the warming is more or less horizontal uniform due to a strong mixing of these air masses (see also Fig. 2.1a upper levels). Below this level, local feedbacks dominate the lapse rate and the warming. Due to more available latent heat the lapse rate is lower where the moisture content is higher and vice versa, with the dry adiabatic lapse rate as upper boundary. Thus starting at the same temperature in the middle troposphere and following a moisture dependent adiabat we yield a higher surface temperature at drier air columns and lower surface temperature at wetter air columns. Available moisture is limited over land, so that we get in general a stronger warming over land than over ocean, thus a land-sea warming contrast. Thus the terminology "land-sea contrast" can be a little bit misleading, because it is mostly an "available moisture contrast".

Important aspects of land-sea warming contrast are shown in Figure 2.1a: In the vertical it is most pronounced near the surface and in the horizontal it is strongest over the arid subtropical land masses. In the layer from 850 to 500 hPa the dry trade wind inversions over the East Atlantic and East Pacific warm nearly as strong as the dry air over the subtropical land masses. The humid Maritime Continent has only a weak land-sea contrast at surface and no land-sea contrast in the lower troposphere. These two features become clearer in Figure 2.1b: The Maritime Continent cools above the lowest levels more ocean-like and the Atlantic warms above the lowest levels more land-like. The upper boundary of the land-sea warming contrast varies over the individual oceans and continents (in agreement with *Joshi et al.*, 2008), while in the tropical wide perspective it is at the 400 hPa level (Fig. 2.1b). In summary it is quite obvious in this figure that horizontal differences in the warming of each tropospheric level relative to the level's mean warming are highest in the lower levels, which are strongest affected by the land-sea warming contrast. Since horizontal temperature gradients are one of the main drivers of the longitudinal atmospheric circulation cells, it seems plausible that the land-sea warming contrast could be an important driver of tropical circulation and SLP changes. For example *Bala et al.* (2011) show that an artificial land-sea warming contrast due to geo-engineering enhances the uplift and decreases the SLP over tropical land masses.

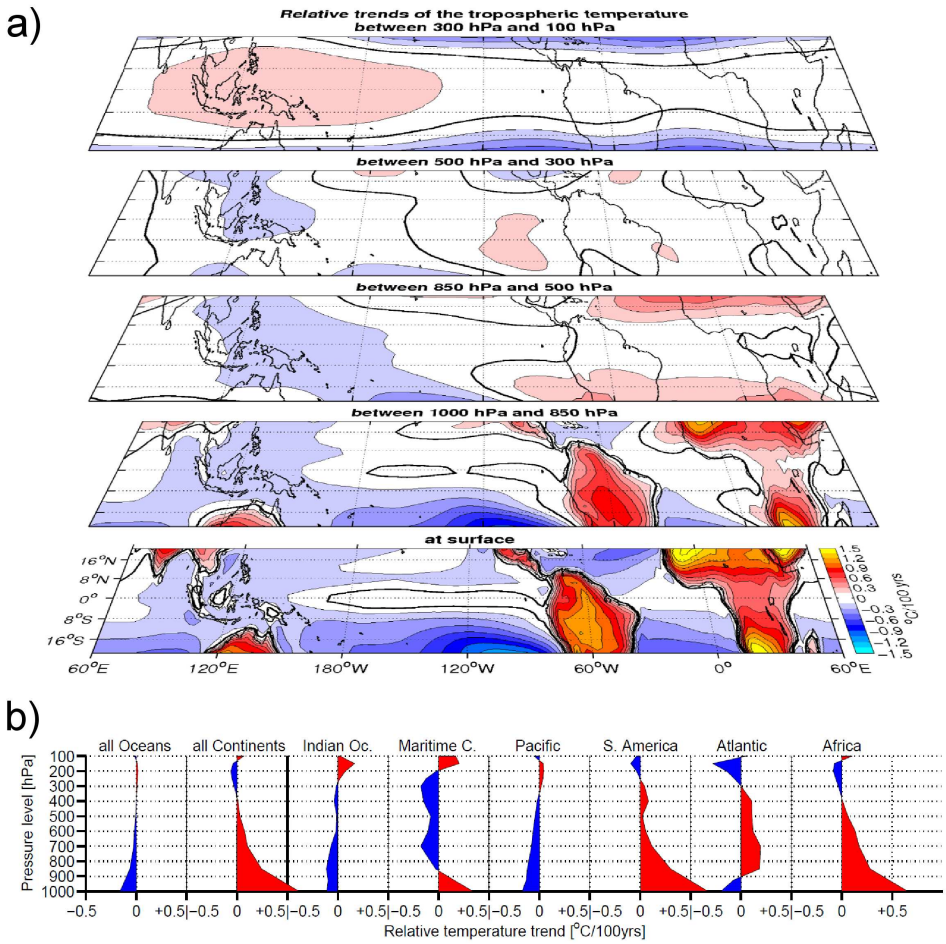

Figure 2.1: *(a) Linear trend of IPCC multi-model ensemble for the period 1970 to 2099 for tropospheric temperature at surface and for layers from 1000 to 850 hPa, 850 to 500 hPa, 500 to 300 hPa and 300 to 100 hPa; area mean trend of 2.4°C/100 yr, 2.6°C/100 yr, 3.0°C/100 yr, 4.2°C/100 yr and 4.6°C/100 yr respectively (from bottom to top) removed; (b) as in (a) but here the vertical profile averaged over the named oceans and continents between 23°S and 23°N.*

In general there is an important contrary relationship between temperature and SLP. This can be observed in monsoon circulation and land-sea breeze and is described by the Bjerknes Circulation Theorem: Heating at one place and cooling at the other will induce a nearly direct circulation, with rising air and low SLP at the heat source and sinking air and high SLP at the heat sink (e.g. *Bjerknes et al.*, 1898; *Gill*, 1980; *Thorpe et al.*, 2003), assuming that in the tropics the Coriolis force can be neglected. On regional scales previous studies (e.g. *Hu et al.*, 2000) found that this relationship can explain the intensification of the Asian monsoonal circulation by the land-sea warming contrast.

We can now do a first simple thought experiment: We know that there are the three relatively warm places in the tropics (Indo-Pacific warm pool region, South America and Africa), where the main deep convection takes place and SLP is low (*Krueger and Winston*, 1974). We also know, that in climate change projections due to land-sea warming contrast two of the three warm places (Africa and South America) warm stronger than the third one (Indo-Pacific warm

pool region, see Fig. 2.1), because highly available moisture reduces the warming there. Having the Bjerknes Circulation Theorem in mind we would expect from this little thought experiment that on large scale the SLP will increase over the warm pool region and decrease over Africa and South America, if land-sea warming contrast is the dominant feature in the SLP trends.

In recent years the tropical SLP response in a warmer climate was often discussed in the context of the weakening of the tropical circulations over the Pacific region, thus also on a more regional than global scale. Since the land-sea warming contrast acts on a global scale the question arises, if the large scale SLP response in the tropics can be explained with the land-sea warming contrast?

To describe this relationship between temperature and SLP as precisely as possible the temperature information of the atmosphere and not only of the surface is important, as indicated by the integration along the circulation path in the Bjerknes Circulation Theorem and stated in *Flohn* (1975). Further, considering only changes in surface temperature neglects the potentially important effect of the land-sea warming contrast in the troposphere. As we will see in the results section the SLP response in a warmer climate can be described considerably better if the temperature change over the full tropospheric circulation domain is considered, thus from surface to tropopause.

The focus of this study is to investigate the link between tropospheric temperature (T_{tropos}) and SLP changes in climate model simulations of future climate change simulations and in observations. We aim to present a simple physical model that can explain a large fraction of the large-scale response of the tropical SLP in a warming climate. The paper is organised as follows: Section 2.2 gives an overview of the data used in this study. This is followed by the first analysis in Section 2.3, in which we investigate the relation between T_{tropos} and SLP in the mean seasonal cycle to establish the link between T_{tropos} and SLP. In Section 2.4 a simple physical model for the tropical SLP response is introduced that quantifies the linear relation between T_{tropos} and SLP. The T_{tropos} and SLP trends of a climate change multi-model ensemble are examined in Section 2.5 and 2.6. The model simulation analysis is complemented by an idealised land-sea contrast experiment in Section 2.7 and the trends in observations are investigated in Section 2.8. We conclude our analysis with a summary and discussion in Section 2.9.

2.2 Data

Observed atmospheric temperatures and SLP are taken from the ERA Interim reanalysis (*Simmons et al.*, 2007) for the available period from 1989 to 2010. Over this period, the tropical temperature trends are in good agreement with satellite observations (*Bengtsson and Hodges*, 2009). We assume that the reanalysis products are the best estimates of observed tropospheric temperatures for this study, in particular due to the lack of sufficient coverage of "real" observations for the vertical air temperature profile.

The future climate change simulation data used are from 23 coupled model simulations of the Climate Model Intercomparison Project 3 (CMIP3) data base (*Meehl et al.*, 2007a). We took all simulations from the CMIP3 data base which have atmospheric temperature and SLP for the IPCC 20C and A1B scenario available, interpolated all data on a regular 2.5° x 2.5° grid and calculated a multi-model ensemble mean with one ensemble member from each model.

Missing atmospheric temperature values due to topography are interpolated from the levels above, following a moist adiabatic temperature profile.

Additionally we analyzed a set of sensitivity experiments with the ECHAM5 atmospheric general circulation model (*Roeckner et al.*, 2003) in T31 horizontal resolution (3.75° x 3.75°) coupled to a single column mixed layer ocean, as described in *Dommenget* (2009). We analyzed two 50 yr long sensitivity experiments in which the land surface temperatures with +1K and -1K differences from a reference climatology are prescribed; see *Dommenget* (2009) for details.

For all following analysis we defined the tropospheric temperature, T_{tropos}, as the vertical average of mass weighted air temperature from $1000hPa$ to $100hPa$, i.e. approximately the entire troposphere. The tropics are defined as the region from 23°N to 23°S.

2.3 The Seasonal Cycle of Tropical SLP and T_{tropos}

As a starting point for this study, we analyse the observed seasonal changes in tropospheric temperatures and SLP, as it provides a zero order estimate of the tropical circulation response to changes in tropospheric temperatures or to external forcing (incoming solar radiation in this case) in general. In Figure 2.2a-d we compare the seasonal mean T_{tropos} relative to the tropical total mean T_{tropos} with the seasonal mean SLP relative to the tropical total mean SLP. We can first of all note that the tropics have three regions of relative warm T_{tropos} over Africa, South America and the Indo-Pacific warm pool region (including Australia), which are also called the three main 'heat sources', where the main deep convection takes place (*Krueger and Winston*, 1974). These warm regions are separated by the cooler eastern Pacific and Atlantic and cooler regions towards higher latitudes. Following the seasonal cycle these regions shift mostly in north-south directions. More importantly in the context of this study we can see, that the patterns of relative T_{tropos} and SLP in all four seasons are highly anti-correlated with each other (Fig. 2.2a-d): The three main 'heat sources' in the tropics coincide with the regions of lowest SLP (*Matsuno*, 1966), as expected from the Bjerknes Circulation Theorem. The net mass exchange with the extra-tropics from season to season is small (despite the flow from summer to winter hemisphere), so that air masses redistribute mainly within the tropical band.

Another way of illustrating the strong relationship between relative T_{tropos} and relative SLP is to regress all four seasonal mean relative T_{tropos} values against the relative SLP for all grid points, as shown in Figure 2.3. The distribution indicates a clear linear relationship between relative T_{tropos} and relative SLP consistent with the above discussion. As a first measure of the relation, we obtain from a linear regression a -2.4 hPa change in SLP per 1 K warming in T_{tropos} in the seasonal cycle, which can explain 76% ($R^2 = 0.76$) of the SLP seasonal means with the T_{tropos} seasonal means.

2.4 A Simple Model for Tropical SLP Response to Changes in T_{tropos}

From simple physical considerations we can build a physical model to estimate the linear relationship between relative T_{tropos} and relative SLP in the tropics. Figure 2.4 illustrates how a regionally different warming of T_{tropos} can cause a mass redistribution and therefore a change

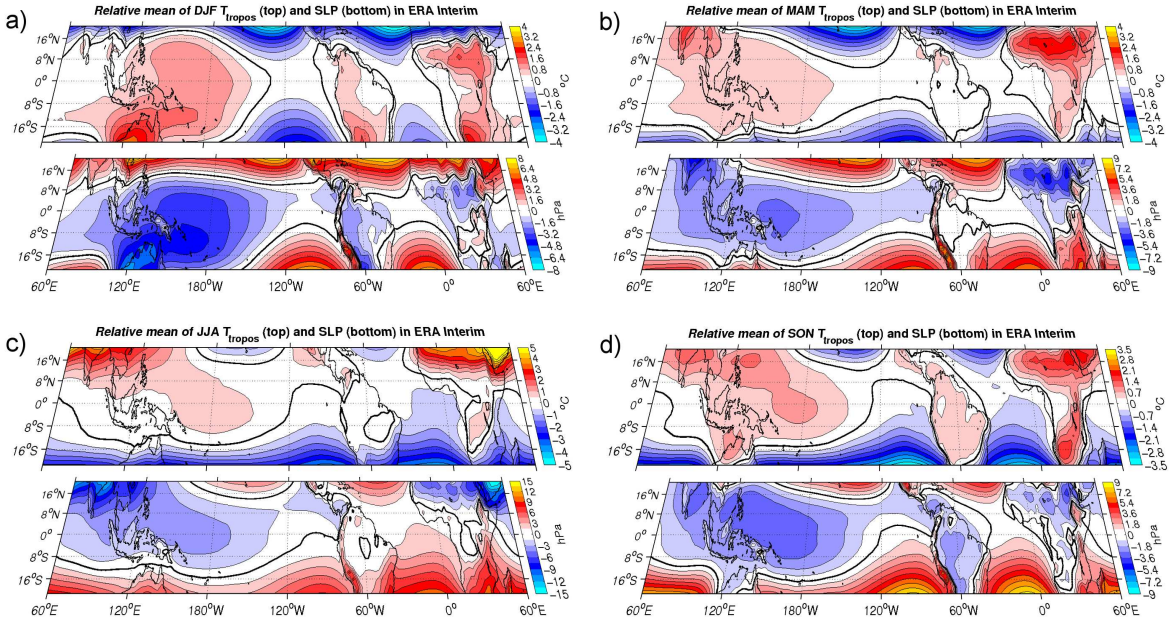

Figure 2.2: *Seasonal mean T_{tropos} (top) and SLP (bottom) in ERA Interim relative to the tropics area total mean in (a) DJF $(-10.0^oC, 1011.8hPa, -0.85)$, (b) MAM $(-9.6^oC, 1011.6hPa, -0.87)$, (c) JJA $(-9.9^oC, 1012.7hPa, -0.89)$ and (d) SON $(-9.9^oC, 1012.1hPa, -0.87)$; values in brackets are the subtracted area mean for T_{tropos}, SLP and the pattern correlation between the two patterns, respectively.*

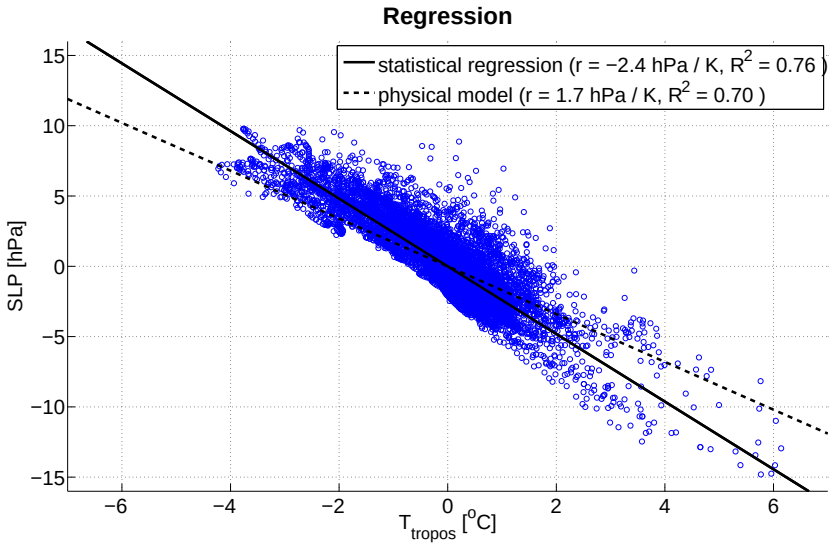

Figure 2.3: *Regression between relative T_{tropos} and SLP pattern from Fig. 2.2a-d for all four seasons together.*

in SLP. Regarding to the Bjerknes Circulation Theorem we propose the following mechanism behind the simple model: We consider initially two air columns with the same temperature and pressure (Fig. 2.4a). Warming the left column will expand the air, and cooling the right will contract the air (Fig. 2.4b). In the real world the Bjerknes Circulation tries to balance the temperature differences and induces a lateral mass flow between the warmer and the colder air

column and causes a SLP change. In our physical model we assume that the heights of the two columns are balanced at the end again (Fig. 2.4c). As in a hydrostatic framework the pressure is just the weight of the mass above we start in our simple model with the hydrostatic equation:

$$dp = -\rho\, g\, dh \tag{2.1}$$

with pressure p, density ρ, gravity constant g and air column height h. With

$$dh = \frac{h}{T}\, dT \tag{2.2}$$

we can calculate the isobaric thermal expansion of the air column using ideal gas law, with temperature T. To balance the heights of the two columns at the end, half of the height difference is moved from the warmer to the colder air volume. So with both equations we obtain for the SLP change in dependency of the temperature change:

$$\frac{dp}{dT} = 0.5\, \rho\, g \frac{h}{T} \tag{2.3}$$

Our model assumes lateral mass flow so that the pressure changes of many thin air volumes integrated vertically over the whole column is the same as the mass flow of one 900-hPa-thick column. This allows us to use the hydrostatic equation. From ERA Interim we obtain for the mean tropospheric density $\rho = 0.562kg\ m^3$, troposphere height $h = 16.5km$ and tropospheric temperature $T = 263.6K$ so that we yield a pressure change of $-1.7\ hPa$ at the surface per 1-K warming of the tropospheric air column above. This value is close to the statistical regression coefficient found in Fig. 2.3, indicating that the simple model describes a significant part of the SLP response to T_{tropos}. However, there is also a statistically significant deviation from the observed relationship, indicating that the model is not a complete match.

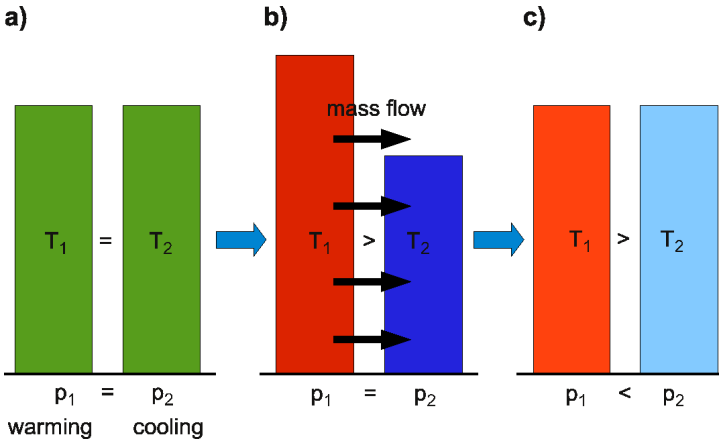

Figure 2.4: *Schematic of the physical model (for details see text).*

There are four assumptions for this model: First, the model only considers relative (inhomogeneous) changes in T_{tropos} and SLP, which means a mass redistribution only inside the tropics for SLP and a local heating relative to the tropical average for T_{tropos}. Thus the area mean is removed from SLP and T_{tropos} (as in Fig. 2.2a-d) before applying the simple model. A homogenous warming of T_{tropos} has no effect on SLP, as they would not induce any regional SLP changes (mass redistribution inside the tropics). The seasonal changes of the absolute values of

T_{tropos} and SLP (Fig. 2.2a-d) are an order of magnitude smaller than the regional differences within one season. Thus the inhomogeneous variations are much more pronounced than the homogeneous. With respect to the seasonal cycle, we can explain 70% of the SLP changes by the changes in T_{tropos} (Fig. 2.3), which is only 6% less than in the statistical regression.

Second, it is assumed that the T_{tropos} changes are given and independent of SLP changes. Thus SLP changes are assumed to be a response to T_{tropos}, but do not cause changes in T_{tropos}. This is a simplification, as changes in SLP or more generally in the atmospheric circulation will cause changes in T_{tropos}. However, the main feature in T_{tropos} change is the land-sea warming contrast (compare Fig. 2.1a and 2.5a top) due to processes and feedbacks that do not involve atmospheric circulation changes (*Joshi et al.*, 2008; *Dommenget and Flöter*, 2011). Indeed the tropical land-sea warming contrast can be reproduced very well in a global energy balance climate model that does not simulate atmospheric circulation changes (*Dommenget and Flöter*, 2011). Thus atmospheric circulation feedbacks can be considered as a secondary effect.

Third, the model does not consider that vertical column extent varies with topography. Since we interpolated all columns to sea level height, we implicitly assumed that this topographic effect is of secondary order.

Fourth, a pressure level exists, in which we have nearly no horizontal gradients in the geopotential height change, so that the mass has to redistribute below this level. This is best valid at the tropopause layer, which is in the tropics roughly at the 100 hPa level (not shown).

2.5 Projected Trends in the Multi Model Ensemble

Having established the fidelity of our simple model to describe the tropical SLP response to T_{tropos} changes over the seasonal cycle, we can now look at the multi-model ensemble mean trends of tropical climate change simulations for the period 1970 to 2099. First we can note that the SLP trend averaged over the entire tropics is 0.05 $hPa/100\ yr$ and is an order of magnitude smaller than the relative trends (about 0.22 $hPa/100\ yr$; spatial standard deviation of Fig. 2.5a bottom), indicating that mass flow in or out of the tropics is small compared to the tropical internal changes. Thus relative SLP changes in the tropics mark the main signal of tropical SLP changes. In contrast the T_{tropos} absolute trend ($3.6\,^{\circ}C/100\ yr$) is about an order of magnitude larger than the relative trends (up to $\pm 0.4\,^{\circ}C/100\ yr$).

Figure 2.5a shows the linear trend patterns in relative T_{tropos} and relative SLP for the period 1970 to 2099. Relative to the tropical mean warming, the troposphere over Africa and South America warms most (Fig. 2.5a top). A second strong relative warming appears in the very dry trade wind inversions over the eastern parts of the subtropical Atlantic and South Pacific. In agreement with the available moisture dependence of the land-sea warming contrast, the models predict a relative cooling over the Indo-Pacific warm pole region. Thus the land-sea contrast of surface and mid level warming dominates the T_{tropos} trend pattern. The ensemble mean relative trend of tropical SLP (Fig. 2.5a bottom) is mostly the opposite to the T_{tropos} trend pattern. This roughly zonal structure shows a mass redistribution from the Atlantic region to the warm pool region, and exhibits, as the T_{tropos} trend pattern, only small seasonal variations (not shown). Again the strong linear relationship between relative T_{tropos} and relative SLP trends can be illustrated by a scatter plot, see Fig. 2.5b. The linear regression coefficient between all T_{tropos} and SLP trend points is -2.0 hPa/K, which is a bit

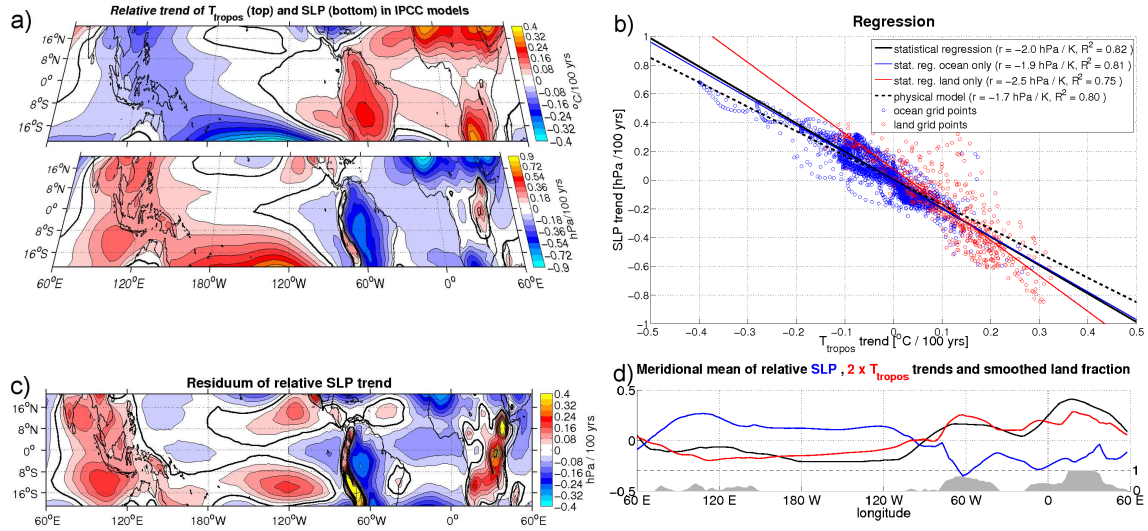

Figure 2.5: *(a) As in Fig. 2.2 but for linear trend of the IPCC multi-model ensemble for the period 1970 to 2099; area mean trend removed (3.6°C/100 yr for T_{tropos} and 0.05 hPa/100 yr for SLP); (b) regression of the two trend pattern in (a); (c) residuum of relative SLP trend after applying the physical model to multi-model ensemble data, (d) meridional mean of the two trend pattern in (a) and land fraction of the area between 23°S and 23°N in black, smoothed with a running mean of 60° and mean value subtracted; the grey filled area is the unsmoothed meridional mean of land fraction, with y-axis on the right.*

larger in magnitude than the physical model value of -1.7 hPa/K.

In this scatter plot the ocean grid points are colored in blue and the land grid points in red. Most ocean grid points have a negative trend in T_{tropos} and positive trend in SLP, and vice versa for the land grid points. Thus the relatively clear separation of land and ocean grid points in this point cloud illustrates again, that the land-sea warming contrast is the major driver for the tropical SLP changes. However, even if we look at the relation between T_{tropos} and SLP for ocean or land points only we find the same basic linear relationship. The linear regression coefficient and explained variance (R^2) values are similar for all ocean points and a bit stronger regression coefficient but smaller R^2 value for all land points. This mainly suggests that the link between T_{tropos} and SLP exists also on the smaller scales (e.g. within the continental regions) and is not just between land and ocean contrast, underlining the general relevance of Bjerknes Circulation Theorem in the tropics.

It is important to note here that the relationship of the surface temperature (T_{surf}) or SST and the SLP is not as clear as the relationship between T_{tropos} and SLP, because there are some significant changes in the relative warmings at different levels (see Fig. 2.1b): At the near surface (below 850hPa) the local land-sea distribution is dominating the warming contrast, but at the mid levels from 850hPa-400hPa the large-scale land-sea distribution is more important. In total we get therefore T_{tropos} trends with a large-scale hemispheric warming contrast between the hemisphere with more land (South America to Africa) and the hemisphere with mostly ocean (Indo-Pacific).

To underline the importance of considering the whole tropospheric warming instead of just the surface warming, we analyze the relation between T_{surf} or SST and SLP. In Fig. 2.6 the regression of T_{surf} (black line) and SST (blue line) shows a much weaker regression coefficient of 0.3 hPa/K, which can be explained by the stronger gradients at the surface than in T_{tropos}. But more important in the comparison is that with $R^2 = 0.82$ T_{tropos} can explain twice as much of the SLP trends as T_{surf} with $R^2 = 0.40$ and nearly five as much as SST with $R^2 = 0.17$ in a linear fit. This figure in comparison with Fig. 2.5b confirms as stated in *Flohn* (1975) that tropospheric temperature can describe the SLP response in a warming climate considerably better than (sea) surface temperature.

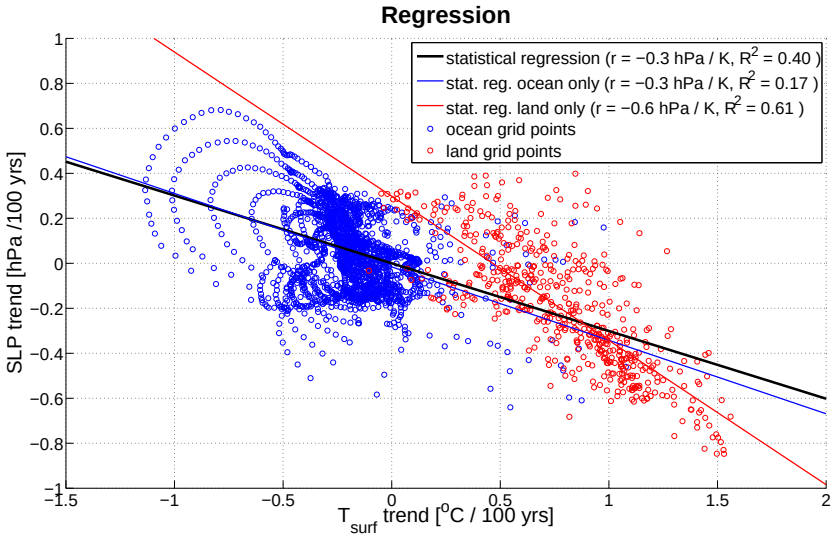

Figure 2.6: *Linear regression between relative trends of T_{surf} (Fig. 2.1a bottom) and SLP (Fig. 2.5a bottom) in the IPCC multi-model ensemble for the period 1970 to 2099.*

With the T_{tropos} trends our physical model can explain with 80% only 2% less of the SLP trends as the statistical regression. The residual SLP trends of the physical model are shown in Fig. 2.5c (note the different colorbar): Much of the trend signal is gone, highlighting that the model can explain a large part of the SLP trends, and the residuum trend no longer shows the large scale mass redistribution but more local trends.

The contrary relationship between relative T_{tropos} and SLP trends can also be seen very nicely in the meridional mean of the two trend pattern (Fig. 2.5d), with a correlation of -0.94 between the red and the blue curve. The dependency of the responses to the land warming shows up in comparison with the meridional mean of the tropical land fraction (black line in Fig. 2.5d), which is smoothed with a running mean of 60° and the mean value subtracted (correlation of 0.90 with T_{tropos} and -0.84 with SLP) or in comparison with the unsmoothed tropical land fraction (gray shaded area in Fig. 2.5d, correlation of 0.75 with T_{tropos} and -0.58 with SLP), only disagreeing slightly over the warm pool region. But this can be explained by the small size of the islands of the Maritime Continent, which leads to a more ocean-like cooling in the layers above the surface due to the close proximity of the oceans for all land points in coarse resolution models (Fig. 2.1b).

2.6 Projected Trends in the Individual CMIP3 Models

The response of individual IPCC models in the A1B scenario can be quite different from model to model. It is therefore instructive to discuss the distribution in the relationship between the relative T_{tropos} and SLP trends for all the IPCC models. Table 2.1 on page 24 lists some important values for all the individual IPCC models. The absolute trends of tropical T_{tropos} have with values between 2.2 and 5.5 $^{\circ}C/100\ yr$, on average 3.6 $^{\circ}C/100\ yr$, nearly the same spread and magnitude as the trends of the global mean surface temperature (*Meehl et al.*, 2007b).

Notable are the global mean SLP trends in the models, which suggest some unphysical trends that will have no impact on the atmospheric circulation. For most models the trends of the tropical SLP is very similar to the global mean trends (correlation of Tab. 2.1 column 4 with column 5 = 0.96, root mean square error = 0.85 hPa) indicating that the trends of air flow in or out of the tropics is much smaller than the tropical mean SLP trends would suggest. But with an average of 0.05 $hPa/100\ yr$ the multi-model mean has nearly no change for the absolute tropical SLP. These area mean trends of the tropics are removed to get the relative trend pattern. The spatial standard deviation of the relative trend pattern varies between 0.07 and 0.23 $^{\circ}C/100\ yr$, with an average of 0.14 $^{\circ}C/100\ yr$ for T_{tropos} and between 0.20 and 0.78 $hPa/100\ yr$, with an average of 0.37 $hPa/100\ yr$ for SLP.

The spatial distribution of nearly all IPCC models shows the same characteristic land-sea contrast pattern in the relative T_{tropos} and SLP trends (for some models they are shown in Fig. 2.8). The question arises, if the strength of the land-sea contrast in SLP trends in the individual model depends on the strength of land-sea contrast in T_{tropos} trends. In Figure 2.7 the land-sea contrasts in T_{tropos} and SLP are compared against each other. For T_{tropos} the land-sea contrast is defined as the ratio between the absolute land and ocean mean warming trend (as defined in *Sutton et al.* (2007) for surface temperature). We can first of all note that the land-sea contrast of T_{tropos} is an order of magnitude smaller than the land-sea contrast of T_{surf} (in e.g. *Sutton et al.*, 2007), which is due to much stronger horizontal diffusion in the free atmosphere. For the land-sea contrast in SLP trends we need a different definition, because the definition as ratio between land and ocean SLP trend would not fit here since the absolute trends are positive and negative. We therefore define the land-sea contrast for SLP trends on the basis of the difference between the average ocean and land trends, with ocean weighted with 80% and land with 20% according to their relative fractions in the tropics. Thus large deviations from zero indicate a strong land-sea contrast, as spatially independent distributed trends would yield a value of zero. In this figure we can see, that the models with a strong land-sea contrast in T_{tropos} tend to have also a strong land-sea contrast in SLP , which is also indicated by the regression line in black, and shows with a $R^2 = 0.66$ a significant relation.

We can take a closer look at the T_{tropos} and SLP trends in some models to get an idea of the extent to which the relationship between T_{tropos} and SLP varies. Fig. 2.8 shows the relative trend pattern and regressions of four models, which cover a wide range of different relationships between T_{tropos} and SLP trends.

The Bjerknes Centre for Climate Research (BCCR) Bergen Climate Model version 2 (BCM2.0) model has the weakest land-sea contrast in T_{tropos} and a weak sea-land contrast in SLP (see Fig. 2.7, number 1), which can be also seen in the trend pattern in Fig. 2.8a: The strongest warming takes place over the Pacific Ocean and the Atlantic Ocean and the SLP

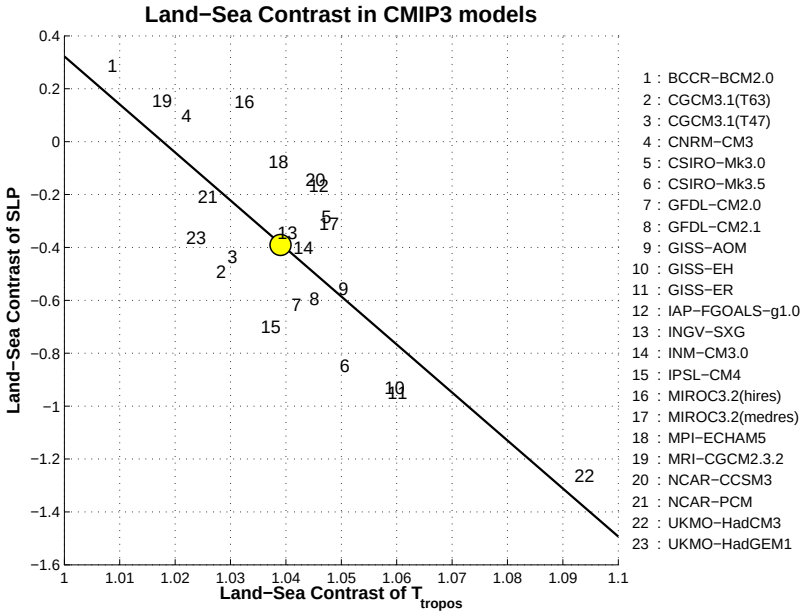

Figure 2.7: *Land-sea contrast in the individual IPCC models and the multi-model ensemble (circle) for T_{tropos} on the x-axis and SLP on the y-axis; for the definition of the land-sea contrast see text; the black line is the regression line with $R^2 = 0.66$.*

trends are mostly the opposite (pattern correlation = -0.74). Thus, despite the weak land-sea contrast in T_{tropos}, the linear relation between T_{tropos} and SLP is still strong (Fig. 2.8b, R^2 = 0.55). The regression of ocean only (blue line) and land only (red line) grid points yields similar regression coefficients but a higher R^2 value for ocean only and a lower for land only. Further the land-sea contrast at surface is with 1.35 in the normal range (not shown) but the land-sea contrast in T_{tropos} is with 1.01 (Fig. 2.7) very low, indicating that the coupling between surface and troposphere is different than in the other models.

The Max-Planck Institute (MPI) ECHAM5 model has nearly no land-sea contrast in SLP and is in the lower middle of the land-sea contrast range (see Fig. 2.7, number 18), even so the land-sea contrast is clearly imposed on both trend patterns in Fig. 2.8c. The SLP trends disagree strongly with our hypothesis above the mountainous regions. The regression (Fig. 2.8d) shows a relation between these two patterns (R^2 = 0.42) and the ocean and land grid points are mostly separated, but not directly along the regression line. The regression for the ocean only and land only grid points has a similar regression coefficient, but a higher R^2 value for ocean only and an even weaker for land only. Here the land-sea contrast values of T_{surf} and T_{tropos} are both in the normal range, but the land-sea contrast in SLP is very low (Fig. 2.7), so that in this model the coupling of T_{tropos} and SLP over the mountainous regions, seems to be different from the other models.

The Geophysical Fluid Dynamics Laboratory Climate Model version 2.1 (GFDL-CM2.1) model is in the upper middle of the land-sea contrast range (see Fig. 2.7, number 8) and the trend pattern (Fig. 2.8e) looks quite similar to those of the multi-model ensemble. The land and ocean points are well separated along the regression line, which show with a R^2 = 0.72 a strong relation (Fig. 2.8f). The regression for ocean only and land only is here quite similar to the all grid points regression.

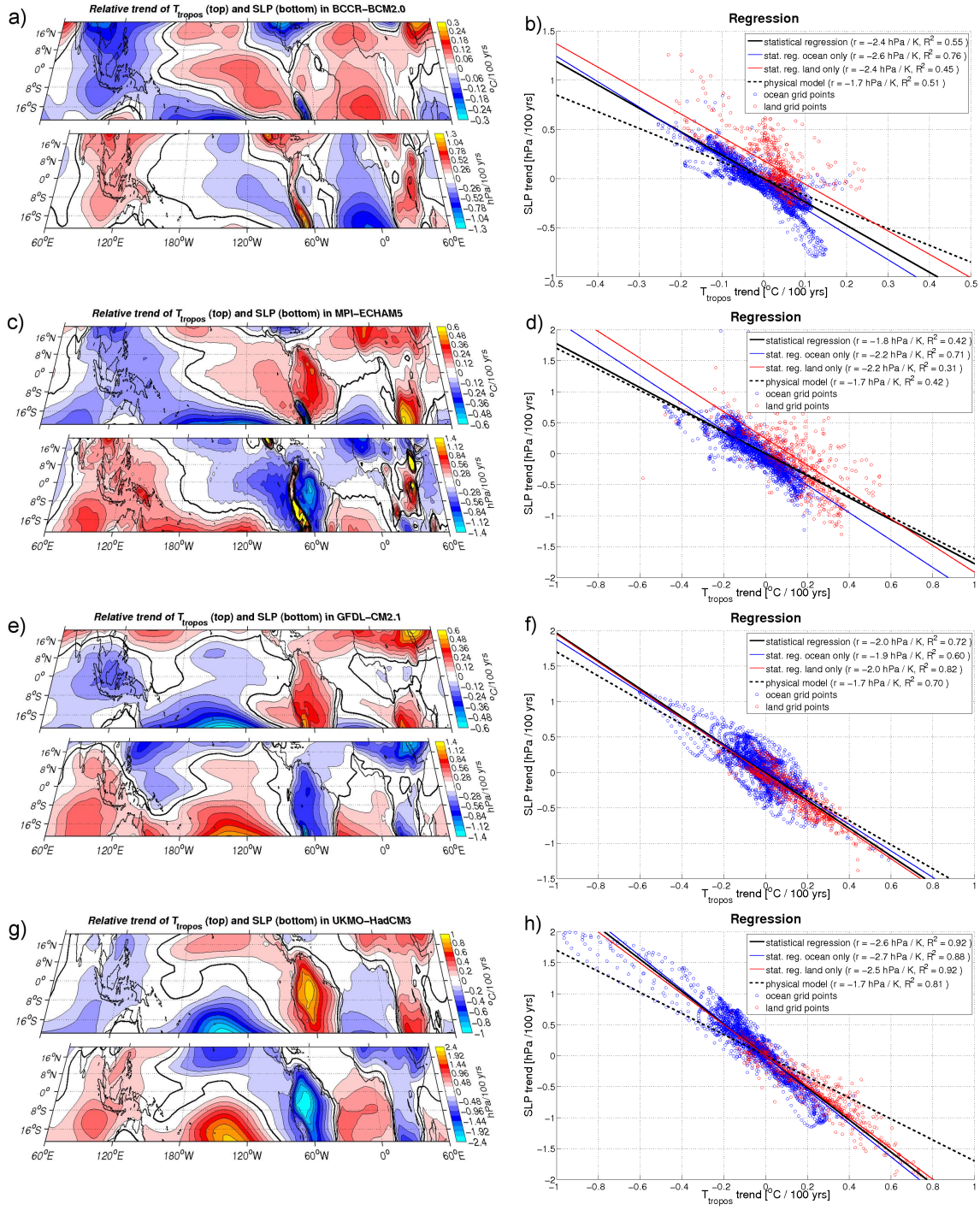

Figure 2.8: *As in Fig. 2.5a,b, but in (a),(b) for BCCR-BCM2.0, in (c),(d) for MPI-ECHAM5, in (e),(f) for GFDL-CM2.1 and in (g),(h) for UKMO-HadCM3 climate model.*

The third climate configuration of the United Kingdom Met Office Unified Model (UKMO-HadCM3) is the model with the strongest land-sea contrast (see Fig. 2.7, number 22) and in the trend patterns (Fig. 2.8g) the land-sea contrast is imposed on both trend pattern and the amplitudes are stronger than in the multi-model ensemble. The regression (Fig. 2.8h) shows a clear relation between these two patterns ($R^2 = 0.92$) and a clear separation of ocean and land grid points due to the strong land-sea contrast. Here again the regression for ocean only and land only is quite similar to the all grid points regression. In these four models the R^2 value is higher over ocean than over land, with bigger differences in the models where we have only a weak land sea contrast in T_{tropos} or SLP , so that the interaction over land seems to be the critical point in these models.

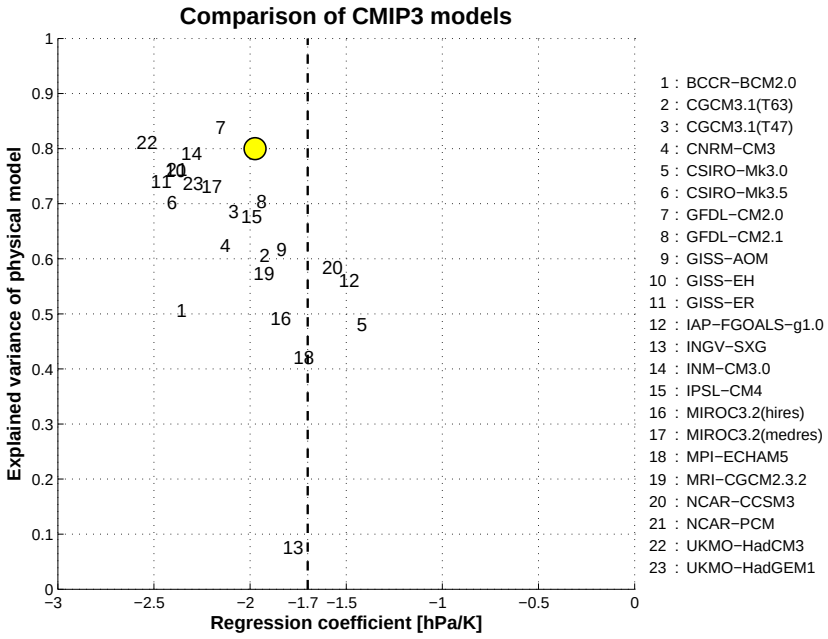

Figure 2.9: *Comparison of regression coefficient and explained variance of the physical model in the individual IPCC models and the multi-model ensemble (circle). The black dashed line represents the corresponding sensitivity coefficient of the physical model.*

Most of the remaining models have trend pattern that are quite similar to the ones of the multi-model ensemble. With pattern correlations between the two trend pattern between -0.28 and -0.96, with an average of -0.80 (Tab. 2.1), we can see that in most of the IPCC models the SLP trends are strongly related to the T_{tropos} trends. The statistical regression of the trend patterns yields values between -1.4 and -2.6 hPa/K (Fig. 2.9), with an average of -2.1 hPa/K, and R^2 values between 0.08 and 0.92, with an average of 0.67. These regression coefficients are on average again a bit stronger than in the simple physical model (black dashed line), indicating that the simple model underestimates the link between T_{tropos} and SLP. The simple model can explain in the individual IPCC models between 8% and 84% of the SLP trends, with an average of 63%, but all except one model explaining more than 40% (Fig. 2.9).

We conclude that the strong coupling between the T_{tropos} and SLP trends is evident in most of the models, even if the land-sea contrast is not the dominant signal in the trends, as in BCCR-CM2.0 model. And models that have a strong land-sea contrast in T_{tropos} trends

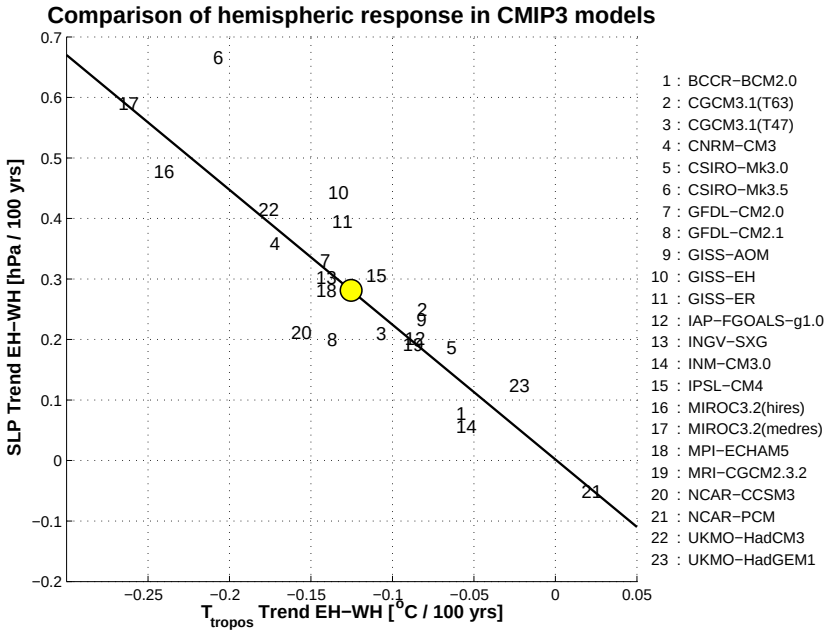

Figure 2.10: *Comparison of the "eastern" hemispheric* $(60^oE - 120^oW, 23^oS - 23^oN)$ *minus the "western" hemispheric* $(120^oW - 60^oE, 23^oS - 23^oN)$ *trend of* T_{tropos} *(on x-axis) and* SLP *(on y-axis) of the individual IPCC models and the multi-model ensemble (circle); the black line is the regression line with* $R^2 = 0.79$*.*

tend to have also a strong land-sea contrast in SLP trends. Further in most of the models the land-sea contrast is the dominant signal in the trend pattern: As already stated in the introduction the land-sea contrast depends on available moisture, so that we expect a stronger warming in T_{tropos} and decreasing SLP over the South American/African sector and a relative cooling in T_{tropos} and increasing SLP over the Indo-Pacific warm pool region. This is true for nearly all individual models with a strong linear relation (Fig. 2.10).

2.7 SLP response in idealized T_{land} +1 K experiment

We can use a set of atmospheric general circulation model (AGCM) experiments to investigate how the atmospheric circulation responds to tropical land warming. This should give some support for the hypothesis that the SLP trends are being primarily a response to the tropospheric temperature warming pattern, which is dominated by the land-sea warming contrast. We therefore analyze some experiments of *Dommenget* (2009), in which the response of an AGCM to warming of the global land by +1K and cooling of the global land by -1K is simulated. The SST in the AGCM is free to respond, as the SST is simulated by a simple single column ocean mixed layer model; see *Dommenget* (2009) for details. Thus these experiments are not constructed in a way that they can exactly reproduce the IPCC runs, as the surface land warming is here prescribed homogeneously over all land points, independent from available moisture or distant to the coasts.

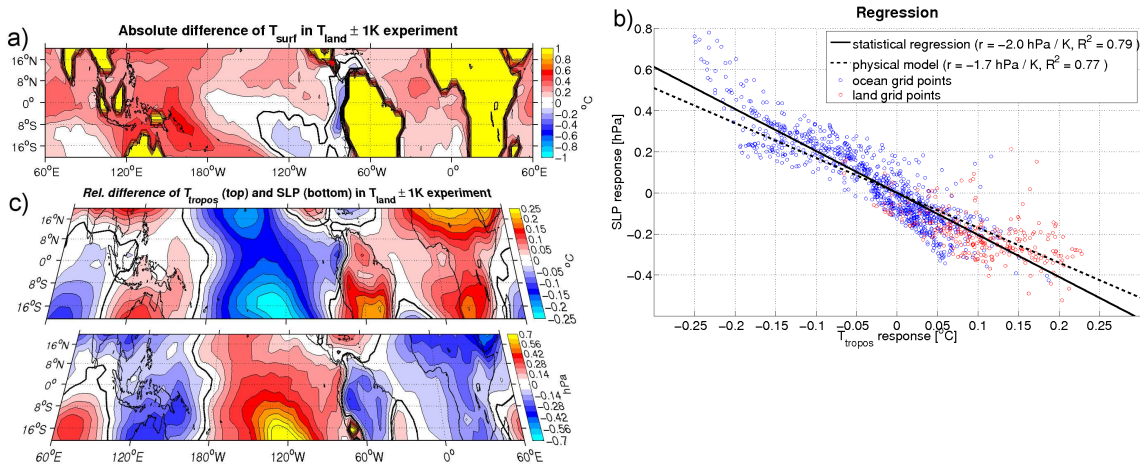

Figure 2.11: *(a) Absolute difference of T_{surf} in the idealised T_{land} ±1K experiment; (b),(c) as Fig. 2.5a,b, but here the relative difference of the idealised experiment, area mean response of 0.6°C for T_{tropos} and -0.05 hPa for SLP removed; pattern correlation = -0.89.*

The results are shown in Fig. 2.11, with the response defined as the difference between the land +1K minus the land -1K divided by 2. The ocean warms much less than 1K in response to the 1K surface land temperature increase (Fig. 2.11a), as discussed in *Dommenget* (2009), and surface temperature has a very strong land-sea contrast of 5.1. The relative response of tropospheric temperature is positive over the continents and mostly negative over the oceans, with higher response over the dry subtropics than over the wetter tropics (Fig. 2.11c top), as expected from the land-sea warming contrast. In agreement with the Bjerknes Circulation Theorem the SLP response is mostly the opposite of the T_{tropos} response (Fig. 2.11c bottom, pattern correlation -0.89). These patterns have similar trends as the global warming runs over Africa, the Atlantic, South America and the Pacific, but disagree in sign over Southeast Asia, the Maritime Continent and Australia. In the idealised runs we have a clear land-sea contrast signal over the warm pool region, as they are prescribed, but in the IPCC runs there is no land-sea contrast in T_{tropos} and SLP . As stated above this difference can be explained with the experimental setup of the idealised experiments, where the land-sea contrast is forced by the fixed land surface temperature change.

A regression between these two response patterns yields a regression coefficient similar to the sensitivity coefficient of the physical model (2.0 hPa/K, Fig. 2.11b) and 79% of the SLP response can be explained by the T_{tropos} response in a linear fit (77% in the physical model). The ocean and land grid points are clearly separated along the regression line, indicating that the land-sea contrast is the major forcing in this two trend pattern. In summary, in these idealized experiments the trend patterns support our hypothesis, that land-sea contrast is the major driver for the large-scale SLP response in a warming climate.

2.8 Observed Trends in ERA Interim Reanalysis

We can now look at observed trends in the tropics over the last two decades to see if a strong relation between relative T_{tropos} and SLP trends exists there too. However, we have to keep in mind a few important differences between the observed and simulated trends: first, the observed trends are more uncertain than those of the IPCC scenario simulations, due to the much shorter observed time period of 22 yr versus the 130 yr of the IPCC scenario simulations used to estimate the trends. Second, it has to be noted that the trends in the 20^{th} century are weaker than those of the 21^{th} century, which will lead to a weaker trend signal in the observation compared to the IPCC scenario simulations. Third is has to be noted that tropical natural variability, such as El Nino, has a stronger impact on relative short time period trends, which will decrease the signal to noise ratio in the observations. Last we have to consider that the observations are just one realization of the warming trend, whereas the IPCC scenario simulations are 23 realizations averaged to one ensemble mean. Thus the observed trends will be much more uncertain and will contain a much larger fraction of internal natural variability than the IPCC scenario simulations.

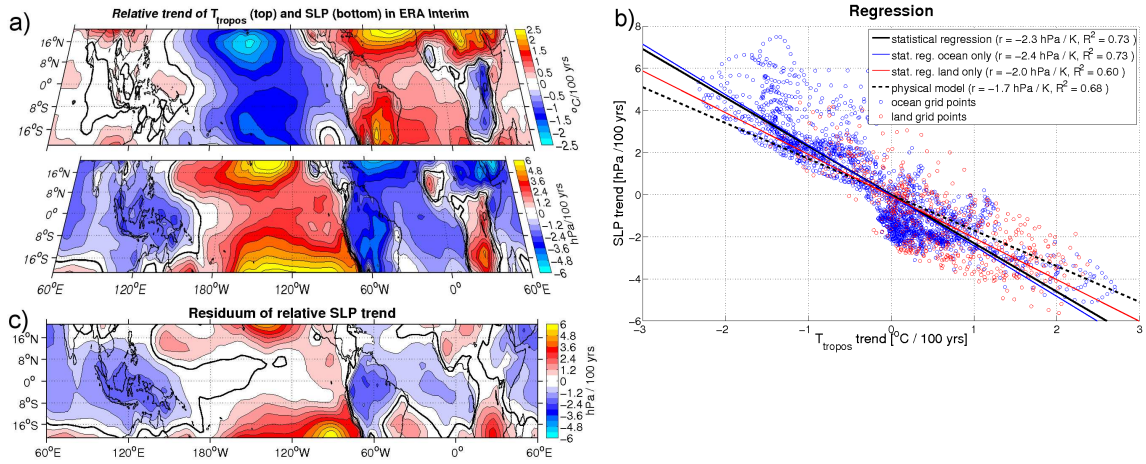

Figure 2.12: *As in Fig. 2.5 but here for the ERA Interim reanalysis data in the period 1989 to 2010; area mean trend removed in (a): 1.7°C/100 yr for T_{tropos} and -1.2 hPa/100 yr for SLP .*

The trend patterns for the period 1989 to 2010 shown in Fig. 2.12a have some similarities with the projected trend pattern of the IPCC models, but the amplitudes over ocean are larger than those over land. The overall T_{tropos} warming trend of $1.7\,^{\circ}C/100\ yr$ lies within the range of trends due to natural variability simulated by a control simulation of a coupled ECHAM5 model (*Bengtsson and Hodges*, 2009). Again these two patterns are highly anti-correlated (-0.85) and pattern regression yields a regression coefficient of $-2.3hPa/K$ (Fig. 2.12b). In the point clouds the land and ocean grid points are only weakly separated, indicating that land-sea contrast is not dominating this trend pattern. The regression for ocean only (blue line) and land only (red line) yields similar values as for all grid points, with a slightly smaller regression coefficient and R^2 value for land only. The large-scale residuum pattern obtained from the simple model (Fig. 2.12c) has a quite similar structure to the trend pattern, but weaker amplitudes. The physical model can explain 68% of the SLP trends.

2.9 Summary and Discussion

In the study presented above we address the causes of the large-scale tropical SLP changes during climate change. Since tropical SLP is an important indicator for the mean state and variability of the tropical atmospheric circulation we implicitly assume that the analysis of the tropical SLP changes will provide us a basis for understanding changes in the tropical atmospheric circulation. The analysis we present was based on the CMIP3 climate model simulations for future climate change scenarios, the observed seasonal cycle and on recent observations of trends in the tropical climate.

In summary we found a quite robust and strong relationship between the large-scale trends in tropical T_{tropos} and SLP . This relationship is physically based on the thermodynamic response of the SLP to inhomogeneous T_{tropos} warming. In this picture, the trends in the T_{tropos} warming drive the large-scale changes in SLP. This is evident in nearly all IPCC models, independent if land-sea contrast is dominating the two trend pattern or not. With the help of a simple physical model we can measure the ratio between the SLP and T_{tropos} trends (-1.7 hPa/K) and can predict a large part of the SLP trends if we know the T_{tropos} trends. Further the dominating feature of the inhomogeneous T_{tropos} warming, which is in most of the IPCC simulations the land-sea contrast, is imprinted onto the SLP trend pattern as well. This leads to decreased SLP over South America, the Atlantic and parts of Africa and increased SLP over the tropical Indo-Pacific warm pool and implies changes in the regional distribution of tropical deep convection. Indeed all of the IPCC models except one predict increasing SLP and a weaker warming of T_{tropos} over the warm pool region and decreasing SLP and a stronger warming of T_{tropos} over the South American/African region (Fig. 2.10).

In the comparison of the IPCC models it becomes evident that the models that have a strong land-sea contrast in T_{tropos} tend to have also a strong land-sea contrast in SLP. Further we could support our hypothesis with an idealised sensitivity experiment, in which we prescribed the land warming.

In recent years the tropical SLP response in global warming was often discussed in context of the enhanced hydrological cycle and the accompanied weakening of the tropical circulations, as in *Vecchi and Soden* (2007, hereafter *VS*07). This discussion, however, did not consider the second important change of tropical temperature: the land-sea warming contrast. The question arises: How does our new idea fit in their discussion about the weakening Walker Circulation: Their Fig. 10 (top) is similar to our Fig. 2.5a (bottom) with a similar tendency in the relative SLP trends over the Indo-Pacific warm pool region and the tropical Pacific, even though they only considered SLP changes only over the oceans. *VS*07 based their argument on the interaction between SST in this region and the Walker Circulation, but found a disagreement between the SLP and SST change. Further, it needs to be noted that our simple model does not make any statement on how the tropical Pacific SST may change, which is central to the *VS*07 study. The simple model discussed here explains a large fraction of the total SLP trends over the Indo-Pacific warm pool region ($R^2 = 0.81$), but the residuum of this model shows still a decrease in SLP gradient over the Pacific Ocean that would fit to the *VS*07 study. In turn, our explanation for the roughly zonal SLP response due to inhomogeneous T_{tropos} warming could be the missing piece, explaining why the zonal Walker Circulation weakens stronger than the meridional Hadley Circulation: Two of the three main convection regions (South America and Africa) warm stronger than the third (the Indo-Pacific warm pool), which decreases the relative

importance of the latter. This zonal inhomogeneous distribution of the land-sea contrast leads to zonal changes that affect the Walker circulation, but do not affect the Hadley circulation that much. Thus it seems that both approaches fit together: *VS*07 considering the changes in the vertical temperature profile and this study here the horizontal. However, the results presented in here suggest that land-sea warming contrast is probably the most important driver of the large scale SLP change and that future changes in the spatial distribution of relative low SLP , with associated upward air motion, which would favor deep convection conditions, are strongly controlled by the relative changes in tropospheric temperatures.

From reanalysis data the question arises, if the trend in the tropical SLP is the warming climate signal as seen in the IPCC simulations or if it is natural variability. The trend patterns show some similarities to those in the IPCC simulations, but this trend lies within the range of natural variability, simulated by a control simulation of a coupled ECHAM5 model (*Bengtsson and Hodges*, 2009) and both variables have stronger trends over oceans than over land. Further the negative SLP trend over the Maritime Continent together with the positive trend over the east Pacific shows an increase in the zonal SLP gradient over the Pacific, which can be interpreted as an increase in strength of the Walker Circulation due to natural variability, as proposed by *Meng et al.* (2011). The response of equatorial Pacific in a warming climate is a topic of recent research (e.g. *DiNezio et al.*, 2009; *Park et al.*, 2009) but still model dependent (*Latif and Keenlyside*, 2009). From these uncertainties in the dynamical response and the short records of observations it is difficult to assess, what part of the observed trends is natural variability and what is climate change. However, the relative trends of T_{tropos} and SLP in observations are also strongly related, following mostly the simple thermodynamical model discussed in this study.

Acknowledgments

We acknowledge the individual modeling groups, the Climate Model Intercomparison Project (CMIP3) and ECMWF for providing the data sets. This work was supported by the Deutsche Forschungsgemeinschaft (DFG) through project DO1038/5-1 and the ARC Centre of Excellence in Climate System Science (CE110001028). We thank Richard Greatbatch, Jan Harlaß, Kevin Hodges, Noel Keenlyside, Joe Kidston, Mojib Latif, Willi Rath, Thomas Reichler and the anonymous reviewers for discussion and useful comments.

Model	Absolute T_{tropos} trend [K/100yr]	Relative T_{tropos} trend [K/100yr]*	Absolute SLP trend tropics [hPa/100yr]	Absolute SLP trend global [hPa/100yr]	Relative SLP trend [hPa/100yr]*	Pattern correlation**	Statistical regression coefficient [hPa/K]**	R^2 value of stat. regression**	R^2 value of simple model**
Multi Model Ensemble	3.6	0.10	0.05	−0.10	0.22	−0.90	−2.0	0.82	0.80
BCCR-BCM 2.0	3.1	0.08	0.40	0.27	0.25	−0.74	−2.4	0.55	0.51
CGCM3.1(T63)	4.2	0.12	−0.24	−0.34	0.30	−0.79	−2.0	0.62	0.61
CGCM3.1(T47)	3.7	0.11	−0.16	−0.29	0.28	−0.85	−2.1	0.71	0.69
CNRM-CM3	3.8	0.12	0.45	0.28	0.32	−0.81	−2.2	0.65	0.62
CSIRO-MK3.0	2.6	0.11	−0.12	−0.20	0.23	−0.70	−1.4	0.50	0.48
CSIRO-MK3.5	4.0	0.17	−0.26	−0.30	0.47	−0.88	−2.4	0.77	0.70
GFDL-CM2.0	3.8	0.15	−0.16	−0.33	0.36	−0.94	−2.2	0.88	0.84
GFDL-CM2.1	3.8	0.14	0.34	0.18	0.34	−0.85	−2.0	0.72	0.70
GISS-AOM	2.9	0.10	0.17	0.18	0.24	−0.79	−1.9	0.62	0.62
GISS-EH	3.2	0.14	0.08	−0.24	0.37	−0.92	−2.4	0.84	0.76
GISS-ER	3.2	0.13	0.06	−0.27	0.36	−0.91	−2.5	0.83	0.74
IAP-FGOALS1.0	2.8	0.11	0.11	−0.17	0.21	−0.75	−1.5	0.57	0.56
INGV-SXG	3.3	0.12	0.01	−0.18	0.78	−0.28	−1.8	0.08	0.08
INM-CM3.0	3.0	0.12	−0.26	−0.29	0.31	−0.93	−2.4	0.86	0.79
IPSL-CM4	4.2	0.14	−0.13	−0.37	0.34	−0.83	−2.0	0.70	0.68
MIROC3.2(hires)	5.5	0.20	0.53	0.43	0.53	−0.70	−1.9	0.50	0.49
MIROC3.2(medres)	4.1	0.21	0.43	0.30	0.53	−0.88	−2.3	0.78	0.73
MPI-ECHAM5	4.6	0.15	−0.03	−0.22	0.40	−0.65	−1.8	0.42	0.42
MRI-CGCM2.3.2	3.0	0.11	−0.02	−0.16	0.28	−0.76	−2.0	0.59	0.57
NCAR-CCSM3	3.2	0.14	0.33	0.25	0.29	−0.77	−1.6	0.59	0.58
NCAR-PCM	2.2	0.07	0.21	0.04	0.20	−0.92	−2.4	0.84	0.76
UKMO-HadCM3	3.6	0.23	−0.74	−0.88	0.62	−0.96	−2.6	0.92	0.81
UKMO-HadGEM1	3.9	0.17	0.23	0.01	0.45	−0.89	−2.3	0.80	0.74
Average	**3.6**	**0.14**	**0.05**	**−0.10**	**0.37**	**−0.80**	**−2.1**	**0.67**	**0.63**

*Spatial standard deviation of the relative trend pattern.
**For the two relative trend pattern of SLP and T_{tropos}.

Table 2.1: *Some statistical values of all IPCC models investigated in this study; boldfaced last row is the average over all 23 individual models.*

Chapter 3

Comparing the spatial structure of variability in two datasets against each other on the basis of EOF-modes

This chapter is a reprint of the paper "Comparing the spatial structure of variability in two datasets against each other on the basis of EOF-modes" published online in Climate Dynamics.

Citation: Bayr, T., and Dommenget, D. (2013b), Comparing the spatial structure of variability in two datasets against each other on the basis of EOF-modes. Climate Dynamics. doi:10.1007/s00382-013-1708-x.

Abstract

In analysis of climate variability or change it is often of interest how the spatial structure in modes of variability in two datasets differ from each other, e.g. between past and future climate or between models and observations. Often such analysis is based on Empirical Orthogonal Function (EOF) analysis or other simple indices of large-scale spatial structures. The present analysis lays out a concept on how two datasets of multivariate climate variability can be compared against each other on basis of EOF analysis and how the differences in the multivariate spatial structure between the two datasets can be quantified in terms of explained variance in the leading spatial patterns. It is also illustrated how the patterns of largest differences between the two datasets can be defined and interpreted.

We illustrate this method on the basis of several well-defined artificial examples and by comparing our approach with examples of climate change studies from the literature. These literature examples include analysis of changes in the modes of variability under climate change for the sea level pressure (SLP) of the North Atlantic and Europe, the SLP of the Southern Hemisphere, the surface temperature of the Northern Hemisphere, the sea surface temperature of the North Pacific and for precipitation in the tropical Indo-Pacific.

3.1 Introduction

Climate variability has significant spatial structure that is often characterized by so called modes of variability. Such modes are, for instance, the El Nino Southern Oscillation (ENSO), the Pacific Decadal Oscillation (PDO), the North Atlantic Oscillation (NAO) or the Southern Annular Mode (SAM). These modes are assumed to be quasi-fixed spatial patterns (*Wallace and Gutzler*, 1981), that represent a relative large part of climate variability. Alternatively one can think of the climate variability as a multivariate stochastic process, which has a continuum of spatial patterns of variability (e.g. see discussion in *Dommenget*, 2007; hereafter D07). Independent of whether we think of the climate variability as fixed modes (factors) or a continuum of spatial patterns reflecting a multivariate stochastic process, often the question arises: What are the differences in the spatial structures of variability between one time period and another or between a control and a sensitivity experiment or between model simulations and observations? The aim of this study presented here is to outline a concept of how such a comparison can be done in a quantitative way on the basis of Empirical Orthogonal Function (EOF) analysis (also known as principal component analysis).

As the multivariate structure of any dataset is unique and different from any other dataset, a special frame is needed to be able to compare the multivariate structure of two data sets. *Jolliffe* (2002, Chapter 13.5) gives a nice overview about EOF related technics for comparing the multivariate structure in two or more datasets against each other. Some of these technics aim to find some common eigenvectors, which are then used as basis to compare the individual datasets (e.g. in common principal component analysis in *Sengupta and Boyle*, 1998). Some other technics suggest a criterion like the angle between the eigenvectors of different datasets to find out if eigenvectors differ significantly from each other (e.g. in *Krzanowski*, 1979). Beyond that several other technics were used in recent literature to investigate the changes in the modes of variability under increased greenhouse gas emissions (e.g. *Osborn*, 2004; *Rauthe et al.*, 2004; *Hu and Wu*, 2004; *Kuzmina*, 2005; *McHugh and Rogers*, 2005; *Miller et al.*, 2006; *Stephenson et al.*, 2006; *Keeley et al.*, 2008). Most of these technics focus on the changes in one particular mode or compare the leading modes pairwise. Although this gives a good discussion of how the particular investigated leading modes will change, it remains unclear whether this change is representative for the whole multivariate stochastic variability or it is the most important change in the dataset. Considering only the dominant mode in the dataset will in most cases exclude the largest part of the variability that is represented by all the other modes of variability. It also needs to be considered that the changes in the spatial structure of the variability may not be well described by the changes in one or two particular modes at all. The change in the spatial structure of variability is not limited to intensification, reduction or shift in one pattern, but it could, for instance, be a change in the length scale of variability in general, a change in the higher ordered modes or a change of in multiple patterns, thus of the multivariate structure.

The method that we will describe is based on the Distinct Empirical Orthogonal Function (DEOF) analysis introduced by D07. The basic idea is similar to the one of *Krzanowski* (1979), but our method takes the whole multivariate structure of the two datasets into account. The method allows to objectively quantify differences between the multivariate structure of two datasets and it allows to define the patterns which best describe these differences. The paper is organised as follows: In Sect. 3.2 the data used in this study are presented, and the new method is introduced in Sect. 3.3. The statistical significance levels of the DEOF patterns

are discussed in Sect. 3.4. How this method works and how the results can be interpreted is illustrated in Sect. 3.5 on the basis of four well-defined constructed examples. The robustness of this method is then compared against several literature examples of studies about changes in the modes of variability under climate change scenarios in Sect. 3.6. The study is concluded with a summary and discussion section.

3.2 Data

The data analysed in this study are taken from the Climate Model Intercomparison Project 3 (CMIP3, *Meehl et al.*, 2007a). We selected all climate models, which had sea level pressure (SLP), surface temperature (T_{surf}), sea surface temperature (SST) and precipitation available for the present day (20C) and global warming scenario (A1B); see Table 3.1 for a list of climate models. For each model simulation the linear trend and mean annual cycle is subtracted to define anomalies which are interpolated onto a common 2.5° x 2.5° grid. The anomalies of the 24 individual model simulations are then concatenated to build one multi-model ensemble dataset with one ensemble member from each model.

Model	Institute
BCCR-BCM2.0	Bjerknes Centre for Climate Research, Norway
CGCM3.1(T63)	Canadian Centre for Climate Modelling and Analysis, Canada
CGCM3.1(T47)	Canadian Centre for Climate Modelling and Analysis, Canada
CNRM-CM3	Centre National de Recherches Meteorologiques, France
CSIRO-Mk3.0	Commonwealth Scientific and Industrial Research Organisation, Australia
CSIRO-Mk3.5	Commonwealth Scientific and Industrial Research Organisation, Australia
GFDL-CM2.0	Geophysical Fluid Dynamics Laboratory, USA
GFDL-CM2.1	Geophysical Fluid Dynamics Laboratory, USA
GISS-AOM	Goddard Institute for Space Studies, USA
GISS-EH	Goddard Institute for Space Studies, USA
GISS-ER	Goddard Institute for Space Studies, USA
IAP-FGOALS-g1.0	Institute of Atmospheric Physics, China
INGV-SXG	Italian National Institute of Geophysics and Volcanology, Italy
INM-CM3.0	Institute for Numerical Mathematics, Russia
IPSL-CM4	Institut Pierre Simon Laplace, France
MIROC3.2(hires)	Center for Climate System Research, Japan
MIROC3.2(medres)	Center for Climate System Research, Japan
MIUB-ECHO-G	Meteorological Institute of the University of Bonn, Germany, Meteorological Research Institute of the Korea
MPI-ECHAM5	Max Planck Institute for Meteorology, Germany
MRI-CGCM2.3.2	Meteorological Research Institute, Japan
NCAR-CCSM3	National Center for Atmospheric Research, USA
NCAR-PCM	National Center for Atmospheric Research, USA
UKMO-HadCM3	Hadley Centre for Climate Prediction and Research/Met Office, UK
UKMO-HadGEM1	Hadley Centre for Climate Prediction and Research/Met Office, UK

Table 3.1: *List of climate models taken from the CMIP3 database*

3.3 Method of comparing two sets of EOF-modes

In the following we assume that the spatial structure of the variability in two datasets is well represented by the leading EOF-modes of each dataset. Note that the set of EOF-modes of any dataset is unique and different from any other dataset. In order to be able to compare the relative importance of the different modes in two different datasets we need to define a common reference set of modes. A method of comparing two sets of EOF-modes against each other has been discussed in D07. Therein the EOF-modes of a dataset are compared against the EOF-modes of the stochastic null hypothesis of isotropic diffusion by projecting the leading EOF-modes of the isotropic diffusion process onto the EOF-modes of the dataset. This approach can be generalized by replacing the EOF-modes of the stochastic null hypothesis with the EOF-modes of any other dataset. Thus we define the EOF-modes of our first dataset "A" as the reference modes. The variance that each (i-index) of the reference modes from dataset $A, \vec{E}_i^A$ would explain in the dataset B can be estimated by projecting all of the EOF patterns of $A, \vec{E}_i^A$ onto the EOF pattern of $B, \vec{E}_j^B$, or in shortened form, $A \rightarrow B$. Due to the orthogonality of the EOF pattern, the sum over all linear combinations gives us the explained variance the EOF pattern of $\vec{E}_i^A$ would have in the dataset B:

$$pev_i^{A\rightarrow B} = \sum_{j=1}^{N} c_{ij}^2 \, ev_j^B \tag{3.1}$$

with projected explained variance, $pev_i^{A\rightarrow B}$, the explained variance of the jth EOF pattern in dataset B, ev_j^B and

$$c_{ij} = \frac{\vec{E}_j^B \vec{E}_i^A}{\left|\vec{E}_j^B\right| \left|\vec{E}_i^A\right|} \qquad \text{(pattern correlation)} \tag{3.2}$$

It is important to note that the projected explained variances $pev_i^{A\rightarrow B}$ do not have to be monotonically decreasing as the explained variances of EOF-modes do. An EOF-mode that explains at lot of variance in dataset A does not need to explain as much variance in dataset B and vice versa. We can now directly compare the spectrum of ev_i^A values against the $pev_i^{A\rightarrow B}$ values to estimate which modes have different strength in the two datasets.

One has to keep in mind that the differences between the two datasets may be largest in a pattern that does not project well onto any of the EOF-modes. In order to find the pattern which shows the largest differences in explained variance between the two datasets it is necessary to rotate the EOF-modes to a set of patterns that maximize the difference in explained variance between the two datasets. These modes are called the DEOF patterns. They can be found by pairwise rotation of the EOF-modes to maximize the difference in the leading ev_i^A values relative to the $pev_i^{A\rightarrow B}$ (See D07 for details).

The DEOF patterns have two explained variance values: one is corresponding to the amount of variance the pattern explains in dataset $A, dev^{A\rightarrow B}(A)$, and the other is the corresponding values for dataset $B, dev^{A\rightarrow B}(B)$. The DEOF-modes are ordered by the difference in explained variance between $dev^{A\rightarrow B}(A)$ and $dev^{A\rightarrow B}(B)$, and not, as in EOF analysis, by the explained variance of the pattern. It is important to keep in mind that interpretation of the DEOF-patterns can be equally difficult as for the normal EOF-modes.

The leading DEOF-mode, DEOF-$1^{A\to B}$, is the pattern that explains more variance in dataset A than in dataset B. No other pattern can have a larger difference in the explained variance between the two datasets, $\Delta dev^{A\to B} = dev^{A\to B}(A) - dev^{A\to B}(B)$, than DEOF-1, as the pattern are ordered by their $\Delta dev^{A\to B}$. In turn, if we want to know which patterns have a higher explained variance in dataset B than in dataset A, we have to repeat the analysis by defining the EOF-modes of dataset B as our reference modes and project the EOF-modes of dataset B onto the EOF-modes of dataset A ($DEOF^{B\to A}$). A MATLAB-script that does the complete analysis is provided as a Supplementary Material in the Sect. 3.9 on page 51 and the nomenclature used in this paper is summed up in Table 3.2.

EOF analysis	
EOF pattern of data set A	$\vec{E}_i^A$
EOF pattern of data set B	$\vec{E}_j^B$
Explained variances of EOF pattern of A	ev_i^A
DEOF analysis	
Explained variance of $\vec{E}_i^A$ projected on B	$pev_i^{A\to B}$
DEOF pattern from projection of A on B	DEOF-$i^{A\to B}$
Explained variance of DEOF-$i^{A\to B}$ in data set A	$dev_i^{A\to B}(A)$
Explained variance of DEOF-$i^{A\to B}$ in data set B	$dev_i^{A\to B}(B)$
Difference $dev_i^{A\to B}(A) - dev_i^{A\to B}(B)$	$\Delta dev_i^{A\to B}$

Table 3.2: *Nomenclature for terms in EOF and DEOF analysis*

3.4 Uncertainties of DEOF-Modes

In the discussion of the DEOF-modes it is important to know whether the difference $\Delta dev^{A\to B}$ is just a reflection of sampling uncertainties or whether it is an indication of differences in the stochastic processes underlying the two datasets. Thus we need to know the probability density function (*pdf*) of Δdev under the null hypothesis that the stochastic processes in the two datasets are the same (sampling uncertainty).

The rule of thumb for EOF analysis from *North et al.* (1982) gives the sampling uncertainty range of an eigenvalue, which is essentially the standard deviation of the *pdf* of the eigenvalue. For the DEOF analysis we have to estimate the expectation value of the difference $\Delta dev^{A\to B} = dev^{A\to B}(A) - dev^{A\to B}(B)$ as well as the spread around it. To estimate the *pdf* of DEOF analysis we followed a bootstrapping approach: As the stochastic process we chose isotropic diffusion, as it is a useful null hypothesis for climate variability and has a well-defined structure of multipoles in the EOF-modes (for details see D07). It can be described for any space and time dependent variable $\Phi(\vec{x}, t)$ with the following differential equation:

$$\frac{d}{dt}\Phi(\vec{x}, t) = c_{damp} \cdot \Phi(\vec{x}, t) + c_{diffuse} \cdot \nabla^2\Phi(\vec{x}, t) + f(\vec{x}, t) \tag{3.3}$$

where $c_{damp} < 0$ is a constant for local linear damping, $c_{diffuse}$ is the diffusion coefficient and $f(\vec{x}, t)$ is spatial and temporal white noise forcing. First, we generated a large ensemble of isotropic diffusion processes (Eq. 3.3) with different white noise realizations, the same spatial number degrees of freedom $N_{spatial}$ (*Bretherton et al.*, 1999) and the same number of

independent samples N_{time} (sampling uncertainties). We then calculated the difference of Δdev between all pairs of the ensemble. Since all members are realizations from the same stochastic process, we get an estimate of the *pdf* of Δdev for this process. We repeated this for different parameters of the isotropic diffusion process, leading to different spatial degrees of freedom (from $N_{spatial}$ from 5 up to 40). We also repeated this bootstrapping approach for different numbers of independent samples (N_{time} from 120 up to 12,000). Additionally we calculated the uncertainties of datasets that are generated from 20 unorthogonal patterns following a bootstrapping approach. The pattern we got from a random rotation of EOF-1 to EOF-20 and multiplied them with random times series to create a dataset. In this case we get $N_{spatial}$ between 5 and 9 and repeated again the bootstrapping approach for different numbers of independent samples (N_{time} from 120 up to 12,000). With both approaches we find a good approximation for the expectation and spread of the *pdf* of Δdev. The expectation value is best described by:

$$\varepsilon\left(\Delta dev_k\right) \approx dev_k \sqrt{\frac{2\, N_{spatial}}{N_{time}}} \tag{3.4}$$

where k denotes the kth DEOF mode. Thus the expectation value differs from the North's rule of thumb only by the factor $\sqrt{N_{spatial}}$. It seems reasonable to assume that the expectation of Δdev would depend on the number of independent modes in the domain ($N_{spatial}$), as we have maximized Δdev by pairwise rotation of all leading modes. The standard deviation (stdv) of the *pdf* of Δdev follows North's rule of thumb:

$$\mathrm{stdv}\left(\Delta dev_k\right) \approx dev_k \sqrt{\frac{2}{N_{time}}} \tag{3.5}$$

With Eqs. 3.4 and 3.5 we can calculate the significance of the DEOF-modes: A DEOF mode that has a Δdev larger than $\varepsilon\left(\Delta dev_k\right) + \mathrm{stdv}\left(\Delta dev_k\right)$ passes the 86% confidence level and a Δdev larger than $\varepsilon\left(\Delta dev_k\right) + 2 \cdot \mathrm{stdv}\left(\Delta dev_k\right)$ passes the 96% confidence level. In Figure 3.1 two *pdf*s of the Δdev for $N_{spatial} = 10$ (Fig. 3.1a) and $N_{spatial} = 20$ (Fig. 3.1b) are shown. Our estimated *pdf* of Δdev (dashed lines) is more conservative than the observed *pdf* (solid lines) and the cumulative distribution curve can be used to estimate the significance of a Δdev value for a given N_{time}.

3.5 Discussion of some Artificial Examples

In the following we discuss four artificial examples that increase in complexity, to illustrate how this method detects prescribed changes. The four examples are chosen in a way, that we can see how some simple types of changes are revealed in the DEOF analysis. Although, the changes in climate variability can be more complex, we will see in the subsequent section that the discussion of these simple artificial examples helps us to interpret the results of observed and simulated phenomena. The artificial examples are summarized in Table 3.3.

For all following artificial examples we choose the stochastic isotropic diffusion process (Eq. 3.3), as it is a useful null hypothesis for climate variability and has a well-defined structure of multi-poles in the EOF-modes (for details see D07). The EOF-modes of isotropic diffusion depend only on the domain dimensions and the decorrelation length. The latter is here a

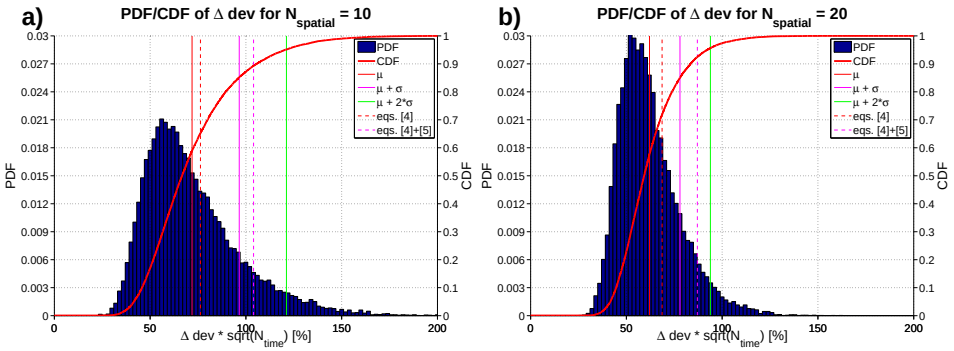

Figure 3.1: *Probability density function (pdf) (blue bars) and cumulative distribution function (cdf) (red line) of* $\Delta dev \cdot \sqrt{N_{time}}$*; all values for different numbers of independent samples* $N_{times} = 120$ *up to 12,000 are show in this Figure; the dashed lines are our estimates of the pdf according Eqs. 3.4 and 3.5; in (a) for spatial degrees of freedom* $N_{spatial} = 10$ *(according to Bretherton et al., 1999) and in (b) for* $N_{spatial} = 20$*.*

function of damping coefficient c_{damp} and diffusion coefficient $c_{diffuse}$. The EOF-1 mode is a monopole, the second and third mode are dipoles followed by multi-poles (for details see D07).

The artificial examples we discuss here are all well-defined and the differences between the two artificial datasets are known by construction. In the first two examples we discuss two datasets, which only differ in the strength of the variability of a fixed pattern. In the third example we discuss two datasets in which the position of a dominant mode of variability is different whereas in the last example the multivariate structure of the variability differs in length scale.

3.5.1 Different fixed teleconnection patterns

In the first example we add a fixed forcing pattern on top of an isotropic diffusion process:

$$\frac{d}{dt}\Phi\left(\vec{x},t\right) = c_{damp} \cdot \Phi\left(\vec{x},t\right) + c_{diffuse} \cdot \nabla^2\Phi\left(\vec{x},t\right) + f\left(\vec{x},t\right) + \pi\left(\vec{x}\right) \cdot F(t) \tag{3.6}$$

with $\pi\left(\vec{x}\right)$ as the fixed forcing pattern and $F(t)$ as temporal white noise. The isotropic diffusion processes are calculated on a 77x71 grid point domain, but for EOF analysis only the inner 37x31 grid points are chosen as the data basis to avoid boundary effects. The datasets are driven by different white noise $f\left(\vec{x},t\right)$ and $F(t)$, so that the differences between two datasets are a result of the different forcing patterns and sampling uncertainties. The datasets in this example have 2,400 independent time samples, a decorrelation length of about 9 grid points and $N_{spatial}$ of about 13.

We choose in this first example two different (orthogonal) dipoles as forcing patterns, a left-to-right dipole in dataset A and a top-to-bottom dipole in dataset B (Fig. 3.2a,b). The shape and strength of these two forcing patterns were chosen in a way that they would result as the EOF-2 modes in each dataset. Note, that in a continuous stochastic process such as isotropic diffusion (Eq. 3.3) all possible patterns of variability exist (explain a non-zero amount of variance). The left-to-right dipole pattern would explain 10.0 % in A and the top-to-bottom dipole 8.3% in B in the pure isotropic diffusion process (the background noise). By including

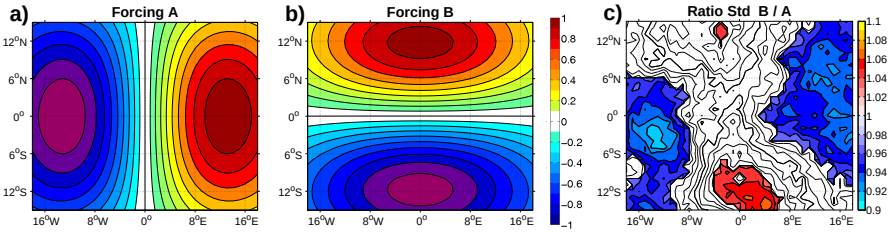

Figure 3.2: *(a) The forcing pattern, that was used in the first dataset A, in (b) in the second dataset B (colorbar in arbitrary units) and in (c) the ratio of the standard deviation of the second dataset B divided by the first dataset A is given, with shading indicating statistical significant changes according to a Fisher-F test with 90% confidence level.*

the forcing pattern in A we increase the amount of variance explained of this pattern in dataset A by 6.0% and by including the forcing pattern in B we increase the amount variance explained of this pattern in dataset B by 4.2%. Due to the different forcing patterns the variability is higher in the left and right part of the domain in A and in the top and bottom part in B (Fig. 3.2c).

We start the discussion of the differences of the spatial structure in the variability of the two datasets by comparing the leading EOF-modes (see Fig. 3.3a-f). The three leading EOF-modes of the two datasets are similar in pattern and explained variances, but the order of the patterns are different for mode 2 and 3. This reflects the fact that the left-to-right dipole pattern explains more variance in dataset A and the top-to-bottom dipole pattern explains more variance in dataset B, as we forced it by construction. These differences are quantified in the eigenvalue spectra (see Fig. 3.3g,j). It is first of all important to note, that the x-axes in Fig. 3.3g and j refer to different sets of EOF-modes in general and the eigenvalues can therefore not be compared against each other directly. The left-to-right dipole pattern of dataset A, for instance, is the mode number two in Fig. 3.3g, which is similar, but not identical to mode number three in Fig. 3.3j. So in order to be able to compare the relative importance of a specific pattern in both datasets we have to compare the ev_i^A values against the values $pev_i^{A\to B}$ or the ev_j^B values against the values $pev_j^{B\to A}$. In Figure 3.3g,j we see that projected explained variances ($pev_i^{A\to B}$ and $pev_j^{B\to A}$) do not have to be monotonically decreasing as explained variances of EOF analysis. From the projected explained variances we can further see, that the left-to-right dipole has in dataset B a much lower explained variance and the top-bottom dipole has a larger explained variance, thus showing the change in the hierarchy between EOF-2 and EOF-3, as forced by the construction of the example.

In the next step we can now find the leading DEOF patterns that maximize the differences between the two datasets by pairwise rotations of the EOF-modes. DEOF-$1^{A\to B}$ (Fig. 3.3h) is a left-to-right dipole with an explained variance of 16.0% in A and 9.3% in B, thus a difference of 6.7%, statistical significant according the test in Sect. 3.4. This pattern is very similar to the EOF-2 in A, EOF-3 in B and the forcing pattern in A. The DEOF-$2^{A\to B}$ (Fig. 3.3i) has no significant spatial structure and reflects the different white noise forcing (see further below for a discussion of significance and uncertainties). This indicates that the dataset A has one and only one pattern of variability (DEOF-$1^{A\to B}$ in Fig. 3.3h) that is more dominant in dataset A than in dataset B. In turn for dataset B we find the top-to-bottom pattern as the significant DEOF-$1^{B\to A}$ (Fig. 3.3k). The DEOF-$2^{B\to A}$ (Fig. 3.3l) is not significant and is therefore again indicating that the top-bottom dipole is the only pattern that is more dominant in dataset B

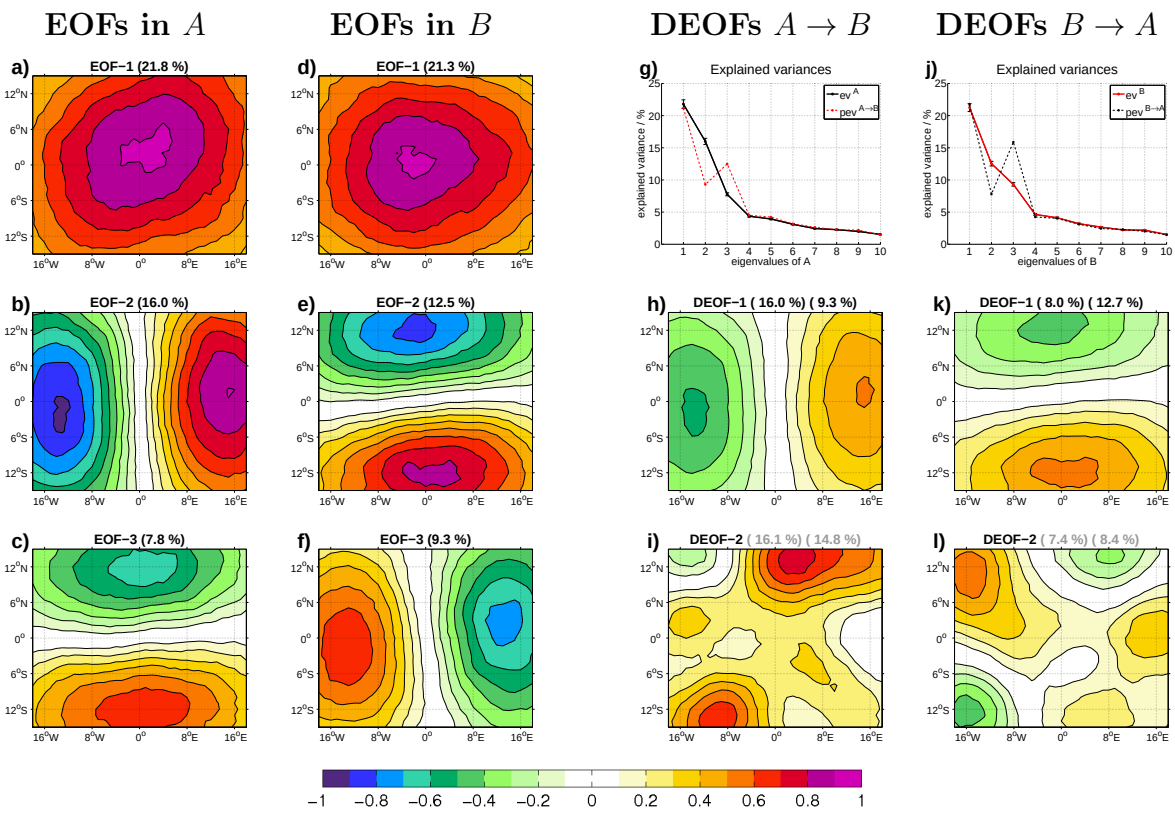

Figure 3.3: *(a)-(c) EOF patterns of dataset A (colorbar in arbitrary units); (d)-(f) EOF patterns of dataset B; explained variance is given in the header in brackets; (g) the explained variances of dataset A (black line) and explained variances of dataset A projected onto the eigenvalues of dataset B (red dashed line), the error bars show the statistical uncertainties of the explained variances due to sampling errors according to North et al. (1982); (h)-(i) DEOF$^{A\to B}$ patterns; the explained variances in A and B are given in the header in brackets, respectively, and grey values indicate that Δdev is not significant according the test in Sect. 3.4; (j) same as (g), but here showing the explained variances of dataset B (red line) and the explained variances of dataset B projected onto the eigenvalues of dataset A (black dashed line), (k)-(l) same as (h)-(i), but for the DEOF$^{B\to A}$ patterns.*

than in dataset A, as expected by construction of this example.

The significance of Δdev was calculated using the Eqs. 3.4 and 3.5 with an 86% confidence level. Alternatively we can estimate it from Fig. 3.1a,b: with a Δdev and $N_{times} = 2400$ we get $\Delta dev \cdot N_{times} = 328$. With $N_{spatial} = 13$ we find that this value is roughly at the 100% value (none of the numerical realizations produced such a large Δdev).

According to the significance test both DEOF-1 patterns have a significant Δdev, while the higher ordered DEOF patterns are all insignificant. Thus our test can separate the signal from the noise. The strength of the forcing patterns in this example was constructed in a way, that we would expect a difference of 6.0% in DEOF-1$^{A\to B}$ and of 4.2% in DEOF-1$^{B\to A}$, as mentioned above. The estimated values in this example (Fig. 3.3h,k) match the expected values relatively well.

In summary, we have illustrated in this example that the two different forcing patterns can be identified with this approach quite clearly in a qualitative and quantitative way, even though

the forcing patterns are not the dominant modes and even though they project strongly onto the background noise of isotropic diffusion. Additionally, the approach demonstrates that there are no other significant large-scale differences between the two datasets.

3.5.2 Intensification of a fixed pattern

In the second example we included a forcing pattern in the second dataset only to illustrate how the intensification of a mode is represented in the DEOF analysis. The forcing pattern (Fig. 3.4a) is a monopole located in the eastern part of the domain, which increases the variance in this region (Fig. 3.4b). The shape of the pattern was chosen to be projecting onto both EOF-1 and EOF-2 of the isotropic diffusion process (domain-wide monopole and a left-to-right dipole) to illustrate how a forcing pattern can be detected that does not project on one EOF-mode only.

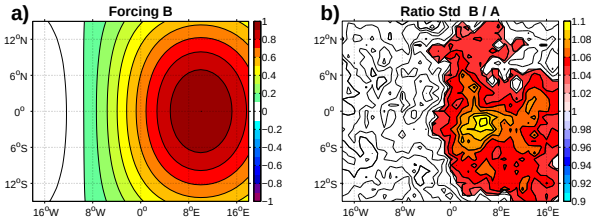

Figure 3.4: *Same as Fig. 3.2, but here for the example in Sect. 3.5.2.*

The EOF-modes (Fig. 3.5a-d) of the two datasets are quite similar, but the comparison of the eigenvalue spectra reveals some differences. The DEOF-1$^{B\to A}$ (Fig. 3.5h) is the only significant DEOF pattern and no other significant DEOF patterns exist in dataset A. Thus the DEOF analysis is able to reveal the forcing pattern even though its original structure is not projecting on one particular EOF-mode and it shows that only one pattern is amplified in dataset B. The increase in variance in DEOF-1$^{A\to B}$ (Fig. 3.5f) is not significant and reflects the different white noise forcing.

The experiment can also be repeated with more than one fixed forcing pattern included in Eq. 3.6 for dataset B, to test if the intensification of several modes can be detected. The method can clearly present several fixed forcing patterns, assuming that they are orthogonal to each other (see Supplemental Figure 3.15 and 3.16 on page 48).

3.5.3 Shift of the location of a fixed pattern

In the third example we introduce a forcing pattern that shifts the location between dataset A to dataset B (Fig. 3.6a,b), so that the forcing weakens in one part and strengthens in the other (Fig. 3.6c) and describes an eastward shift of the forcing by 16 grid points. The two EOF-1 modes are slightly different in shape, with the center more to the left in dataset A and more on the right in B (Fig. 3.7a,c), consistent with the forcing patterns. The eigenvalue spectra reveal differences between the two datasets in EOF-1 and EOF-2 (Fig. 3.7e) and the DEOF-1 of both projections reveal larger and significant differences. Thus in this example, the DEOF-1 patterns of both projections reveal a dominant pattern in each dataset, together illustrating the shift in a pattern.

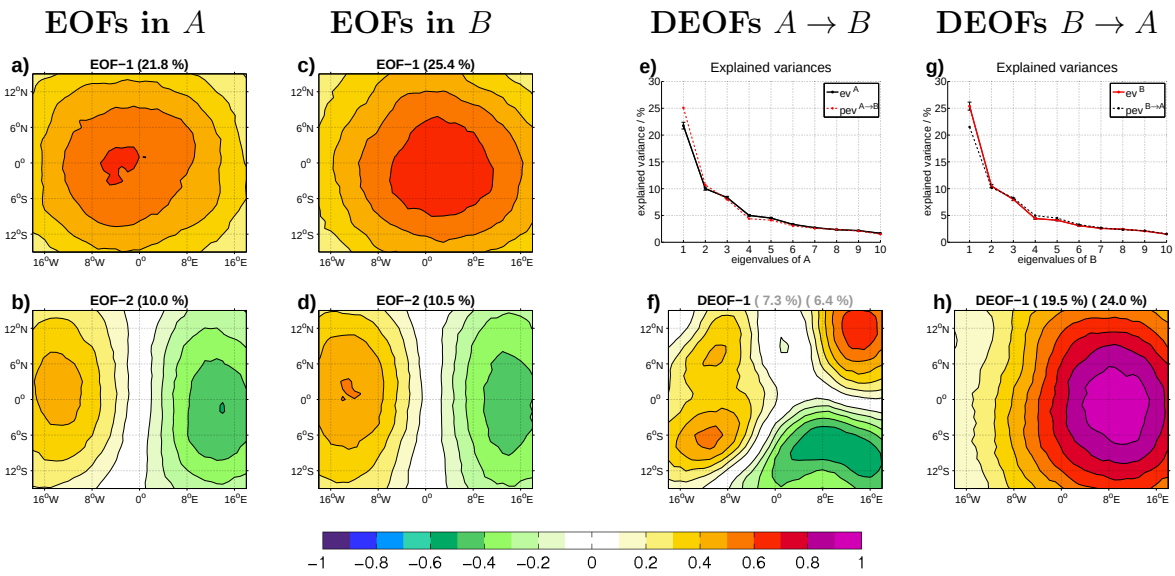

Figure 3.5: *Same as Fig. 3.3, but here for the example in Sect. 3.5.2.*

However, we have to note that the pattern shape of the DEOF-1 patterns do not quite match the forcing patterns. This can be understood when we think about how this method works: A DEOF pattern with the shape of the forcing pattern would not maximize in this case the difference in explained variance between the two datasets, because it also has amplitude at those locations, where the other dataset has more explained variance due to the other forcing pattern. So the interpretation in this case becomes more complicated. Indeed if we compare the first example with two different (orthogonal) forcing patterns with this example here, we can notice that the two patterns (before and after the shift) here are not orthogonal to each other (they project onto each other). In principle the first example can also be interpreted as a shift in one pattern: The forcing pattern in dataset A is the forcing pattern in dataset B rotated by 90°. The shift in this first example is more complete, leading to two (before and after the shift) orthogonal patterns.

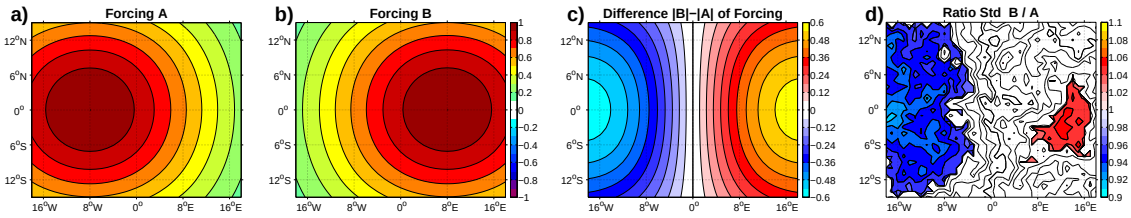

Figure 3.6: *Same as Fig. 3.2, but here for the example in Sect. 3.5.3; additional in (c) the difference between the two forcings $B - A$.*

So the signature of a shift of one pattern is that we have a significant DEOF-1 mode in both projections, each representing a pattern that is similar to the pattern that is shifted. The fact that the patterns before and after the shift are not orthogonal to each other will lead to the DEOFs being slightly different from the pattern that is shifted. Thus we get two patterns, each of them mostly similar to one "sign" of the ratio of standard deviation (Fig. 3.6d). Other examples with a shifted dipole pattern are shown in the Supplemental Figure 3.17 to 3.20.

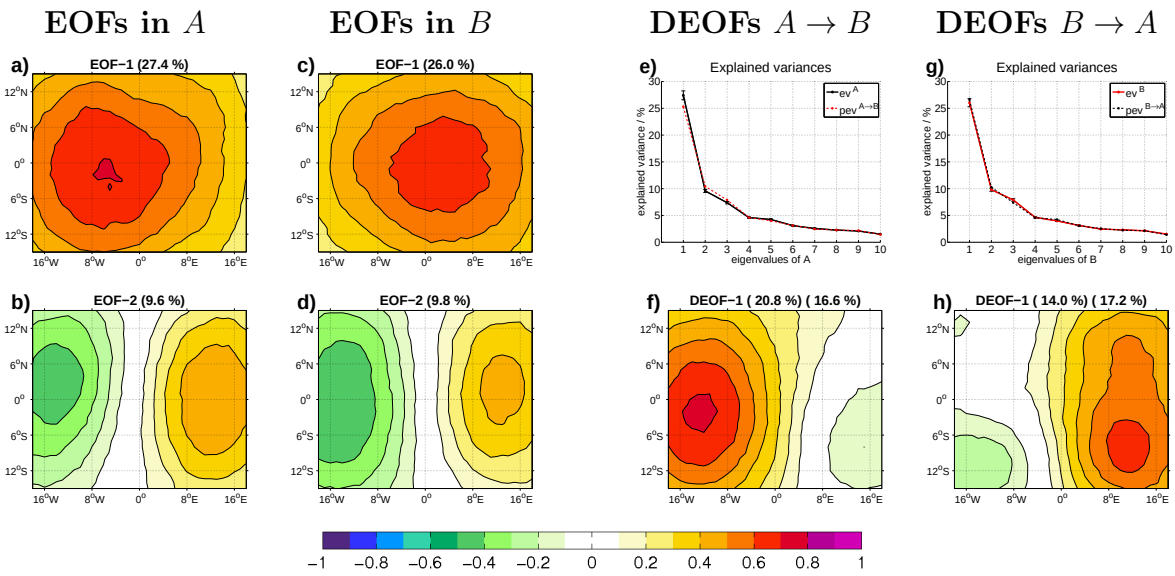

Figure 3.7: *Same as Fig. 3.3, but here for the example in Sect. 3.5.3.*

3.5.4 A Multivariate difference: A difference in length-scale

In this last artificial example we compare two pure isotropic diffusion processes with different length-scales. So no fixed forcing patterns are included. This example can illustrate that differences in the EOF-modes do not always have to be interpreted as a difference in a fixed pattern, but may sometimes reflect multivariate differences in the stochastic high-dimensional process underlying the dataset. In comparison with the above examples the discussion of this example illustrates the characteristic signatures of multivariate (high-dimensional) differences.

In dataset A we choose a weaker damping and diffusion constants than in dataset B, which leads to a shorter decorrelation length (about 7 grid points) in dataset A and a larger decorrelation length (about 10 grid points) in dataset B. The pattern shape of the EOF-modes is similar in both datasets (Fig. 3.8a-f), which we also see in the eigenvalues, as the black dashed line of Fig. 3.8j is nearly the same as the black solid line in Fig. 3.8g (same for the two red lines). But the amount of explained variance is different. The shorter decorrelation length in dataset A leads to larger number of spatial degrees of freedom compared to dataset B and subsequently more EOF-modes are needed to explain the same amount of variance. Therefore the leading EOF-modes have to explain less variance and the higher order EOF-modes have to explain more variance to sum up to 100%.

The first three leading DEOF$^{B\rightarrow A}$ are similar to the first three EOF patterns and are all significantly stronger in dataset B than in dataset A. This is quite different from the previous examples, where we always found only one pattern that was more dominant in one of the datasets. It thus suggests that the differences in the two datasets are of a higher-dimensional order and are most likely not best described by the change in one, two or three patterns but are more likely a reflection of a change in the stochastic high-dimensional process underlying the dataset, such as a change in decorrelation length. In turn the DEOF$^{A\rightarrow B}$ are all of small-scale structure and reflect the relative increase in variance of small-scale variability, with first two DEOF$^{A\rightarrow B}$ being significant (Fig. 3.8h,i).

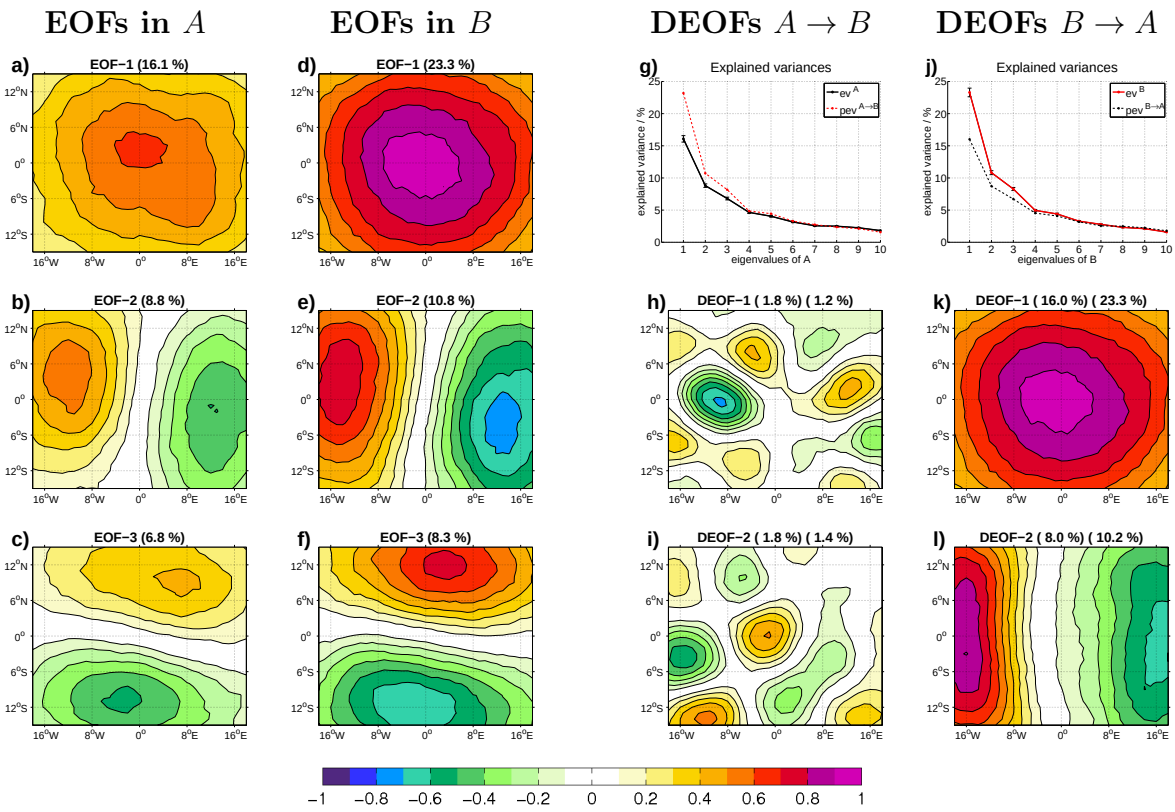

Figure 3.8: *same as Fig. 3.3, but here for the example in Sect. 3.5.4.*

3.5.5 Summary

We illustrated the application of the DEOF analysis with a series of well-defined examples. By analyzing the spectrum of eigenvalues in comparison with the projected explained variances we can see how distinct the EOF patterns are and with the DEOF patterns we are able to specify the pattern that most strongly gains or loses importance and to quantify how much explained variance is gained or lost.

The discussion of the idealized examples is summarized in Table 3.3. The table can be used as look up table to identify the structures that describe the difference in real data analysis problems. If a single mode or teleconnection is amplified in dataset B compared to a dataset A it appears as the DEOF-1$^{B\rightarrow A}$, but no significant DEOF$^{A\rightarrow B}$ will appear (second example in Table 3.3). If a pattern shifts its position in dataset B compared to its position in dataset A, then both the leading DEOF$^{A\rightarrow B}$ and the DEOF$^{B\rightarrow A}$ pattern together highlight the shift (third example in Table 3.3). And last a change in the multivariate structure is reflected in having several significant DEOF patterns in either one projection or in both, depending on the nature of the multivariate changes (fourth example in Table 3.3).

Example Name	**Type of differences**	**DEOF characteristics**
3.5.1 Different fixed teleconnection patterns	One leading mode in each data set is different from the other data set.	One or more eigenvalues will be more dominant in both datasets relative to the other dataset. One (only one!) DEOF-mode will be significantly dominant in each of the two datasets.
3.5.2 Intensification of a fixed pattern	One leading in one data set mode is stronger than in the other	One or more eigenvalues will be more dominant in one dataset relative to the other dataset. One (only one!) DEOF-mode will be significantly dominant in the one dataset relative to the other dataset.
3.5.3 Shift of the location of a fixed pattern	One leading mode has different spatial location in the two datasets.	One or more eigenvalues will be more dominant in both datasets relative to the other dataset. One (only one!) DEOF-mode will be significantly dominant in each of the two datasets. The DEOF-modes peak at the locations where the variance is increased most relative to the other dataset, marking the location shift.
3.5.4 A Multivariate difference: A difference in length-scale	The length scale of the multivariate stochastic process is different in the two data sets	Most leading eigenvalues will be more dominant in one dataset relative to the other dataset. The higher-ranked eigenvalues of the other data set maybe more dominating than in the first dataset. Two or more DEOF-modes will be significantly dominant in the first dataset relative to the other dataset. More than one large-scale leading EOF-mode will be more dominant than in the other dataset.
3.6.1 Sea Level Pressure over the North Atlantic and Europe in winter	Mainly a pattern shift in the 1.EOF as in 3.5.3 and Fig. 3.18	One eigenvalue dominates in both datasets relative to the other dataset. One DEOF-mode significantly dominates in each of the two datasets. The DEOF-modes peak at the locations where the variance is increased the most relative to the other dataset, marking the location shift.
3.6.2 Sea Level Pressure of the southern hemisphere in DJF	Mainly a pattern shift in the 1.EOF as in 3.5.3 and Fig. 3.20	One eigenvalue dominate in both datasets relative to the other dataset. One DEOF-mode significantly dominates in each of the two datasets. The DEOF-modes peak at the locations where the variance is increased the most relative to the other dataset, marking the location shift.
3.6.3 Northern hemispheric winter surface temperature	Mainly a pattern shift in the 1.EOF as in 3.5.3 and Fig. 3.18, but also some difference in the patterns as in 3.5.1	Several eigenvalues dominate in both datasets relative to the other dataset. One DEOF-mode significantly dominates in each of the two datasets. The DEOF-modes peak at the locations where the variance is increased the most relative to the other dataset, marking the location shift.
3.6.4 North Pacific SST	Mainly an intensification in parts of 1.EOF (or the variance in this region) as in 3.5.2, but also some similarity to a shift as in 3.5.3.	Two eigenvalues dominate in the 21C dataset relative to the 20C dataset. One DEOF-mode significantly dominates in each of the two datasets. The DEOF-modes peak at the locations where the variance is increased the most relative to the other dataset. With the 21C DEOF-mode being more dominant.
3.6.5 Precipitation over the tropical Indo-Pacific	Mainly a multi-variate change in the modes of variability as in 3.5.4, with some characteristics of a shift in the 1.EOF as in 3.5.3	Several eigenvalues dominate in the 20C dataset relative to the 21C dataset and one eigenvalue of 21C dominates over the 20C dataset. Two DEOF-modes significantly dominate in each of the two datasets.

Table 3.3: *Summary of all examples*

3.6 Literature Examples about Climate Change Simulations

In this section we discuss examples from the literature to illustrate how this method relates to other approaches. In all cases we discuss previous studies that analyzed the changes in the spatial structure of climate variability from 20th century control climate to future 21th century global warming scenarios with different methods. Some of these methods are based on EOF-modes and others are based on alternative methods. In all examples the discussion is about the change of modes under climate change. Thus to test our method we try to reproduce with our method the results of several previous studies in a multi-model ensemble from the CMIP3 data base. In the following examples the dataset A refers to the period 1950 to 1979 in the present day or 20th century control climate (dataset 20C) and dataset B to the period 2070 to 2099 future 21th century or global warming scenario climate (dataset 21C). The focus in the discussions will be on illustrating the robustness of the method introduced in this study and not on arguments about changes in the modes of variability in the future, although the discussion may contribute to the latter.

3.6.1 Sea Level Pressure over the North Atlantic and Europe in winter

Hu and Wu (2004) investigated the two centers of action of the North Atlantic Oscillation (NAO) in winter SLP of the coupled ECHAM4/OPYC3 climate model, which they defined by the strongest negative correlation between two grid points in this region, and found a northeastward shift of both centers of the NAO in global warming.

The EOF analysis in winter SLP of the CMIP3 multi-model ensemble shows in both periods as EOF-1 the typical NAO pattern (Fig. 3.9a,b), with only small differences: The negative pole gets stronger over the Barents Sea in 21C, both centers move a little bit to the east and the explained variance is 2.1% higher in 21C as in 20C. These changes appear to be small by visual inspection or pattern correlation (0.99).

The DEOF-$1^{20C \to 21C}$ (Fig. 3.9e) shows a significant decrease in explained variance of 2.6% in 21C in a dipole structure over the western Atlantic. The DEOF-$1^{21C \to 20C}$ (Fig. 3.9f) shows a significant increase in explained variance of 4.3% in a dipole structure over the polar region and the midlatitudes of the east Atlantic and Eurasia. This structure with significant DEOF-1 in both projections is similar to the artificial examples with the pattern shift (Sect. 3.5.3 or Supplemental Fig. 3.17 and 3.18): Losing relevance over the western Atlantic in 20C and gaining relevance over the Polar Regions, the eastern Atlantic and Eurasia in 21C. These DEOF-1 patterns together mark the northeastward shift of the NAO pattern in global warming, as already mentioned in *Hu and Wu* (2004) and fit quite well to the change in variability in Fig. 3.10. Additionally we can see, that the NAO pattern strengthens strongest over the Barents sea, a region that could be important for the Northern Hemisphere in global warming, as also mentioned in *Petoukhov and Semenov* (2010). In summary, the DEOF analysis basically confirms the *Hu and Wu* (2004) results, illustrating the robustness of the method in this context.

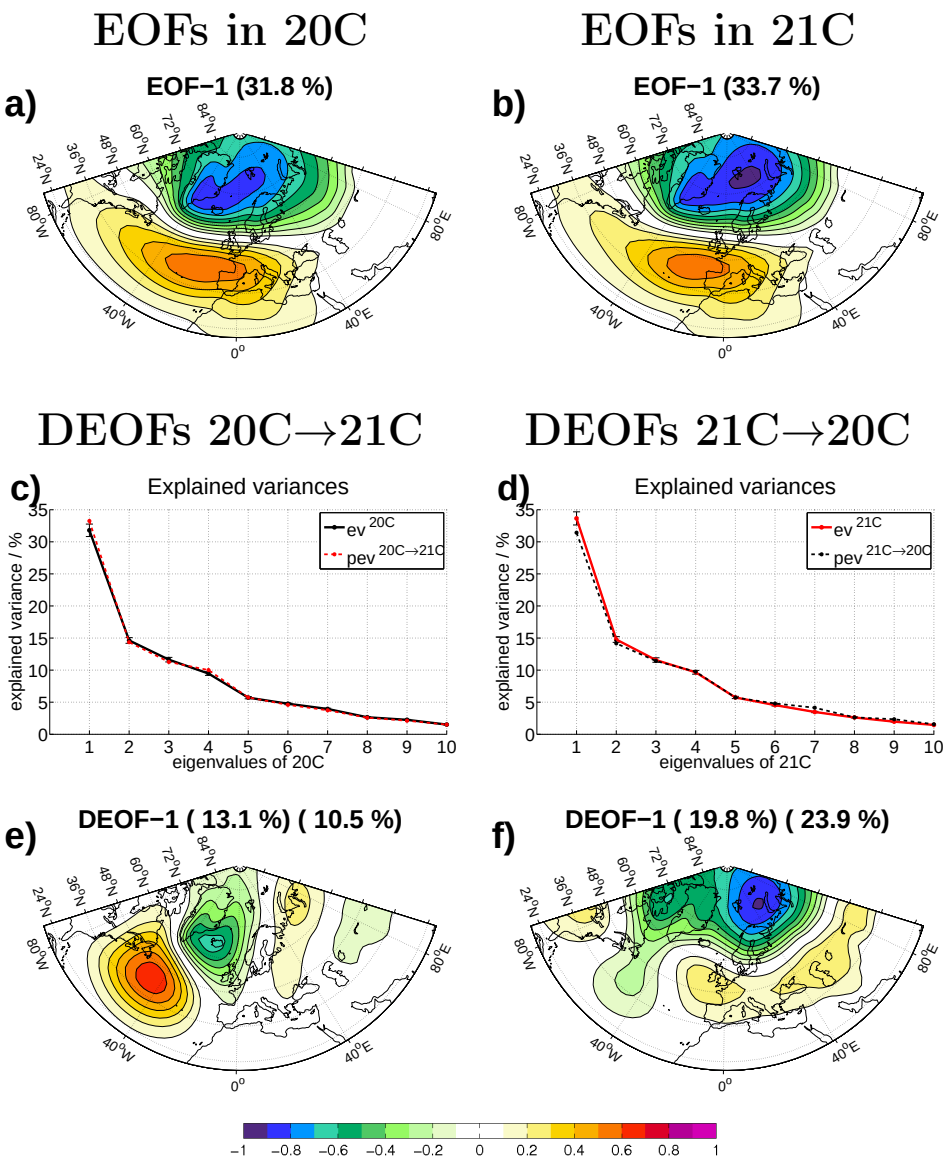

Figure 3.9: *Same as Fig. 3.3, but here for DJF SLP over the Atlantic region in the periods 1950-1979 (20C) compared with the period 2070-2099 (21C), as discussed in Sect. 3.6.1.*

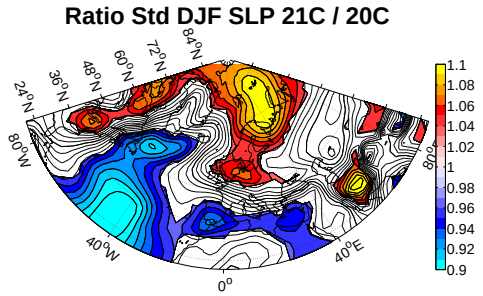

Figure 3.10: *Ratio of the standard deviation of 21C divided by 20C for DJF SLP over the Atlantic region, with shading indicating statistical significant changes according to a Fisher-F test with 90% confidence level.*

3.6.2 Sea Level Pressure of the Southern Hemisphere in DJF

Kidston et al. (2010) analysed the position of the Southern Hemispheric eddy-driven jet stream by looking at the maximum in zonal mean near surface zonal wind speed in the CMIP3 data base and found a pole-ward shift of the jet under global warming, which also leads to a pole-ward shift of the Southern Annular Mode (SAM).

In the EOF analysis of DJF SLP in the Southern Hemispheric higher latitudes the EOF-1 pattern (SAM, Fig. 3.11a,b) is by far the most dominant but loses 4.5% of its explained variance in 21C in comparison to 20C. The annular pattern shifts pole-ward in 21C and the amplitude weakens a little bit. Again these changes can hardly be seen by visual inspection or by pattern correlation (0.99). The DEOF-$1^{20C \rightarrow 21C}$ (Fig. 3.11e) shows an almost annular pattern that has a 7.7% higher explained variance in 20C than in 21C. This pattern is located further equator-ward than the EOF-1 pattern. The DEOF-$1^{21C \rightarrow 20C}$ (Fig. 3.11f) is also almost annular but with a maximum over the Pacific and has a 4.2% higher explained variance in 21C than in 20C. This structure is more pole-ward than the EOF-1 pattern. In comparison with the artificial example in Sect. 3.5.3 and Supplemental Fig. 3.19 and 3.20 it becomes clear, that these two DEOF pattern together reveal the pole-ward shift of the SAM pattern, consistent with the study of *Kidston et al.* (2010). Again it illustrates the robustness of the DEOF analysis. Additionally, it could be noted here, that this shift is most pronounced over the South Pacific.

3.6.3 Northern Hemispheric winter surface temperature

The third example is the winter T_{surf} of the Northern Hemisphere. In *Keeley et al.* (2008) T_{surf} was investigated in a 2xCO2 and 4xCO2 slab ocean run in comparison to a control run. EOF analysis was performed to find the patterns of variability and pattern correlations between individual EOF-modes to find the differences in the modes between the control and increased CO2 runs. They found no significant changes in terms of dominance or spatial pattern in the modes of variability.

The leading EOF-modes in the CMIP3 multi-model ensemble in both the control 20C simulations and the 21C scenario simulations (which corresponds roughly to the analysis of *Keeley et al.*, 2008) are shown in Fig. 3.12. The EOF-1 modes in both centuries are mostly the manifestation of the NAO in T_{surf} (*Hurrell and Loon*, 1997). The leading EOF-modes in the multi-model ensemble simulations are indeed very similar. Not only are the patterns quite similar (pattern correlation = 0.94), but also are the explained variances not too different. However, the eigenvalue spectra of the 20C and 21C multi-model ensemble dataset relative to the projected eigenvalues reveal some quite significant difference, also in the spatial structure.

The DEOF-$1^{20C \rightarrow 21C}$ (Fig. 3.12e) is a multi-pole structure, with strongest amplitude over the Barents Sea, the Labrador Sea and Alaska. This pattern shows a significant decrease of explained variance of 2.9% (a reduction of one third relative to its eigenvalue) from 20C to 21C. The DEOF-$1^{21C \rightarrow 20C}$ (Fig. 3.12f) projects strongly on the EOF-1 pattern, but is shifted more to the east over Eurasia. This pattern shows a significant increase in explained variance of 2.8% from 20C to 21C, which represents a 30% increase relative to the explained variance of this mode in the 20C control simulation. Both DEOF-1 modes together reveal an eastward shift of the NAO manifestation in T_{surf} in 21C, with an increase in dominance over Asia and a decrease over the Barents Sea and Scandinavia. This eastward shift could be expected from

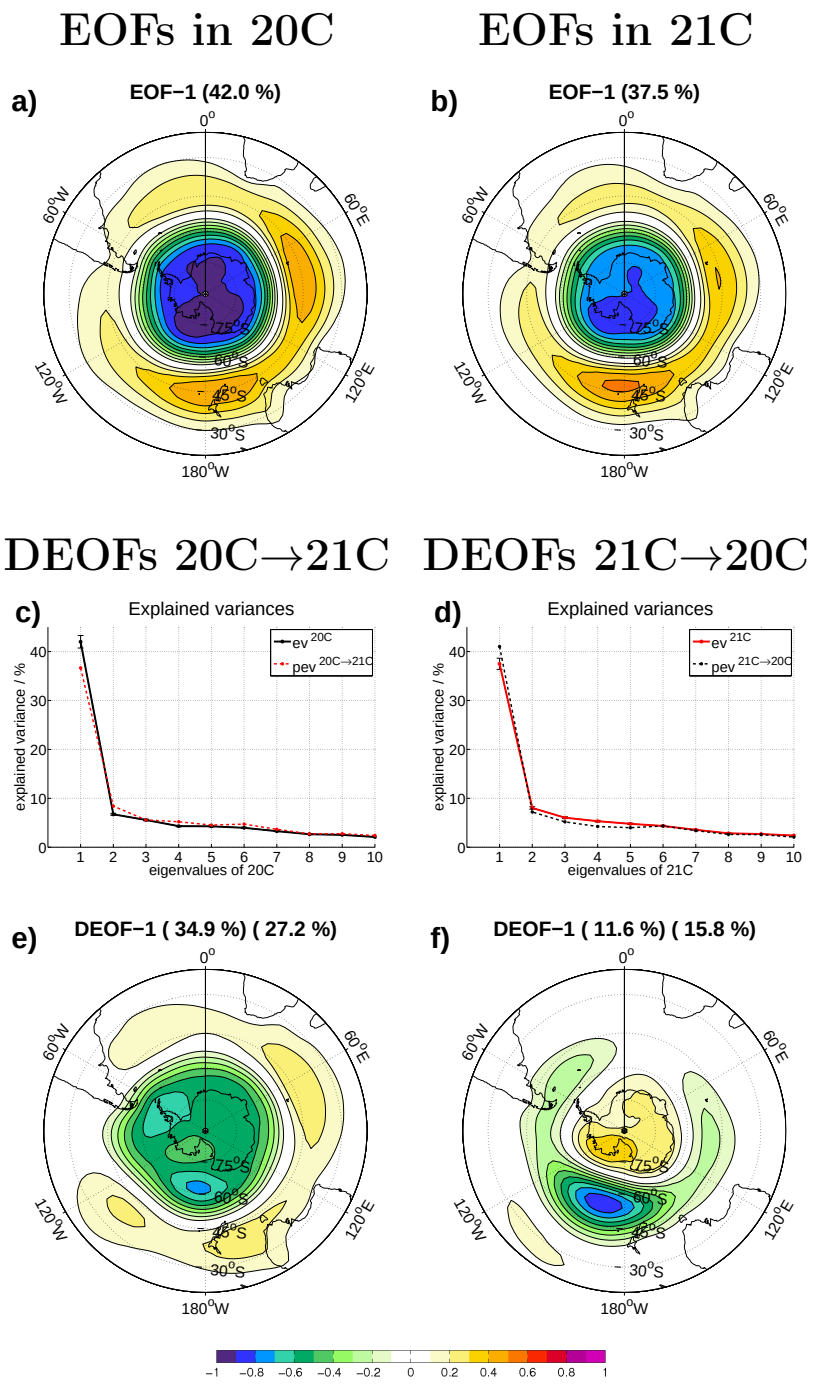

Figure 3.11: *same as Fig. 3.9, but here for Southern Hemispheric SLP in DJF as discussed in Sect. 3.6.2.*

shift of NAO in winter SLP in Sect. 3.6.1. But also the changed snow and sea ice conditions seem to have an effect on T_{surf}, by reducing the amount of variability over Alaska and the Labrador Sea in 21C.

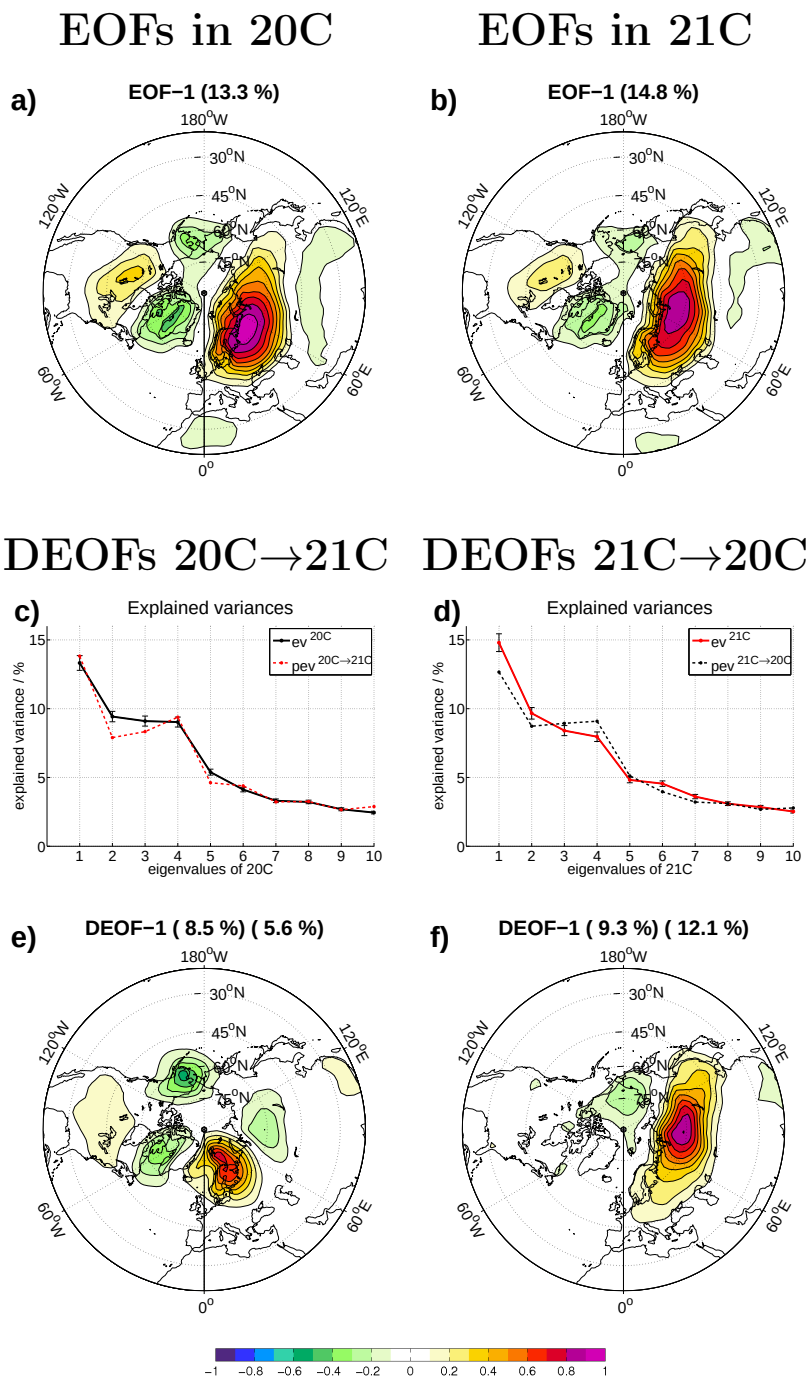

Figure 3.12: *same as Fig. 3.9, but here for Northern Hemispheric T_{surf} in DJF as discussed in Sect. 3.6.3.*

Thus in contrast to the study of *Keeley et al.* (2008) our method reveals significant changes in the spatial pattern of the modes variability. This may, to some degree, be due to the larger database used here (24 CMIP3 models) and using transient global warming simulations, in contrast to *Keeley et al.* (2008) who used only one 2xCO2 and 4xCO2 global warming simulation of one climate model. But it also illustrates the robustness of the method presented here.

3.6.4 North Pacific sea surface temperature

The next example is SST of the North Pacific for the periods 1950-1999 (20C) and 2050-2099 (21C). We choose here 50 years long periods, because the Ocean has a longer decorrelation time, thus fewer independent samples. The Pacific Decadal Oscillation (PDO) is the dominant mode of variability of North Pacific SST and in *Furtado et al.* (2011) its change in global warming was investigated in the same multi-model ensemble of 24 IPCC models from the CMIP3 database. They did not mention which method they used to compare the two EOF sets, but found no significant changes in the patterns of variability.

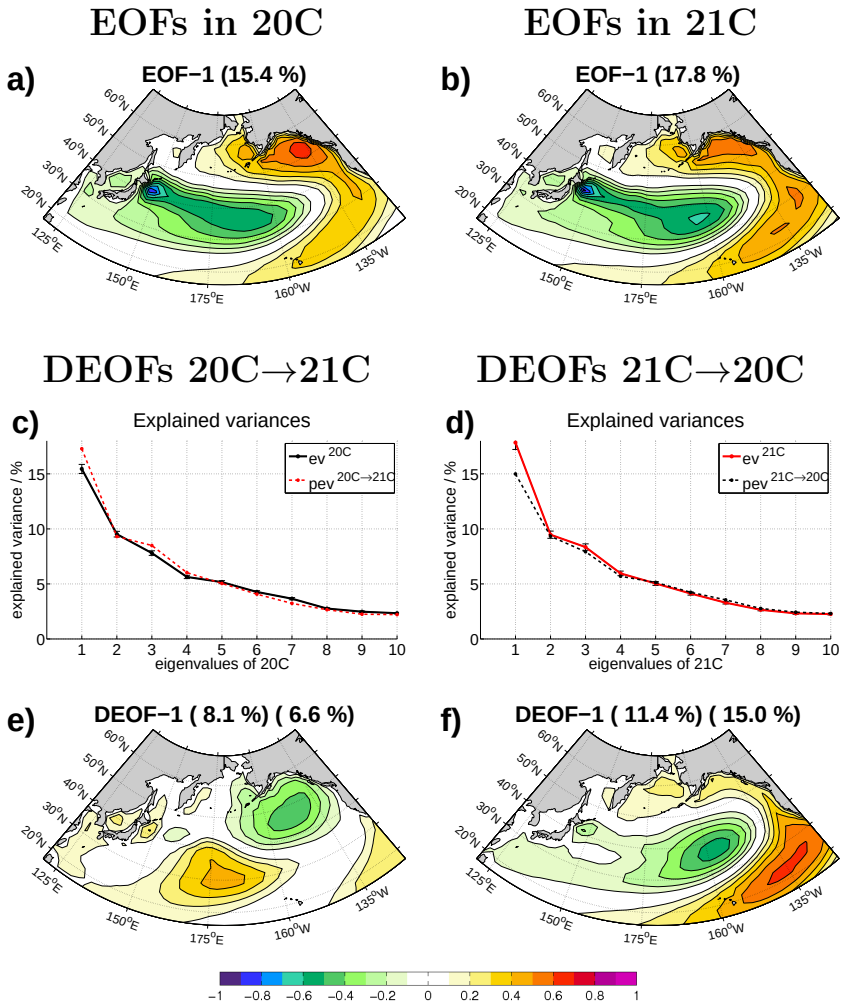

Figure 3.13: *same as Fig. 3.9, but here for North Pacific SST as discussed in Sect. 3.6.4.*

In both centuries the EOF-1 (Fig. 3.13a,b) represents the PDO and again the modes are quite similar in pattern (pattern correlation = 0.98) and explained variances. However, the DEOF-$1^{21C\rightarrow 20C}$ (Fig. 3.13f) finds a significant increase in variance in a pattern centered in the subtropical southeast corner of the domain. This modes variance is increasing by roughly one third relative to its variance in the 20C simulations. The overall change in modes is somewhat similar to the artificial example 2 with the intensification of a pattern. The strong variability increase over the subtropical region further supports this view (not shown). However,

the change in modes in the North Pacific also has some aspects of a shift in a pattern. This is supported by fact that the DEOF-1$^{20C\to21C}$ and DEOF-1$^{21C\to20C}$ both project onto the EOF-1, but both representing different aspects or locations of the EOF-1 mode. Thus it could be interpreted as a shift in the teleconnection of this mode from the extra-tropics more to the eastern subtropics of the North Pacific.

3.6.5 Precipitation over the tropical Indo-Pacific

Hu et al. (2012) analysed the global warming response of tropical precipitation in the CCSM3 climate model in all four seasons and compared EOF-modes of the control scenario with the EOF-modes of the A1B scenario. They found some small differences in the details, but overall a high pattern correlation of the leading EOF-modes let them conclude that there are no significant differences. Here we will focus our analysis on the Indo-Pacific region as the leading modes of variability of tropical precipitation are all located in this region (see Fig. 11 and 12 of *Hu et al.*, 2012), but the results would be the same, if we would take the whole tropics.

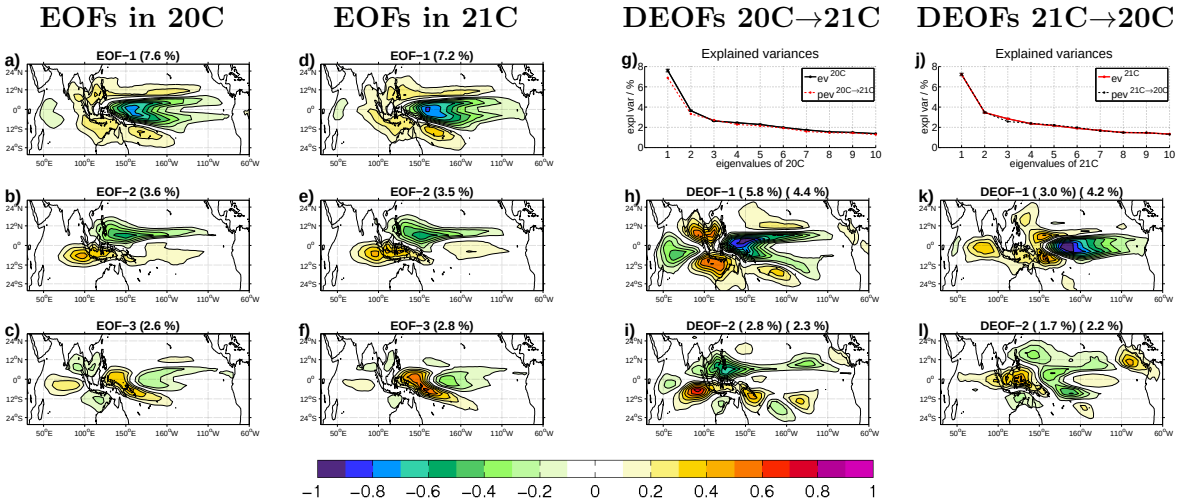

Figure 3.14: *same as Fig. 3.9, but here for Tropical Indo-Pacific precipitation as discussed in Sect. 3.6.5.*

The variability of precipitation has a small decorrelation length, thus has a lot of small scale variability (Fig. 3.14a-f). The projected eigenvalues show that the pattern shape has changed. The DEOF-1$^{21C\to20C}$ (Fig. 3.14k) is a multi-pole structure quite different from the EOF-1 pattern that has a significant increase in variance. The variance in this mode increases by about 40% relative to its value in the 20C simulations. Together with the DEOF-1$^{20C\to21C}$ (Fig. 3.14h), which is mostly the EOF-1 pattern losing relative importance in the 21C simulations, this illustrates an eastward shift of the ENSO related precipitation, in agreement with *Chung et al.* (2013). Both DEOF-2 (Fig. 3.14i,l) also show significant changes that project on EOF-2 and show small-scale changes in the pattern shape. As all leading DEOF patterns are significant, this example illustrates that a multivariate system as a whole can change and it is not enough to look at the dominant mode only. But this example has also some similarity to the artificial example in Sect. 3.5.3 (shift in location). Here it is mostly an eastward shift in the dominant variability pattern.

3.7 Summary and Discussion

In this study we introduced a method based on EOF analysis to quantify the differences in the modes of variability in two datasets, which is called DEOF analysis. It can be used to compare modes of variability in climate models with observations or find the changes in the modes of variability in climate change scenarios. We can summarize the DEOF analysis as a simplified recipe for the comparison of modes, see Table 3.4. The first feature of this method, the projected explained variances, reveals which EOF patterns are most distinct in two datasets. The second feature, the DEOF patterns, are the patterns with the largest differences in explained variance between two datasets and is also able to find small-scale changes in the modes of variability. The biggest advantage of this method is that it considers the changes in all patterns of variability instead of only the leading mode.

Step	Comment
1. Define anomalies for both data sets.	
2. EOF analysis for both data sets.	Use identical domains and define eigenvalue variances in terms of relative explained variance [%].
3. Define the EOF-modes of one dataset as the reference modes.	This defines the reference modes (patterns) on which you base your analysis.
4. Project the reference EOF-modes onto the other dataset.	This will allow you to compare the eigenvalue spectrum of the reference dataset with the projected explained variances of these modes in the other dataset.
5. Compute the DEOF-modes by pairwise rotation to maximize the differences in explained variance of this mode in the two data sets.	The DEOF-modes represent the modes in the reference dataset that have the largest difference in explained variance relative to the other dataset.
6. Repeat steps 3 to 5 with the other dataset as the reference modes.	If you first projected A on B, then now project B on A.
7. Compare the results with idealized examples to understand the nature of the differences.	The idealized examples will help you to formulate a simple model to describe the differences.
8. Do further analysis to verify findings.	No single statistical analysis will be sufficient. Use other statistical methods and, most importantly, sensitivity experiments or theoretical considerations to backup the results.

Table 3.4: *DEOF-analysis recipe*

We further illustrated the method on the basis of several well-defined constructed examples. These examples do not only demonstrate the application of the DEOF method, but are also role models for formulating simple hypothesis for the differences in modes of variability between two datasets of real data analysis. Table 3.3 can basically be used as a look up table for the characteristics of the spatial variability differences. These characteristics are mainly: an intensification, a shift or a multivariate difference.

In the application of the DEOF analysis to literature examples we demonstrated that we could reproduce the main findings of the previous studies. Furthermore, we could also demonstrate that the DEOF analysis may in some aspects be more powerful than previously used

methods. We detected the northeastward shift of the NAO pattern as in the paper from *Hu and Wu* (2004) and beyond that we could also find how much explained variance is gained and lost in certain regions. We could also find the pole-ward shift of the SAM with the DEOF method as described in *Kidston et al.* (2010), and beyond that we found that this is strongest over the Pacific Ocean. Further we investigated changes in the modes of Northern Hemispheric winter T_{surf} in global warming and found an eastward shift in the dominant mode, which is the manifestation of the NAO in T_{surf}. From the northeastward shift of NAO in SLP we expected this shift in the dominant mode of T_{surf}, which *Keeley et al.* (2008) could not find in a similar analysis. We think that their conclusion being different from ours is on the one hand based on the fact that they use only one model instead of a multi-model ensemble to investigate the changes and on the other hand that their method (pattern correlation) aims on changes in the large scale pattern structure and while our method can also detect local changes in the patterns. For the modes of North Pacific SST we could also find in contrast to *Furtado et al.* (2011) significant changes: A shift of the eastern part of the PDO and a strengthening in the southeastern part of the PDO. *Furtado et al.* (2011) did not made any statement about the method they used to compare the modes of variability, thus again we think their conclusion being different from ours is mostly based on the fact that their method aims more on the large scale changes in the modes of variability while our method can also detect local changes in the patterns. In the modes of precipitation we found an eastward shift in the ENSO related precipitation (EOF-1) in agreement with *Chung et al.* (2013), but beyond that also significant changes in the higher ordered modes, thus in the whole multivariate structure.

Finally, we need note that although we think that the DEOF analysis method is a powerful new tool to help evaluate the differences in the spatial structure of climate variability, the interpretation of DEOF-modes or EOF-modes is complicated (see e.g. *Dommenget and Latif*, 2002). Alternative statistical methods, model sensitivity simulations and theoretical considerations of the climate processes involved should accompany any analysis of these complicated multivariate datasets.

Acknowledgements

We acknowledge the individual modeling groups, the Climate Model Intercomparison Project (CMIP3). This work was supported by the Deutsche Forschungsgemeinschaft (DFG) through project DO1038/5-1 and the ARC Centre of Excellence in Climate System Science (CE110001028). We thank Jan Harlaß, Klaus Getzlaff, Katja Lorbacher and Gang Wang for discussion and useful comments.

3.8 Supplemental Figures

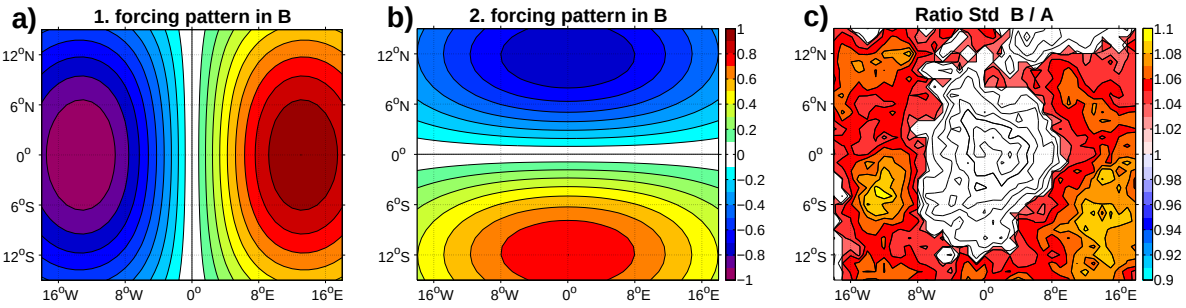

Figure 3.15: *Additional experiment for the example in Sect. 3.5.2, but with two fixed patterns intensified in dataset B.* ***Part 1****: Forcing patterns and difference in variability. Same structure for the figure panels as in Fig. 3.2: (a)-(b) the two forcing patterns included in B (instead of only one as in Sec. 3.5.2); (c) due to these two forcing patterns, dataset B has a higher variability, except in the middle of the domain, where the difference is not significant.*

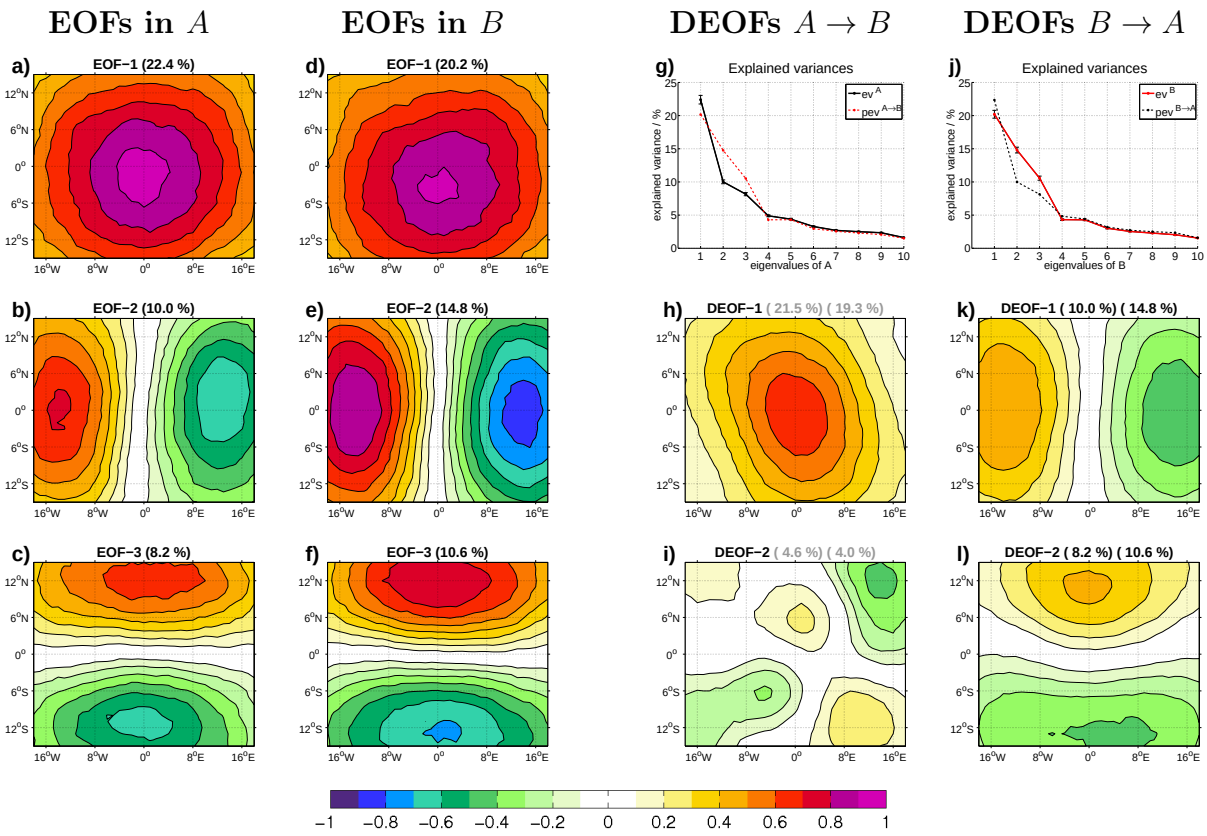

Figure 3.16: *Additional experiment for the example in Sect. 3.5.2, but with two fixed patterns intensified in dataset B.* ***Part 2****: EOF and DEOF analysis. Same structure for the figure panels as in Fig. 3.3.*

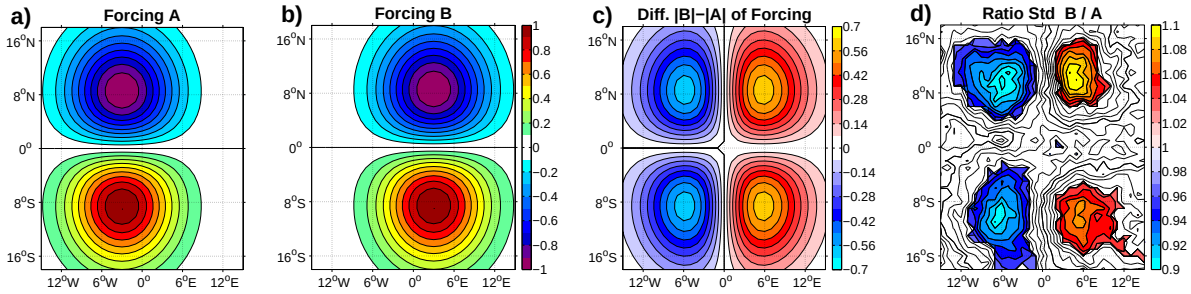

Figure 3.17: *Additional experiment for the example in Sect. 3.5.3, but with a dipole pattern shift from west (A) to east (B).* ***Part 1****: Forcing pattern and difference in variability. Same structure for the figure panels as in Fig. 3.2: (a)-(b) the dipole forcing pattern shifts location orthogonal to the line between the two poles, i.e. a shift to the right of 6 grid points in this case; (c)-(d) the difference between the two forcing pattern is a quattro-pole structure, also in the ratio of the standard deviation.*

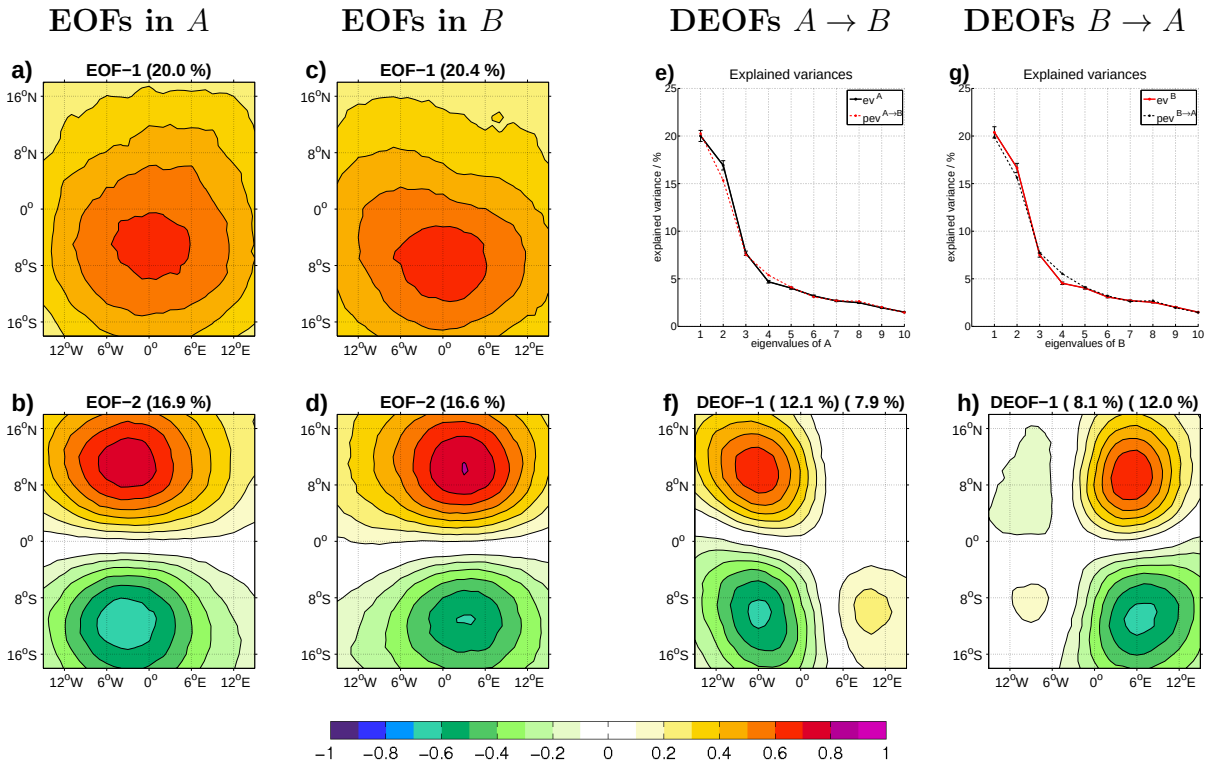

Figure 3.18: *Additional experiment for the example in Sect. 3.5.3, but with a dipole pattern shift from west (A) to east (B).* ***Part 2****: EOF and DEOF analysis. Same structure for the figure panels as in Fig. 3.3: (f), (h) as in the example in section 3.5.3 both DEOF-1 pattern have to be considered together: The DEOF-1$^{A\to B}$ shows where the EOF-2 pattern has weakened and the DEOF-1$^{B\to A}$ where the EOF-2 pattern has strengthened, thus showing both together the shift in the EOF-2 pattern. The centers of the dipoles in the DEOF pattern agree with the regions of strongest increase/decrease in variability, as seen in Fig. 3.17d, i.e. the DEOF analysis reveals how the changes in variability relate to the changes in the modes of variability.*

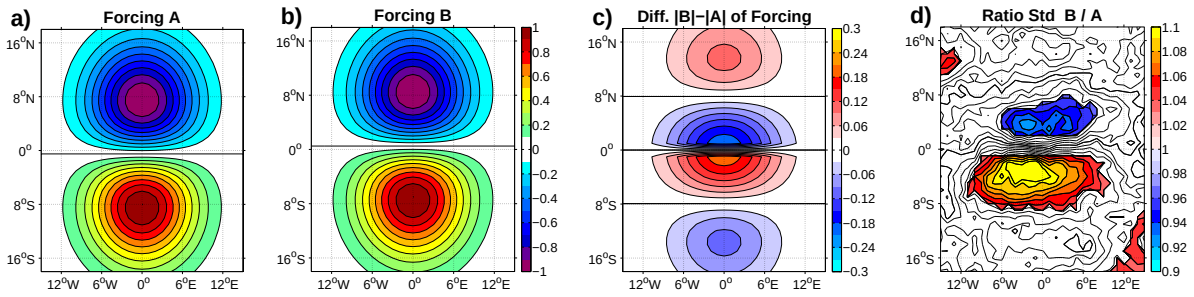

Figure 3.19: *Additional experiment for the example in Sect. 3.5.3, but with a dipole pattern shift from south (A) to north (B).* ***Part 1****: Forcing pattern and difference in variability. Same structure for the figure panels as in Fig. 3.2: (a)-(b) the forcing pattern shifts along the line between the two centers, i.e. an upward shift of 1 grid point in this case. (c)-(d) absolute difference in the forcing is a quattro-pole structure, also in the ratio of the standard deviation.*

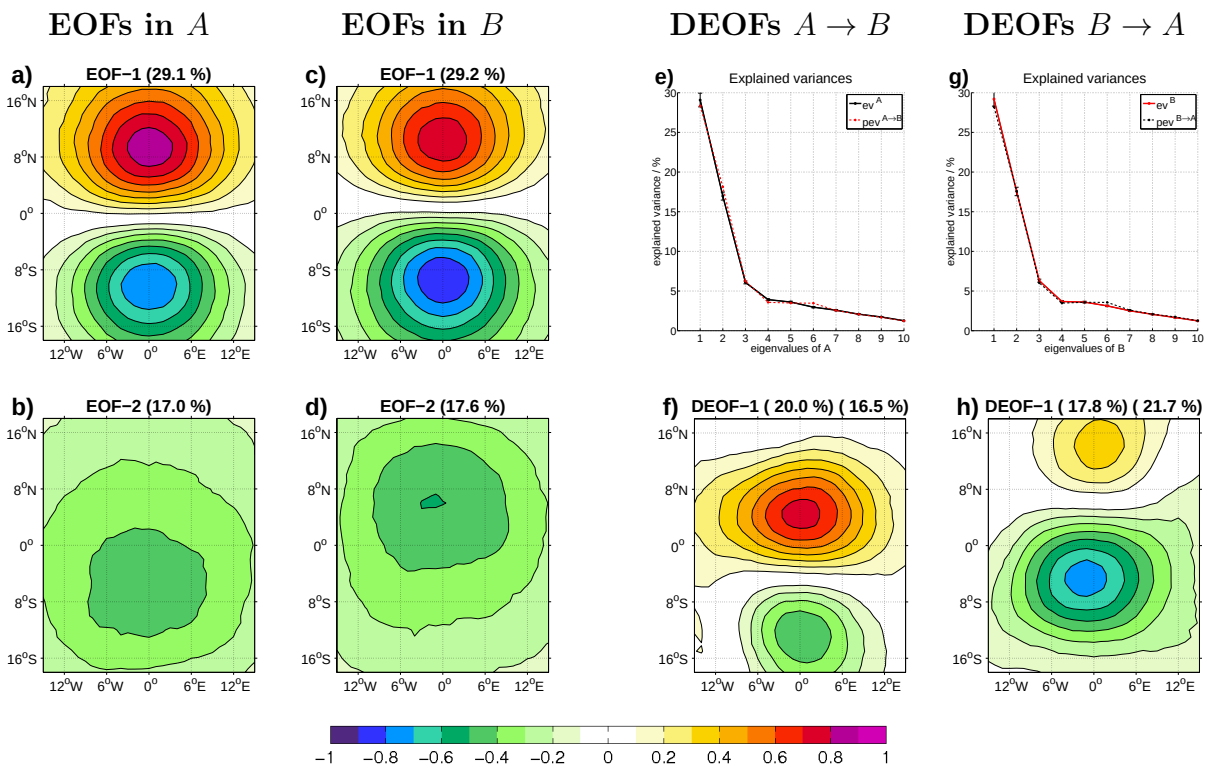

Figure 3.20: *Additional experiment for the example in Sect. 3.5.3, but with a dipole pattern shift from south (A) to north (B).* ***Part 2****: EOF and DEOF analysis. Same structure for the figure panels as in Fig. 3.3: (a)-(d) here we chose a quite strong forcing, so that the EOF-1 is a dipole and EOF-2 is a monopole. A small upward shift of the pattern can be seen, if we look closely on the EOF-1 pattern of A and B; (e), (g) the projected explained variances show no difference in explained variance of the EOF pattern, due to high pattern correlation between the EOF patterns of the two datasets (0.99 for the EOF-1 and 1.00 for the EOF-2). (f), (h) the two centers of both DEOF pattern are exactly at the points where the variability changes strongest. The two DEOF-1 patterns show together the northward shift of the two poles in the EOF-1. In comparison with the example in Fig. 3.18 we can see that the small shift of 1 grid point along the line between the two centers gives nearly the same difference in the DEOF pattern than a 6 grid point shift orthogonal to the line between the two centers.*

3.9 Supplemental Material: Matlab code for DEOF Analysis

```
function [deof,pev,dev0,dev] = deof_2sets_analysis(eof0, eof, ev0, ev, lat)
%
% evaluating EOFs of two data sets against each other to find the
% DEOF pattern that are more important in terms of explained variance
% in data set2 than in data set1. See Bayr and Dommenget (2012) for details.
%
% Input:
%
% eof0(neof,xdim,ydim): eofs of data set1 (this eofs will not be rotated)
%  eof(neof,xdim,ydim): eofs of data set2 (this eofs will be rotated)
%           (undefined values should be set to zero in both eof sets)
%                 ev0: explained variances of eof0
%                  ev: explained variances of eof
%                 lat: latitudes as vector for lat weighting sqrt(cos(lat))
%
%
% Output:
%
% deof:  DEOF pattern of the data-matrix that have a higher
%         explained variance in data set2 than in data set1
%  pev:  projection of eigenvalues of data set1 on data set2
%        (compare with ev0; eq.[1] and [2] of Bayr and Dommenget (2012))
% dev0:  exp. variances of DEOFs in data set1
%  dev:  exp. variances of DEOFs in data set2
%
% Author: Tobias Bayr (tbayr@geomar.de) based on a Dietmar Dommenget script
% date: 18.09.2012 V1.0

% parameters & initialization
[neof,xdim,ydim] = size(eof);
xydim = xdim*ydim;
deof  = zeros(neof,xdim,ydim);

% latitudes weight (apply same lat weight in eof analysis
% to ensure that pattern are orthogonal!)
wg = ones(xdim,1) * sqrt(cosd(lat))';
wgv = reshape(wg,xydim,1);

% reshape data(neof,xdim,ydim) -> xydata(xydim,neof)
eofv = reshape(eof,neof,xydim)';
eof0v = reshape(eof0,neof,xydim)';

% latitude weight data
eofv = eofv .* (wgv * ones(1,neof));
eof0v = eof0v .* (wgv * ones(1,neof));

% normalize eofs
for k=1:neof
    eofv(:,k) = eofv(:,k)./sqrt(eofv(:,k)'*eofv(:,k));
    eof0v(:,k) = eof0v(:,k)./sqrt(eof0v(:,k)'*eof0v(:,k));
end

% warning if eofs are not orthogonal
pcor1 = eofv(:,1)' * eofv(:,2);
```

```
pcor2 = eof0v(:,1)' * eof0v(:,2);
if abs(pcor1) > 1e-12 || abs(pcor2) > 1e-12
    warning('Warn:Unorthogonal',...
'EOF pattern are not orthogonal to each other. Please check lat weighting!');
end

% project null-eof on eof (eq. [1] and [2] Bayr and Dommenget 2012)
r = (eofv'*eof0v); pev = ev0*(r.*r)';

% find DEOF (rotation of eof around eof0)
[deofv, dev, dev0]=deof_rotation(eofv,ev,eof0v,ev0);

% reshape & scale fields
for n=1:neof
    deof(n,:,:)=sqrt(sum(ev0)*dev(n)/100)*reshape(deofv(:,n)./wgv,xdim,ydim);
end

return

% ========================================================================
function [reofv, rev, rev0] = deof_rotation(eofv,ev,eof0v,ev0)
% estimate maximum variance diff. by pairwise rotation
% ========================================================================
neof = length(eofv(1,:)); rev=ev; reofv=eofv;
da   = 0.05;                % step width in rotation    [fractions of pi]
amax = pi;                  % maximum angle of rotation
a=0.:da*pi:amax;
iter = 3;                   % number of interations of rotation
xdif = zeros(1,neof);

% rotation
for i0=1:neof
    for k=1:iter
        for i2=i0+1:neof
            x1=cos(a)'*reofv(:,i0)'+sin(a)'*reofv(:,i2)';
            x2=sin(a)'*reofv(:,i0)'-cos(a)'*reofv(:,i2)';
            xev1=ev*((eofv'*x1').^2);  xev2=ev*((eofv'*x2').^2);
            evbx=ev0*((eof0v'*x1').^2);
            [xd ii]=max(xev1-evbx);         % eq. [10] of (Dommenget 2007)
            reofv(:,i0)=x1(ii,:); rev(i0)=xev1(ii);
            reofv(:,i2)=x2(ii,:); rev(i2)=xev2(ii);
        end
        xdif(i0)=xd;
    end
end
rev0=rev-xdif;
return
```

Chapter 4

The Eastward Shift of the Walker Circulation in Global Warming and its relationship to ENSO variability

This chapter will be submitted as an article to Climate Dynamics.

Abstract

This article discusses the global warming response of the Walker Circulation and the other zonal circulation cells (represented by the zonal stream function) in a CMIP5 multi-model ensemble (MMEns) in the RCP4.5 scenario. The changes in the mean state are presented as well as the changes in the modes of variability.

The main changes in the mean zonal circulation are a weakening of the circulation nearly everywhere along the equator, but over the Pacific the Walker cell also shows a significant eastward shift. These changes in the mean circulation are very similar to the leading mode of interannual variability in the tropical zonal circulation cells, which is dominated by ENSO variability. During an El Nino event the circulation weakens and the rising branch over the Maritime Continent shifts to the east in comparison to neutral conditions (vice versa for a La Nina event). Two third of the global warming trend of the Walker cell can be explained by a long-term trend in this interannual variability pattern, i.e. a shift towards more El-Nino-like conditions in the MMEns in global warming.

The ENSO associated variability of the zonal stream function has a spatial non-linearity, which is characterised by El Nino anomalies being located more to the east compared to La Nina anomalies. Consistent with this non-linearity we find a shift to the east of the dominant mode of variability of zonal stream function in global warming. All these results vary among the individual models, but the MMEns of CMIP3 and CMIP5 show in nearly all aspects very similar results, which underline the robustness of these results.

The observed data (ERA Interim reanalysis) from 1979 to 2012 shows a westward shift and strengthening of the Walker Circulation, opposite of what the results in the CMIP MMEns reveal. However, 75% of the trend of the Walker Cell can again be explained by a shift of the dominant mode of variability, but here towards more La-Nina-like conditions. Thus long-term trends of the Walker cell seem to follow to a large part the pre-existing dominant mode of internal variability.

4.1 Introduction

The equatorial zonal circulation of the atmosphere originates from the zonal temperature differences along the equator due to the land-sea distribution and ocean circulation within the tropics and forms the main zonal circulation cells: the Indian Ocean cell, the Pacific Ocean or Walker cell and the Atlantic Ocean cells. The Walker cell is the most prominent one of these cells, as its variability is strongly linked to sea surface temperature (SST) variations of the El Nino phenomena. Mean state and variability of these zonal circulation cells have large socio-economical impacts via modulating the distribution of precipitation. It is therefore of great interest, how the zonal circulation cells will respond in mean state and variability in a warmer climate, and whether they are already changing today.

Most recent studies focus on the Walker Circulation and predict that it weakens under global warming (e.g. *Knutson and Manabe*, 1995; *Vecchi and Soden*, 2007; *DiNezio et al.*, 2009). This picture has not changed in the climate model runs of the 5th Phase of the Coupled Model Intercomparison Project (CMIP), that were carried out for the 5th Assessment Report (AR5) of the Intergovernmental Panel on Climate Change (IPCC): Figure 4.1 shows the trend of the sea level pressure (SLP) and SST gradient over the equatorial Pacific of the individual CMIP3 models under the A1B scenario and of the individual CMIP5 models under the RCP4.5 scenario. The multi-model ensemble (MMEns) and most models show a consistent reduction of both SST and SLP gradients, i.e. a weakening of the Walker Circulation. The CMIP5 MMEns shows a stronger weakening than the CMIP3 MMEns, despite a weaker greenhouse gas increase in the CMIP5 RCP4.5 scenario than in the CMIP3 A1B scenario. But in both CMIP3 and CMIP5 there are models that show no significant trend or even a strengthening of the Walker Circulation. Thus a spread in the signal can be found in the individual models.

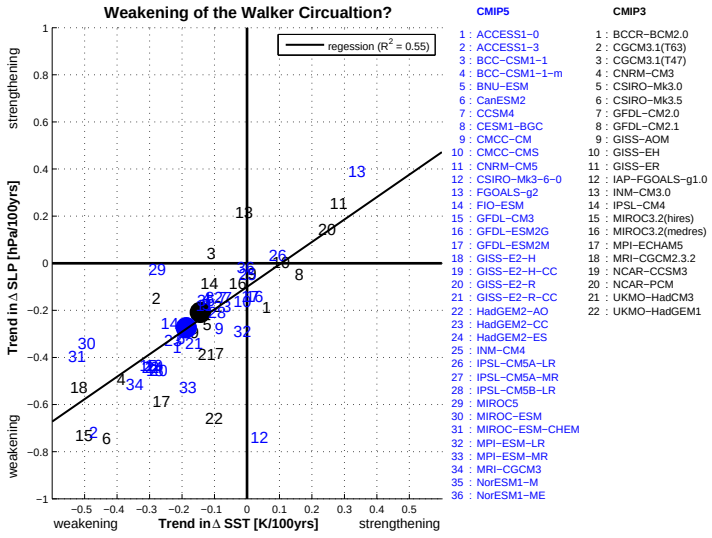

Figure 4.1: *Trend of the Δbox index difference (W−E) of SST and (E−W) of SLP in the individual models of the CMIP3 and CMIP5 data base, with box E = (80-160°W,5°S-5°N) and box W = (80-160°E, 5°S-5°N) over the period 1950-2099; The black and blue circles are the MMEns values.*

Knutson and Manabe (1995) indicate two different mechanisms, which determine the response of the Walker Circulation in a warmer climate. The first mechanism works with a

horizontal homogeneous warming, that increases with height, and is a pure atmospheric one. In a warmer climate an enhanced hydrological cycle leads to enhanced upper level warming, which increases the static stability. This mechanism was further investigated in *Held and Soden* (2006) and *Vecchi and Soden* (2007) and it acts to weaken the tropical circulations in a warmer climate. This pure atmospheric mechanism can only weaken the Walker Circulation in a warmer climate and strengthens it in a colder climate as found in a paleo-climate study (*DiNezio et al.*, 2011). In the following we will refer to this mechanism as the homogeneous warming, as it does not require any horizontal gradients in the warming pattern.

The second mechanism works with horizontal inhomogeneous temperature changes, i.e. the change in zonal temperature gradients. These depend on the local differences in the strength of evaporative cooling (*Knutson and Manabe*, 1995), the ocean dynamical thermostat cooling (*Clement et al.*, 1996), cloud cover feedbacks (*DiNezio et al.*, 2009) and the land-sea warming contrast (*Bayr and Dommenget*, 2013a). Further *DiNezio et al.* (2009) found that in a CMIP3 MMEns the evaporative cooling and cloud cover feedbacks reduce the warming over the warm pool region stronger than the ocean dynamical thermostat cooling over the cold tongue region, hence reduce the SST gradient over the Pacific and weakens the Walker Circulation. This second mechanism can in general act in both directions in a warmer climate: it can increase or decrease the zonal circulation. In the following we will refer to this mechanism as the inhomogeneous warming, as it requires changes in the horizontal temperature gradients.

The studies of *Vecchi and Soden* (2007) and *Yu et al.* (2012) mention another interesting aspect about the Walker Circulation response, which can have a large impact on the distribution of precipitation: The Walker Circulation is not only expected to weaken, it also shifts eastward in global warming. Both studies relate this eastward shift to a trend towards more El-Nino-like conditions and also the studies of *Chung et al.* (2013) and *Bayr and Dommenget* (2013b) give some hints that this eastward shift can be related to El Nino Southern Oscillation (ENSO).

ENSO is a coupled air-sea interaction phenomena with associated changes in SST gradient, SLP gradient and surface winds over the Pacific (*Philander*, 1990): El Nino is characterised by anomalous warm SST over the East and Central Pacific, weaker surface winds over the West Pacific, a weaker SLP gradient over the Pacific and more convection over the Eastern Pacific. For La Nina the situation is vice versa, with more convection over the West Pacific, thus ENSO variability is associated with a longitudinal shift of convection. Another important feature of ENSO variability is its spatial non-linearity (e.g. *Hoerling et al.*, 1997; *Rodgers et al.*, 2004; *Yu and Kim*, 2011; *Dommenget et al.*, 2013), i.e. that the warming of SST during El Nino events occurs a bit further to the east than the SST cooling during La Nina events. The aim of this study is to have a closer look on the eastward shift of the Walker Circulation in global warming and its relationship to ENSO variability. Further, we want to analyse the changes in the modes of variability and find out if the trend of the zonal circulation cells follow a pre-existing mode of internal variability.

In our analyses we use the zonal stream function for the representation of the zonal circulation cells and the Walker Circulation, as defined in *Yu and Zwiers* (2010) and *Yu et al.* (2012). This is a direct measure of the circulation and not like the SLP an indirect approximation of the circulation. It has the advantage that it measures the zonal circulation over all levels, and thus includes both areas where the two mechanisms mentioned above influence the zonal circulation. We address the following questions: 1) What is the response of the zonal circulation cells to global warming in the mean state and how do its modes of variability change in the CMIP3

and CMIP5 database in global warming? 2) Does the Walker Circulation shift eastward and if yes, what causes the eastward shift in global warming? 3) Can the predicted response already be found in reanalysis data of the last decades? The paper is organised as follows: Section 4.2 gives an overview of the data and the definition of the zonal stream function used in this study. The response in the mean state in the CMIP MMEns is shown in section 4.3, followed by an analysis of the eastward shift in section 4.4. The non-linearity of the Walker Circulation in ENSO variability is investigated in section 4.5 and the changes in the modes of variability in section 4.6. The observed trends in the recent decades in reanalysis data are shown in section 4.7. In the final analysis section we discuss how changes in SLP relate to changes in the zonal circulation cells and conclude our analysis with a summary and discussion in section 4.9.

4.2 Data and Methods

The data analysed in this study are taken from the Climate Model Intercomparison Project Phase 3 and 5 (CMIP3, *Meehl et al.*, 2007a and CMIP5, *Taylor et al.*, 2012). From CMIP3 we use data from the 20C and A1B scenarios, from CMIP5 we use the historical and RCP4.5 scenarios. The RCP4.5 scenario has a bit weaker increase in greenhouse gases than the A1B scenario. We choose these greenhouse gas emission scenarios because most of the available models simulated these scenarios. We have the following variables available from 22 CMIP3 models and 36 CMIP5 models: sea level pressure (SLP), sea surface temperature (SST), atmospheric temperature (T), tropospheric temperature (T_{tropos}; mass weighted average of atmospheric temperature between 1000 and 100hPa), zonal wind (U), meridional wind (V) and vertical wind (W); see Figure 4.1 for a list of climate models. Each data set is interpolated onto a regular 2.5° x 2.5° grid and for each CMIP phase, CMIP3 and CMIP5, we make a multi-model ensemble (MMEns) with one ensemble member from each model. For the mean trend analysis we calculate the multi-model mean trends and for the analysis of the change in variability we concatenate all data sets to get one long data set, where anomalies are defined for each model individually first.

For comparison with observations and analysing the trends of the recent decades we use ERA Interim reanalysis data (*Simmons et al.*, 2007) for the period 1979 until 2012 in lack of "real" observations of tropospheric winds. We choose ERA Interim because the tropical tropospheric temperature trends in this data set are in a good agreement with satellite observations (*Bengtsson and Hodges*, 2009). These data sets are also interpolated onto a regular 2.5°x2.5° grid.

As a measure for the zonal circulation along the equator we use the zonal stream function as defined in *Yu and Zwiers* (2010) and *Yu et al.* (2012):

$$\Psi = 2\pi a \int_0^p u_D \frac{dp}{g} \tag{4.1}$$

with the divergent component of the zonal wind u_D, the radius of the earth a, the pressure p and gravity constant g. The zonal wind is averaged for the meridional band between 5°N and 5°S and integrated from the top of the atmosphere to surface, but in the figures only the levels below 100hPa are shown, as above that level the stream function is nearly zero.

4.3 Mean state and response

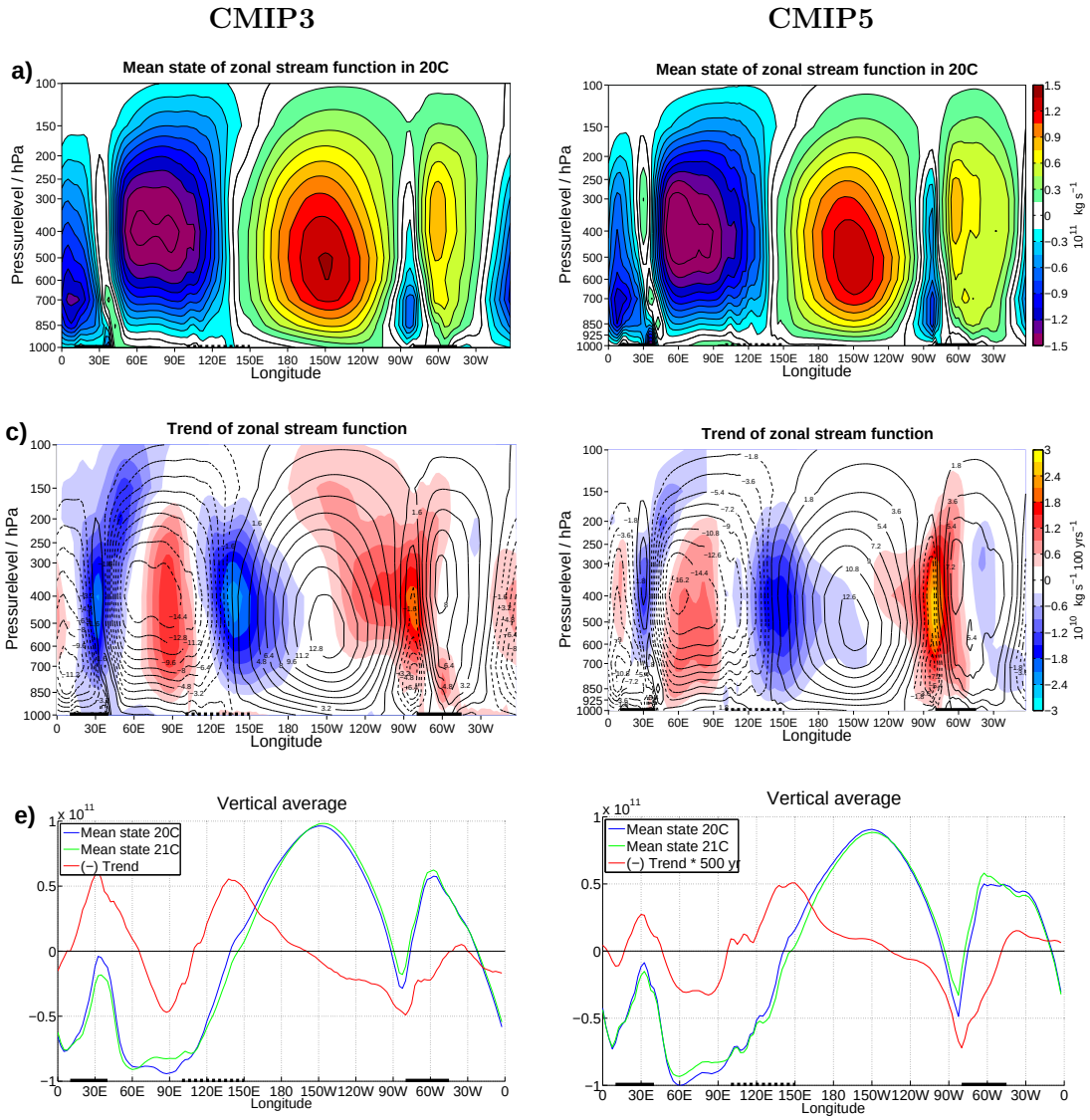

Figure 4.2: *(a) Mean state of zonal stream function along the equator in CMIP3 MMEns over the period from 1950 to 1979 (20C), averaged from 5°S to 5°N; black bold lines at the bottom indicate the three continents Africa, Maritime Continent and South America, (b) same as (a) but here for CMIP5 MMEns, (c) shading: linear trend of zonal stream function in CMIP3 MMEns in the period 1950 to 2099, contours: mean state from (a), (d) same as (c) but here for CMIP5 MMEns, (e) vertical average of (a) in kg s^{-1} (blue line), (c) in kg s^{-1} $(500yr)^{-1}$ (red line) and mean state over the period from 2070 to 2099 (21C) in kg s^{-1} (green line), (f) vertical average of (b) in kg s^{-1} (blue line) and (d) in kg s^{-1} $(500yr)^{-1}$ (red line) and mean state in 21C in kg s^{-1} (green line).*

The mean state of the zonal stream function in the CMIP3 and CMIP5 MMEns for the period 1950 until 1979 agree quite good with each other (see Fig. 4.2a,b) and with reanalysis data (not shown), as already investigated in more detail in *Yu et al.* (2012) for a CMIP3 MMEns. Positive values indicate a clockwise circulation and negative an anticlockwise circulation. The

three main convection regions (Africa, the Maritime Continent and South America) and the descending regions (West Indian Ocean, the Pacific cold tongue region and the Atlantic Ocean) form together the main circulation cells (the Indian Ocean cell, the Pacific or Walker cell and the Atlantic Ocean cells). The trend patterns in global warming over the period 1950 until 2099 are very similar in the CMIP3 and CMIP5 MMEns (Fig. 4.2c,d) and to the results of *Yu et al.* (2012). Thus, the trend pattern seems to be very robust despite different models, resolutions, ensemble sizes and emission scenarios in the MMEns. The MMEns predict more ascending over the West Indian Ocean and the Pacific and more descending over Africa, the Maritime Continent and South America in global warming (see also Fig. 4.3). We can build the vertical averages of the stream functions to get a clearer picture: The global warming trend of the tropical zonal circulations over most of the Indian and Atlantic oceans is opposite to the mean state (Fig. 4.2e,f, note the reversed sign of the trend for better comparison), which indicates a weakening of the circulation in agreement with the arguments of *Vecchi and Soden* (2007). If we focus on the Pacific ocean, the MMEns predict only a small change in strength of the circulation (at the maximum of the Walker cell at 150°W): in the CMIP3 MMEns it slightly increases, in agreement with the results from *Yu et al.* (2012), in the CMIP5 MMEns it slightly decreases. But in these figures the striking difference between the mean states in 20C and 21C over the Pacific is the eastward shift of the Walker cell (compare the blue and green curves in Fig. 4.2e,f). This can also be seen in the vertical wind at the 500hPa level along the equator (Fig. 4.3): Over the East Indic and Maritime Continent the vertical wind decreases, but increases over the Pacific Ocean. Thus an eastward shift of the Walker Circulation can be seen in zonal stream function as well as in the vertical wind.

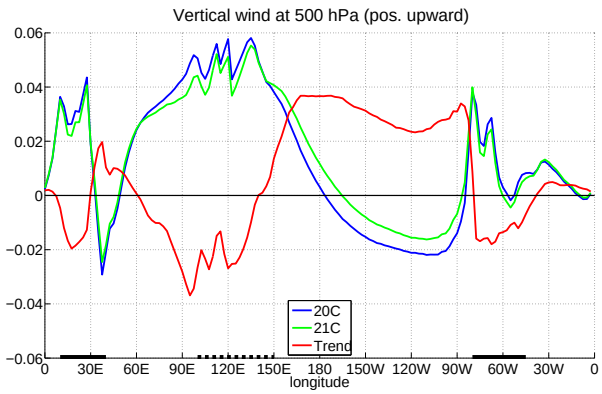

Figure 4.3: *Mean state of the vertical wind (positive upward) at 500 hPa, 5°S-5°N in 20C (blue line), 21C (green line) in Pa s^{-1} and trend over the period 1950 to 2099 in Pa s^{-1} $(500yr)^{-1}$ (red line) in CMIP5 MMEns.*

We can quantify the shift in the circulation cells by the zero line of the stream function over the Maritime Continent warm pool region, which determines the western edge of the Walker cell and coincides approximately with the maximum of convection in Fig. 4.3. Figure 4.4 shows the shift in the position of the western edge of the Walker cell in global warming on the x-axis and the average trend in the box over the ascending branch of the Walker and Indic cell on the y-axis (120°E-180°, 700-300hPa) for each individual CMIP3 and CMIP5 model. Most models show a negative trend and an eastward shift under global warming, which appear to have a weak linear relation: models that tend to have a stronger negative trend also tend to have a stronger eastward shift.

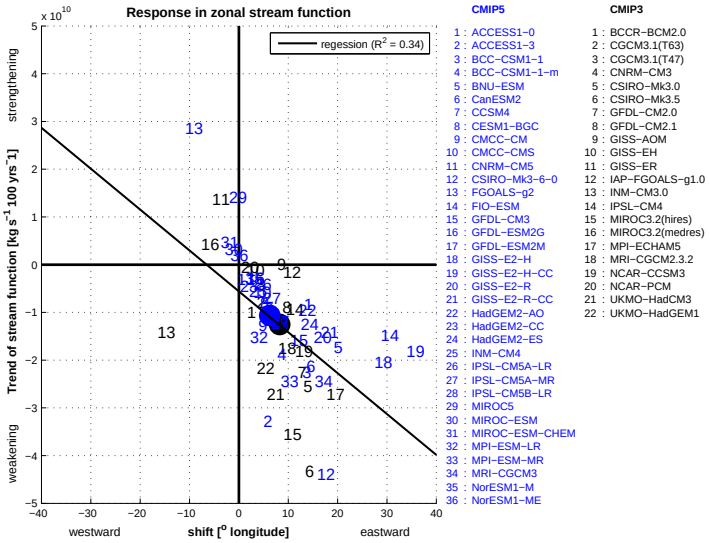

Figure 4.4: *Response of zonal stream function in global warming in the individual models of the CMIP3 and CMIP5 data base, on the x-axis the shift of the western edge (zero line of stream function) of Walker cell, on the y-axis the trend of zonal stream function averaged over the box 120°E-180°, 700-300hPa.*

4.4 East-west shift of the Walker Circulation during El Nino/La Nina

From interannual variability it is known that the large scale convection and precipitation shift in the east-west direction during El Nino/La Nina events (e.g. *Philander*, 1990). Whether the east-west shift of the convection during El Nino is associated with an east-west shift in the zonal circulation cells can be analysed by composites of the stream function for El Nino and La Nina events. As selection criteria for these composites we use the normalised Nino3.4 index (normalised with its standard deviation) from detrended SST anomalies. These composites contain all months with normalised Nino3.4 index $>$ 1 for El Nino and normalised Nino3.4 index $<$ -1 for La Nina.

The Walker Circulation in ERA Interim reanalysis data reveals indeed an east-west shift in ENSO variability (Fig. 4.5a,b): The zonal circulation cells over the Indo-Pacific are considerably weaker during El Nino than during La Nina. Additionally, we can see that the western edge of the Walker Circulation is shifted more to the east (176°E) during El Nino and more to west (140°E) during La Nina, in comparison to the mean state (151°E). Figure 4.5c shows the difference between the El Nino and La Nina composites. An interesting point is that ENSO affects not only the Pacific cell, but also has a significant impact on the circulation cell over the Indian Ocean.

Figures 4.5d-f show the same composites as in Fig. 4.5a-c but for the CMIP5 MMEns over the period 1950-1979. The Nino3.4 index is again selection criterion, normalised in each model with its standard deviation of Nino3.4 index to account for the inter-model-differences in variability strength. During La Nina the eastern edge of the Walker cell is at 133°E, in the mean state it is at 141°E and during El Nino at 165°E, so with in total 32° a very similar

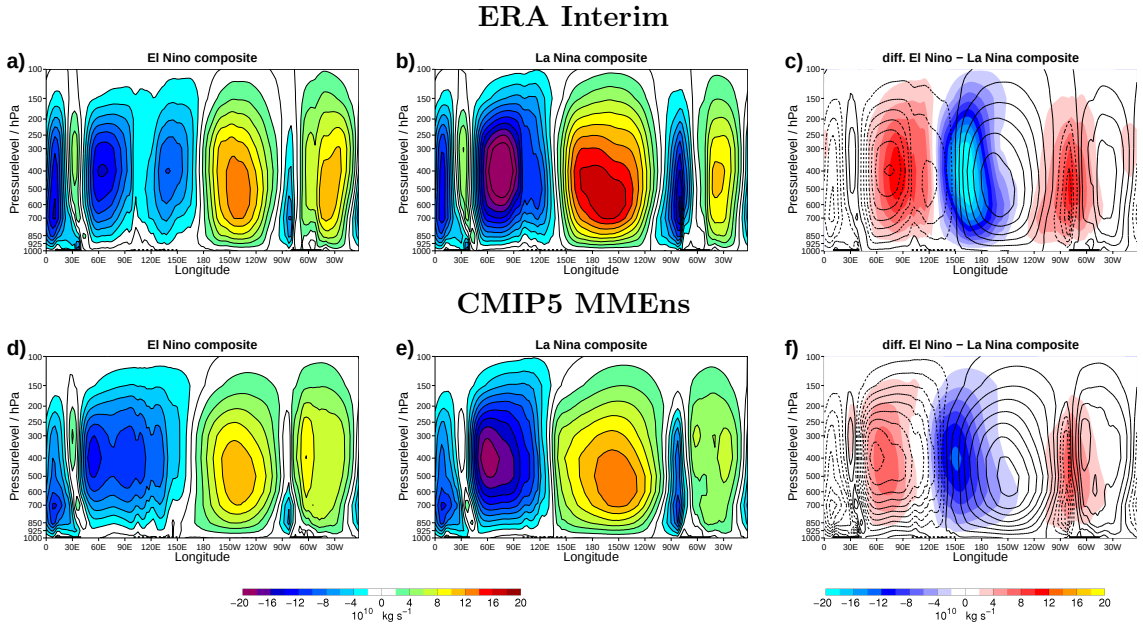

Figure 4.5: *Composites of zonal stream function (a-c) in ERA Interim, with normalised Nino3.4 index (170°W-120°W, 5°S-5°N) as selection creterion, (a) for Nino3.4 > 1 (El Nino), (b) for Nino3.4 < −1 (La Nina), (c) shading: difference El Nino − La Nina (i.e. ENSO amplitude), contours: mean state in ERA Interim; (d-f) same as (a-c) but here for CMIP5 MMEns in 20C.*

east-west shift as in reanalysis data, but all three states located roughly 10° further west than in reanalysis. The amplitude of the ENSO variability (Fig. 4.5f) over the West Pacific is 30% lower und also 10° further west than in the reanalysis data. It is interesting to note that the trend pattern from Fig. 4.2c,d has some similarities to the ENSO amplitude pattern in Fig. 4.5f with a pattern correlation of 0.61 in CMIP3 and 0.73 in CMIP5. This is a hint that large parts of the trend in global warming are linked to more El-Nino-like conditions, as already seen in the trend of the box index of SST in Fig. 4.1. However, there is no linear relation between the eastward shift during El Nino and the eastward shift in global warming in the individual models, i.e. that the models with a stronger eastward shift in ENSO variability do not show a stronger eastward shift in global warming (not shown).

From the similarity of the Walker cell response to ENSO and to global warming the question arises if they have the same mechanism. Figure 4.6a shows the vertical profile of the ENSO pattern (El Nino minus La Nina composite as in Fig. 4.5f) in the CMP5 MMEns of atmospheric temperature along the equator. The strongest warming appears over the Pacific with a maximum at the surface and at 300hPa. According to the two mechanisms mentioned in the introduction, we split up this pattern in a horizontal homogeneous and inhomogeneous part. A homogeneous warming, that increases with height, acts to weaken the tropical circulations and an inhomogeneous warming may cause more ascending where it is relative warm and more descending where it is relative cold.

First of all we can note that ENSO is also associated with a homogeneous warming that increases with height (Fig. 4.6b). In Fig. 4.6c we can see that the response of the zonal stream function in ENSO variability (contours) fits quite well to the inhomogeneous warming (shading), as we get additional ascending where the atmosphere warms stronger and additional descending

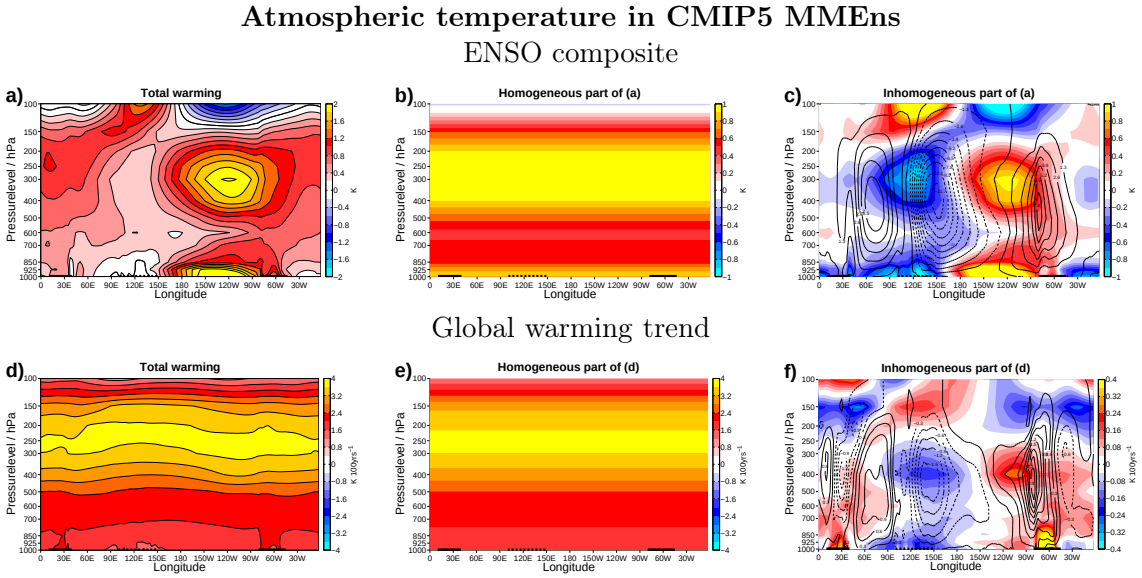

Figure 4.6: *(a) Same as Fig. 4.5f, but here for atmospheric temperature in the CMIP5 MMEns (i.e. the atmospheric warming in an El Nino − La Nina composite), (b) horizontal homogeneous warming (zonal mean of (a)), (c) shading: horizontal inhomogeneous warming ((a) - (b)), contours: ENSO amplitude from Fig. 4.5f; (d) linear trend of atmospheric temperature over the period from 1950 till 2099 in the CMIP5 MMEns, (e)-(f) same as (b)-(c), but here for (d), but in (f) the trend pattern of Fig. 4.2d as contours.*

where it warms less. In ENSO the homogeneous part is of the same order as the inhomogeneous (Fig. 4.6b,c).

In global warming (Fig. 4.6d-f) the homogeneous and inhomogeneous warming have a similar structure as in the ENSO composite: both show the strongest warming near the 300hPa level in the homogeneous warming and a stronger warming over the East and Central Pacific than over the East Indic and Maritime Continent in the levels below 200hPa and vice versa above. But in global warming the homogeneous warming is roughly 10 times larger than the inhomogeneous warming. Here fits the response of zonal stream function (contours in Fig. 4.6f) only roughly to the inhomogeneous warming (shading in Fig. 4.6f), strongest disagreeing over the Maritime Continent.

4.5 Non-linearity of the Walker Circulation in ENSO variability

Next we want to investigate, if the Walker Circulation exhibits a spatial non-linearity in ENSO variability as one can find in SST. We repeat the composite analysis from above but now with detrended anomalies instead of the full field values of the zonal stream function and normalised with the mean Nino3.4 index of these composites to account for the skewness of SST (Fig. 4.7). In reanalysis data we get abnormal ascending over the West Indic and Central Pacific und abnormal descending over most of the Maritime Continent region (between 60°E and 160°E) during El Nino (Fig. 4.7a) and vice versa during La Nina (Fig. 4.7b, note the reversed sign), but with the anomalies shifted more to the west and having a weaker amplitude. This east-west

difference in location and difference in strength are a non-linearity. The amplitude in Figure 4.7c shows the region where the Walker Circulation in ENSO variability is non-linear, as in a linear case the sum of El Nino and La Nina composite would be zero due to the normalisation by the mean Nino3.4 index. The zonal circulation cells anomalies over most of the Indo-Pacific region are non-linear, with a maximum between 110°E to 140°W.

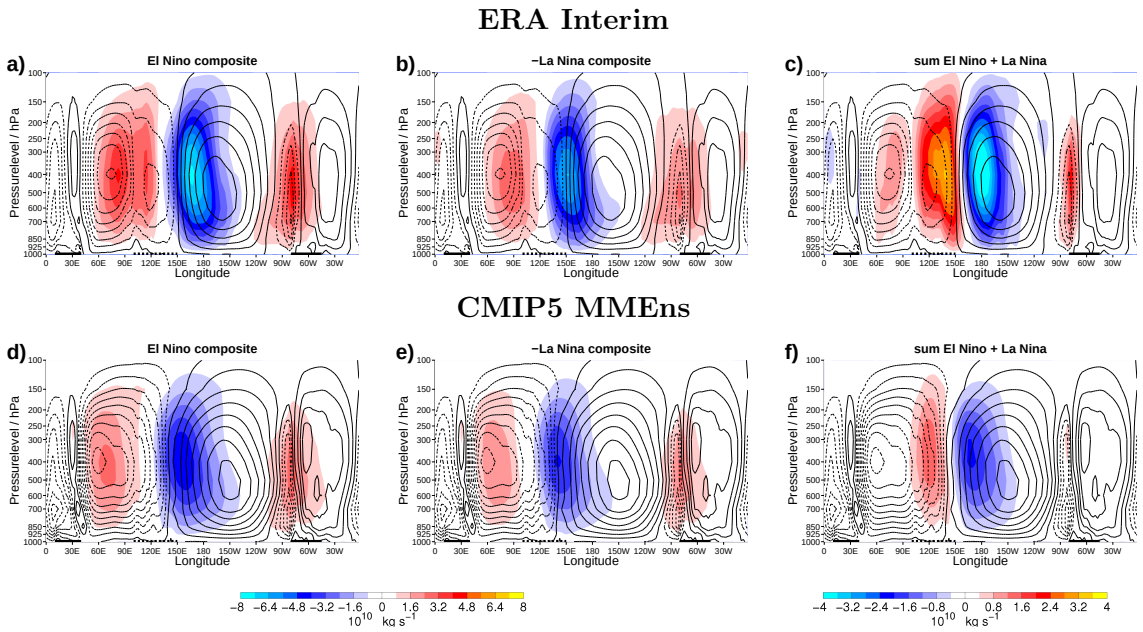

Figure 4.7: *Same as Fig. 4.5, but here composites of detrended anomalies, normalised with mean Nino3.4 index (170°W-120°W, 5°S-5°N), shading: (a) for Nino3.4 > 1 (El Nino), (b) for Nino3.4 < -1 (La Nina), (c) sum El Nino + La Nina (i.e. a measure for the non-linearity); contours in figures (a-c): mean state in ERA Interim; (d-f) sames as (a-c) but here for CMIP5 MMEns in 20C.*

The composites of the CMIP5 MMEns over the period 1950-1979 (Fig. 4.7d-f) are very similar to the composites of reanalysis data (Fig. 4.7a-c), also with La Nina amplitude more in the west and weaker than El Nino amplitude over the West Pacific. The ENSO non-linearity is, however, confined to a smaller region (110°E to 140°W; see Fig. 4.7f) and has weaker amplitude than in reanalysis data. In order to quantify how well the MMEns and the individual climate models simulate the spatial non-linearity of the Walker Circulation, we define a simple two box index: The west-east difference between a western box (120°E-150°E, 200 hPa-700 hPa) and eastern box (170°E-160°W, 200 hPa-700 hPa) in the difference plot of the composites as shown for reanalysis data in Fig. 4.7c. We can compare this with a measure for the spatial non-linearity of ENSO in SST, as defined in *Dommenget et al.* (2013): As for stream function we calculate for SST the east-west difference between an eastern box (80°W-140°W, 5°S-5°N) and western box (140°E-160°W, 5°S-5°N) of the sum of normalised El Nino and La Nina composites. Figure 8 shows these two measures for ERA Interim reanalysis data (1979-2012) and all climate models of the CMIP3 and CMIP5 data base for the period 1900 to 1999. The MMEns of CMIP3 and CMIP5 both have a much weaker non-linearity than ERA Interim, but CMIP5 is closer to the observed than CMIP3. From the individual models we can see two interesting features: First, most of the models have problems to simulate a realistic non-linearity (cluster of models around zero). Second, from the strong linear relationship we can see that the skill

to simulate a strong non-linearity in SST seems to be related to the skill in simulating a strong non-linearity in the zonal stream function. We cannot say from this analysis if the non-linearity of the SST is caused by the non-linearity of the atmosphere or vice versa. But in a recent study *Frauen and Dommenget* (2010) found out that non-linear atmospheric feedbacks in ENSO variability can exist with a linear ocean, thus that the atmosphere plays a substantial role in ENSO non-linearity.

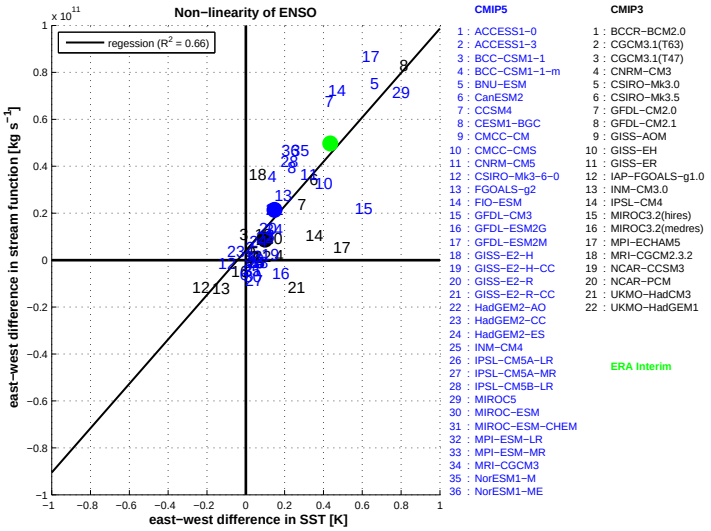

Figure 4.8: *Non-linearity of ENSO in the individual models of CMIP3 and CMIP5 data base and ERA Interm, on the x-axis a measure of the non-linearity of the SST: the difference of eastern box (80°W-140°W, 5°S-5°N) and western box (140°E-160°W, 5°S-5°N) of the sum of El Nino and La Nina composites (as defined in Dommenget et al., 2013); on the y-axis a measure of the non-linearity of the zonal stream function: the difference of western box (120E-150E, 700-200hPa) and eastern box (170°E-160°W, 700-200hPa) of the sum of El Nino and La Nina composites, like in Fig. 4.7c.*

4.6 Changes in the modes of variability in global warming

We now analyse the changes in the modes of variability under global warming. We will base this analysis on Empirical Orthogonal Function (EOF), which is a common way to determine the modes of variability. We will focus on two aspects: Do the EOF–modes change and thus indicate changes in the spatial patterns of variability? Second, do the principal component (PC) time series of the leading modes have a long-term trend under global warming, indicating that the trend-pattern may be related to leading modes of internal variability?

For the first aspect we have a closer look at the EOF patterns in the MMEns in the two time periods 1950-1979 (20C) and 2070-2099 (21C). The EOF-1 patterns (Fig. 4.9a,b) are both very similar to the composite of El Nino and La Nina (Fig. 4.7d,e) and to the combined EOF-1 of zonal stream function and SST, where the SST pattern is the typical ENSO pattern (not shown). Thus the EOF-1 is associated with ENSO variability in zonal stream function and describes an east-west shift of the edge between the Indic and Pacific cell. The western Pacific pole of EOF-1 is more in the east in 21C and this pole becomes a bit weaker than in 20C. EOF-2 describes a strengthening or weakening of the eastern part of Indic cell and the western

part of the Pacific cell and also shifts a little bit to the east in 21C.

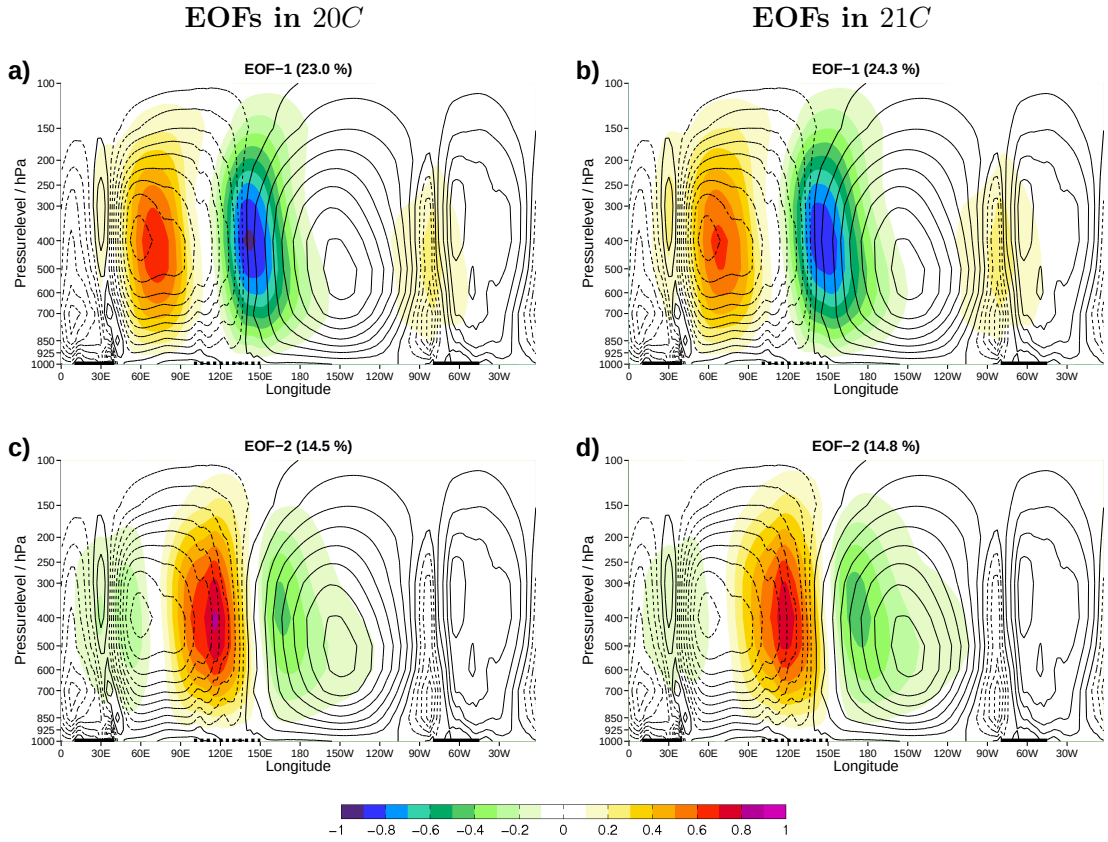

Figure 4.9: *EOFs of zonal stream function in CMIP5 MMEns, shading: (a) EOF-1 in 20C, (b) EOF-1 in 21C, (c) EOF-2 in 20C, (d) EOF-2 in 21C, explained variance is given in the header in brackets respectively; contours in all figures: mean state 20C from Fig. 4.2b.*

For a more detailed analysis of the spatial changes we can use Distinct Empirical Orthogonal Function (DEOF) analysis as described in *Bayr and Dommenget* (2013b). This method compares all the leading modes of variability in two data sets on basis of the multi-variate EOF patterns and finds the patterns of the largest changes in variability. In DEOF analysis the two EOF sets from 20C and 21C are compared against each other via projecting one set of EOF patterns onto the other to find the pattern that has the largest difference in explained variance in these two sets of EOF pattern (see *Bayr and Dommenget* (2013b) for further details). The projected explained variances (Fig. 4.10a,b) show both that the variability becomes more large scale in global warming as the leading modes of variability have a lower explained variance in 20C than in 21C, so that one needs less modes in 21C to explain the largest part of the variance. The spatial degrees of freedom from *Bretherton et al.* (1999) decrease from 10.2 in 20C to 9.5 in 20C. Additionally, EOF-1 has the largest difference in terms of explained variance in the two data sets.

The DEOF-$1^{20C \to 21C}$ (Fig. 4.10c) maximizes the explained variance differences between 20C and 21C. It is the pattern that loses the largest amount of variance in 21C relative to 20C. It mainly shows that the variance in the Indian Ocean cell is reduced by 14% in 21C relative to its 20C value (a change in explained variance from 11.1% to 9.5%). The DEOF-

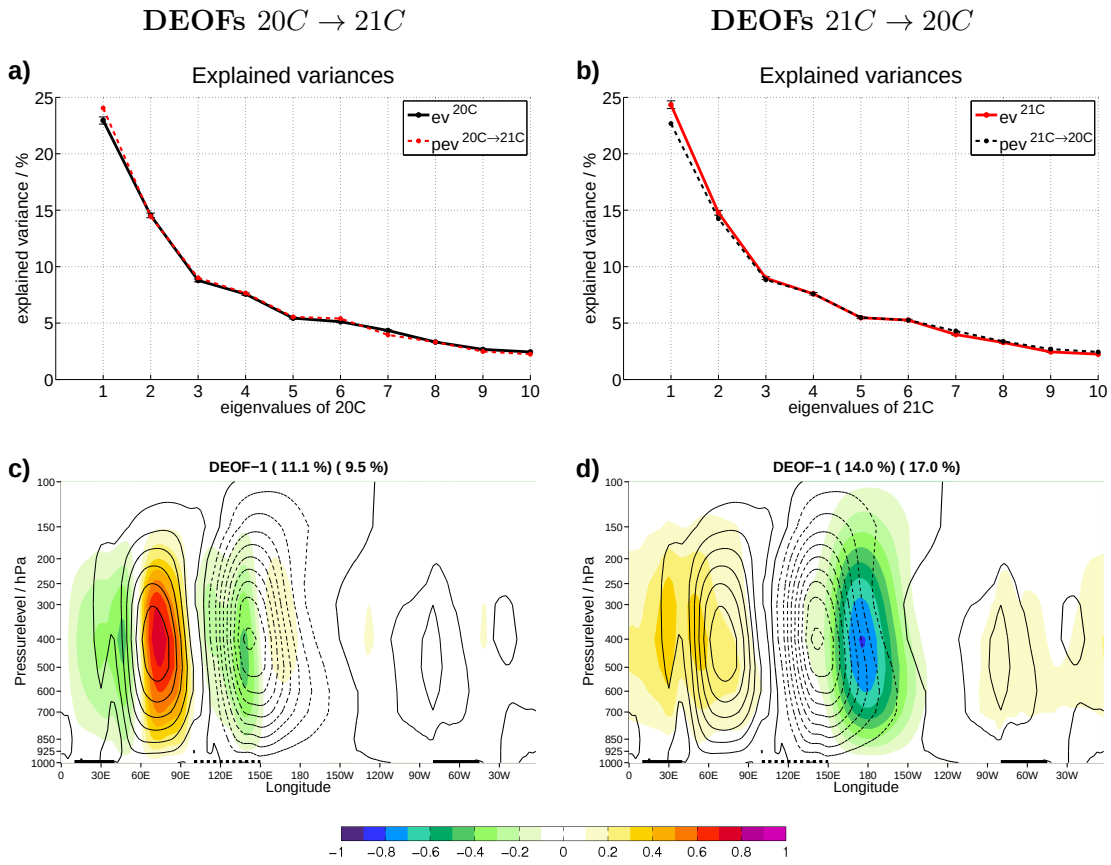

Figure 4.10: *(a) Explained variances of the eigenvalues in 20C (black solid line) and explained variances of 20C projected onto the eigenvalues of 21C (red dashed line), the error bars show the statistical uncertainties of the explained variances due to sampling errors according to North et al. (1982); (b) same as (a), but here for the eigenvalues of 21C (red solid line) and the explained variances of 21C projected onto the eigenvalues of 20C (black dashed line), (c) DEOF 20C → 21C pattern; the values given in the header in brackets is the explained variance of this pattern in 20C and 21C respectively, (d) as (c), but here DEOF 21C → 20C pattern; contours in (c)-(d): EOF-1 in 20C from Fig. 4.9a.*

$1^{21C \to 20C}$ (Fig. 4.10d) maximizes the explained variance differences between 21C and 20C. It is the pattern that gains the largest amount of variance in 21C relative to 20C. It mainly shows that the variance in the central Pacific pole has increased by 21% in 21C relative to its 20C value (a change in explained variance from 14.0% to 17.0%). Combined the two leading DEOF-modes show a shift of the variability from the Indian into the central Pacific in EOF-1. Further we can note that the DEOF-$1^{20C \to 21C}$ is of smaller spatial scale (e.g. distance between the main poles) than DEOF-$1^{21C \to 20C}$. This again suggests that the variability in 21C tends towards larger scales.

This shift from the Indian into the Pacific Ocean is consistent with the spatial non-linearity seen in the section before. The El Nino composite pattern in zonal stream function is more in the east than the La Nina composite pattern, thus an eastward shift of the dominant mode of variability can be linked to a shift towards more El-Nino-like conditions.

Next we have a look at the long-term trend in the PC time series for the period from 1950

to 2099. The similarity of the trend pattern in Fig. 4.2d with EOF-1 from Fig. 4.9a,b is already a strong hint that the zonal circulation shifts in its dominant mode of variability towards more El-Nino-like conditions. Indeed a positive trend in PC-1 (El-Nino-like) can be seen in the CMIP5 MMEns (red line in Fig. 4.11). But the decadal (natural) variability of the individual models is still much larger than the trend in the MMEns, indicating that detection of a Walker Circulation trend due to increased greenhouse gases will be very difficult in the next decades, if we are not able to separate the climate change signal from internal variability. No other PC time series exhibit a strong trend in the MMEns.

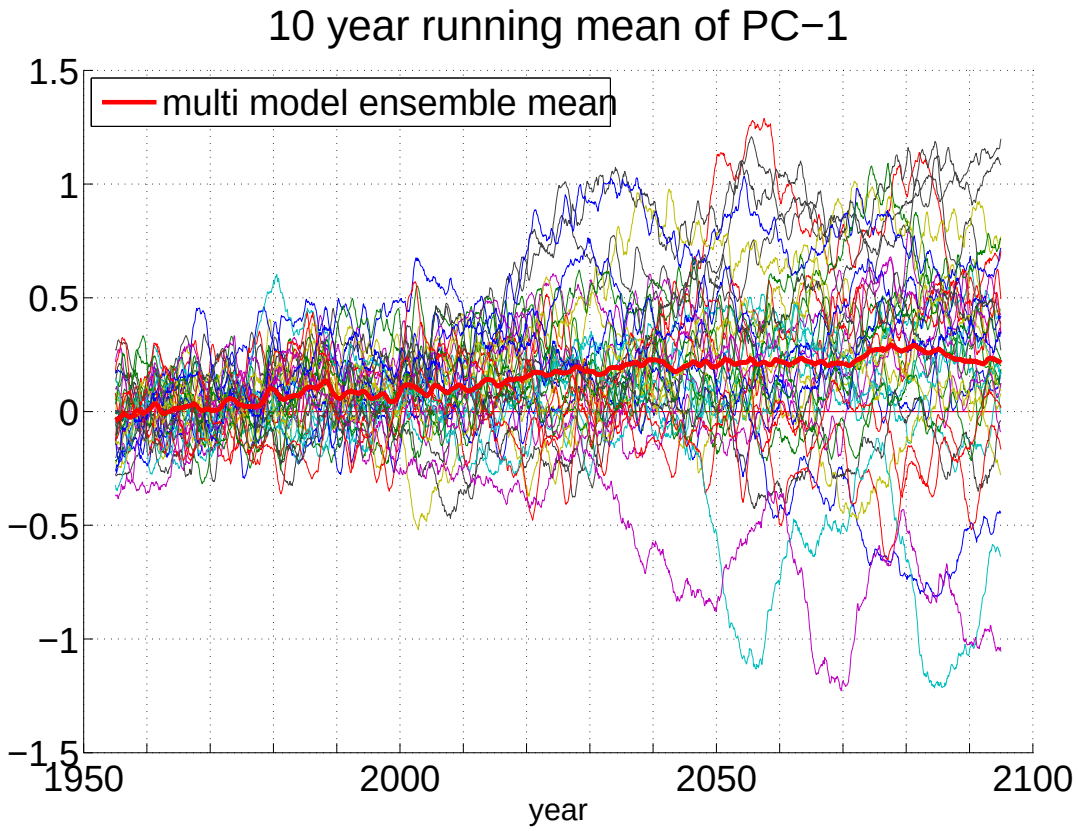

Figure 4.11: *10 year running mean of PC-1 of zonal stream function in all individual CMIP5 models; the thick red line is the average of all 36 individual models.*

Finally we want to find out how much of the global warming trend from Fig. 4.2c,d is related to the trend in the dominant mode of variability, thus the ENSO associated variability of EOF-1. In each individual model we can remove the variability and trend associated with the EOF-1 pattern. After removing EOF-1 in each model individually we can calculate a new MMEns and the residual trend of this new MMEns (Fig. 4.12). Much of the trend has vanished over the Indo-Pacific region and the trend in PC-1 can explain 52% of the trend in CMIP5 over the entire tropics or 69% of the Walker circulation changes (49% and 67% in CMIP3, respectively). The residual trend pattern shows a reduction of convection over Africa and South America, consistent with the general weakening as found in *Vecchi and Soden* (2007), less descending over the cold tongue region, consistent with the strong warming there, and an upward expansion the Indic and Pacific cell.

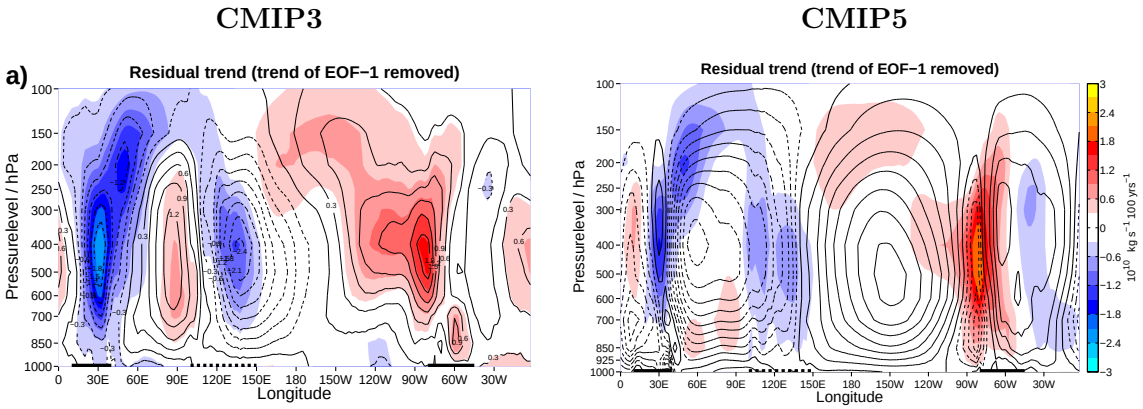

Figure 4.12: *(a) Shading: residual trend in zonal stream function in CMIP3 MMEns after removing the trend of EOF-1 in each model individually, contours: trend in stream function from Fig. 4.2c (before removing the trend of EOF-1) for comparison, (b) same as (a) but here for CMIP5 MMEns.*

4.7 Recent trends in ERA Interim reanalysis data

Next we have a look on the observed zonal circulation trends in the last three decades. We have to keep in mind that in comparison to simulated trends the observed trend has a lower signal to noise ratio due to the shorter time period and a stronger influence of natural variability as it is only one realization, whereas the CMIP MMEns includes many realizations. Thus the observed trends are much more uncertain and contain a larger fraction of natural variability than the CMIP MMEns.

The trend pattern over the Pacific for the period 1979 until 2012 is mostly the opposite of the CMIP trend pattern (compare Fig. 4.13a with Fig. 4.2c,d), thus shows a westward shift of the western edge and a strengthening of the Walker Circulation (see also Fig. 4.13c). The trend is roughly 10 times larger than in the CMIP MMEns and the pattern has again a high correlation with the dominant mode of variability (-0.70), thus indicating that the Walker Circulation shifted towards more La-Nina-like conditions in the recent decade. As in the CMIP models, the trend of EOF-1 can explain 49% of the trend over the entire tropics and even 75% over the Pacific (Fig. 4.13b). The residual trend shows a strong increase of convection over South America in the last decades. From the time series of EOF-1 of zonal stream function in Fig. 4.13d we can see that there was a strong inter-decadal fluctuation of ENSO in the last decades, with more and stronger El Nino's in the time period 1979 till 1998 and more and stronger La Nina's in the time period 1999 till 2012, as also stated in *Kosaka and Xie* (2013). Thus, although the sign of the trends in reanalysis data is opposite to that of the simulated global warming trend in the CMIP models, the trend of the dominant mode of variability again plays a crucial role for the trend in the Walker Circulation.

4.8 Relation of Stream function and SLP

An open question is the relation of our results based on zonal stream function to the results of previous studies using SLP. Figure 4.14 shows the meridional average (5°S-5°N) of SLP and

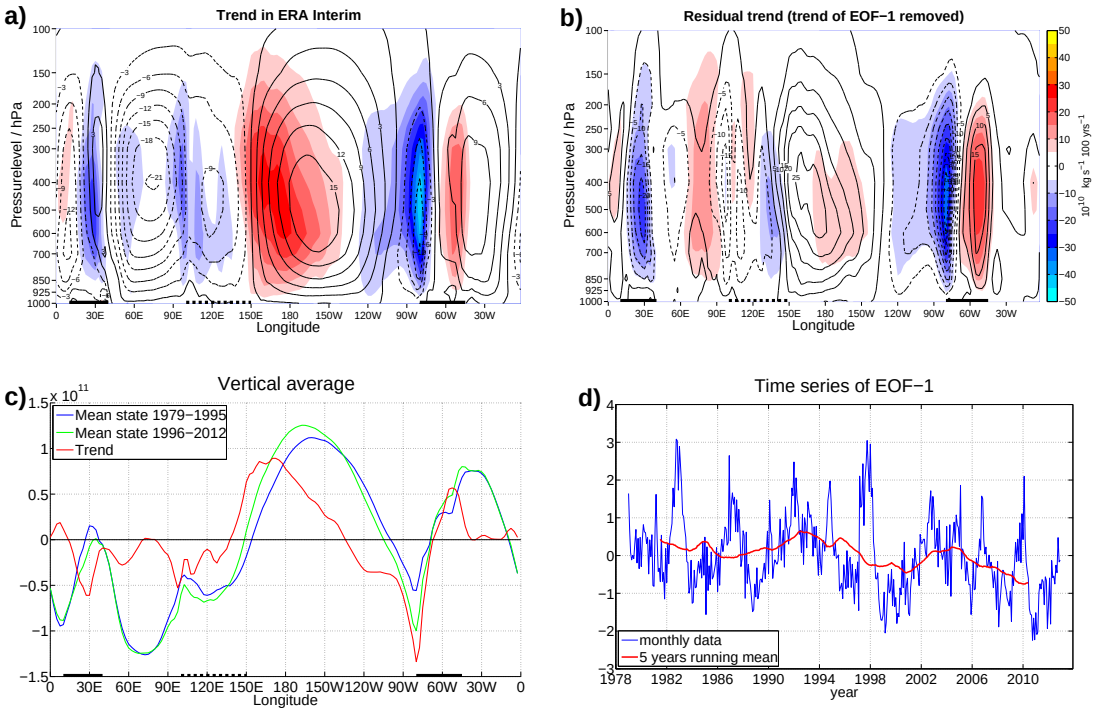

Figure 4.13: *(a) Same as Fig. 4.2c, but here the trend in ERA Interim over the period 1979 to 2012, and mean state of ERA Interim over this period as contours; (b) shading: the residual trend in ERA Interim after removing trend of EOF-1, contours: the trend of (a); (c) same as Fig. 2e, but here for mean state (in kg s^{-1}) and trend (in kg s^{-1} $(50yr)^{-1}$) in ERA Interim, (d) time series of EOF-1 of zonal stream function in ERA Interim.*

vertical wind at the 500 hPa level, the vertical and meridional mean of tropospheric temperature (T_{tropos}) and the zonal gradient of vertical und meridional averaged zonal stream function in the CMIP5 MMEns. For a better comparison we removed the area means for SLP and T_{tropos} and all variables are normalised.

In the mean state (Fig. 4.14a) we see a good agreement between all four variables: Convection takes place were the temperatures are high (the three 'heat sources' Africa, Maritime Continent and South America), SLP is low and the stream function gradients are large. However, this general agreement is not seen in the changes 21C-20C (Fig. 4.14b). The change in vertical wind again agrees with the zonal gradient of the zonal stream function (correlation 0.74) and the T_{tropos} and SLP response are very similar (correlation -0.94), as already found in *Bayr and Dommenget* (2013a). But over most regions the changes in stream function and vertical wind do not agree with the changes in SLP and T_{tropos}, especially over Africa and South America. Here the land-sea warming contrast reduces the SLP according to *Bayr and Dommenget* (2013a), which would suggest an increase in convection. In contrast, the vertical wind and the stream function show more descending. There is no explanation for this discrepancy yet, but it indicates that changes in SLP cannot reveal the full picture of changes over the entire troposphere, like convection and associated precipitation patterns. Further investigations are needed to better understand what causes these discrepancies.

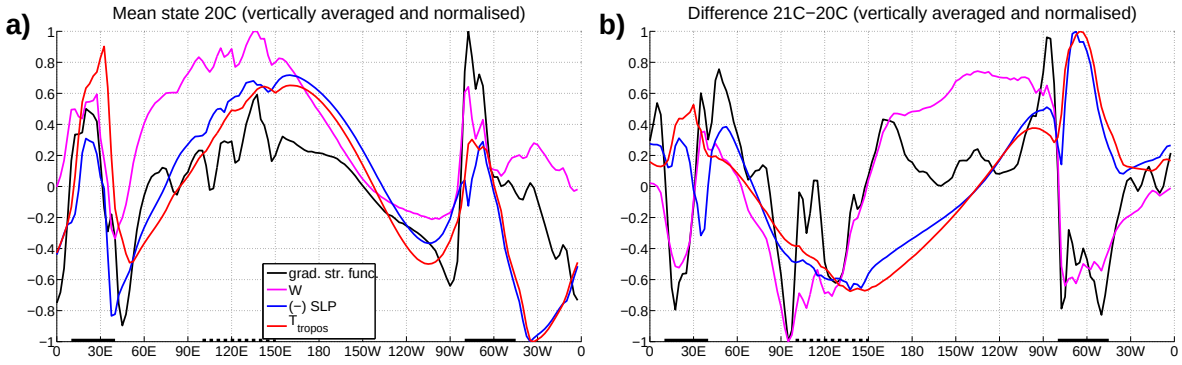

Figure 4.14: *Meridional average (5S-5N) of SLP and vertical wind (W) at the 500 hPa level, the vertical and meridional mean of tropospheric temperature (T_{tropos}, as defined in Bayr and Dommenget, 2013a) and the zonal gradient of vertical und meridional averaged zonal stream function in the CMIP5 MMEns, area mean for SLP and T_{tropos} removed and all variables are normalised; (a) mean state in 20C, (b) difference 21C − 20C.*

4.9 Summary and discussion

The main purpose of this study was to analyze the response of the zonal circulation cells (with a special focus on the Walker Circulation) to global warming and its relation to ENSO in the latest databases of state of the art climate models. The focus was on the eastward shift of the Walker Circulation and the changes in the modes of variability. We chose the zonal stream function for this analysis, as it is a direct representation of the zonal circulation and also available over all levels of the troposphere. We found that the trend patterns of the zonal circulation in global warming (Fig. 4.2c,d) are very similar in the two CMIP MMEns, despite the differences in models, resolution, ensemble size and emission scenario. This underlines the robustness of the signal, although the differences between the individual models are quite large. The trend pattern shows more ascending over the West Indic, Central and East Pacific, and more descending over the three main convection regions Africa, the Maritime Continent and South America, thus a weakening of the zonal circulations. Additionally we could show that the CMIP MMEns predict a substantial eastward shift of the western part of the Walker cell, by 6° in CMIP5 MMEns and 8° in the CMIP3 MMEns.

In the MMEns we have seen that the trend pattern has some similarities with ENSO associated variability of the zonal stream function. Indeed a large part of the global warming response corresponds to a shift towards more El-Nino-like conditions. The El-Nino-like trend in zonal stream function will cause that neutral ENSO conditions at the end of the 21st century will be El Nino conditions, if referred to the 20th century climate. How El-Nino-like the global warming trend is in comparison with an average El Nino can be calculated: An average El Nino in the CMIP5 MMEns is associated with an amplitude of $-3.6 * 10^{-10} kg\ s^{-1}$ in the box (120°E-180°, 700-300hPa) as defined for Fig. 4.4 and an eastward shift of 25° longitude. Thus a global warming trend of the same size would mean a 100% shift towards an average El Nino, with 20th century as reference climate. The eastward shift of 6° and the trend of $-1.1 * 10^{10} kg\ s^{-1} (100 yr^{-1})$ in the CMIP5 MMEns in this box (Fig. 4.4) would thus mean a long-term shift of 30% in amplitude and 26% in location towards an average El Nino event over the next century (31% and 37% in CMIP3, respectively).

Further we could show that the internal variability of the zonal stream function exhibits a substantial spatial non-linearity, as the El Nino anomaly pattern of the zonal stream function is more in the east than the La Nina anomaly pattern. The spatial non-linearity in the zonal stream function is linear related to the non-linearity of ENSO in SST in the individual models. However, most models have problems in simulating a realistic ENSO non-linearity in both variables, subsequently the non-linearity of the CMIP MMEns is less than half as strong as in the ERA Interim reanalysis data.

The similarity of the eastward shift in the zonal stream function during global warming and strong El Nino events may indicate a common forcing mechanism for these shifts. Several studies have shown that the ENSO non-linearity is caused by the atmospheric response to SST anomalies (*Kang*, 2002; *Philip and van Oldenborgh*, 2009; *Frauen and Dommenget*, 2010), in particular the eastward shift of strong El Nino events (*Dommenget et al.*, 2013). Thus the atmosphere responds with an eastward shift to SST warming. In global warming the enhanced hydrological cycle to first order leads to a horizontally homogenous but vertically enhanced warming. This warming trend is also associated with an eastward shift, indicating that horizontally homogenous and vertically enhanced warming patterns, as in both global warming trend and during El Nino, may induce an eastward shift of the zonal circulation cell over the Pacific.

The prominent changes in the modes of variability in global warming are an eastward shift from the Indian Ocean to the central Pacific of EOF-1 and a shift towards larger scale variability. EOF-1 is associated with ENSO variability and has a positive (El-Nino-like) trend in global warming. After removing the trend associated with EOF-1, two third of the trends vanishes over the Pacific, i.e. are related to more El-Nino-like conditions.

The spread in the response of the individual models is quite large. Most of the individual climate models predict a weakening and an eastward shift of the Walker cell in global warming, but some models show no significant trends and some even predict a strengthening and westward shift. This indicates that the homogeneous warming, which can only weaken the Walker cell in a warmer climate, can't be the dominant mechanism in all climate models. The inhomogeneous warming must be the dominant mechanism in the models with a strengthening Walker cell, as this mechanism can act in general to both weaken or strengthen the Walker Circulation.

In ERA Interim reanalysis data we found a strengthening of the Walker Circulation and westward shift over the last three decades. In recent literature there is a debate about the changes of the Walker Circulation over the last decades: Analysing observations and model runs forced with observed SST and/or greenhouse gas concentrations the studies of *Sohn and Park* (2010), *Meng et al.* (2011), *Luo et al.* (2012) and *L'Heureux et al.* (2013) found a strengthening of the Walker Circulation. These studies explain the strengthening with a more La-Nina-like SST warming or a stronger warming over the Indian Ocean than over the Pacific over the last decades. But several other studies found a weakening of the Walker Circulation (*Vecchi et al.*, 2006; *Power and Kociuba*, 2010; *Yu and Zwiers*, 2010; *Tokinaga et al.*, 2012a,b; *DiNezio et al.*, 2013), caused by the pure atmospheric mechanism mentioned in the introduction. A recent study form *Solomon and Newman* (2012) found out that there are large discrepancies in the SST trends over the Indo-Pacific in the different observed data sets, which are caused by different representations of El Nino in these observed datasets. A second problem is the distinction between externally forced trends and internal variability in relative short records, so that *Power and Kociuba* (2011) conclude, that external forcing accounts for 30-70% of the ob-

served Walker Circulation changes, with internal variability making up the rest. To sum up: due to relative short records we cannot definitely say if the trend in ERA Interim reanalysis data is really a global warming trend or if it is just natural variability or even just a measure uncertainty.

With the opposite direction between the predicted trend in the CMIP MMEns and the trends of the recent decades in ERA Interim, there are two conclusions possible: One conclusion could be that the trend in ERA Interim is due to increased greenhouse gases and the CMIP MMEns predict the wrong sign of ENSO response. The other conclusion is that the trends in ERA Interim are just natural decadal variations of ENSO variability and that in global warming the Walker Circulation will weaken and shift eastward, as the CMIP models predict. We think this is quite likely, as both CMIP MMEns predict it and the dominant mode of variability exhibits strong decadal trends in Fig. 4.11. Nevertheless, both possible conclusions have one important thing in common: a large part of the Walker Circulation trend follows a pre-existing mode of variability, thus can be described as more El-Nino-like or more La-Nina-like. We have to keep in mind that the ENSO response of the climate models in global warming is still quite uncertain (e.g. *Latif and Keenlyside*, 2009), but the MMEns of climate models calculated for the IPCC AR5 predict an more El-Nino-like response and therefore a weakening and eastward shift of the Walker Circulation in future climate.

Acknowledgements

We acknowledge the World Climate Research Programme's Working Group on Coupled Modeling and the individual modeling groups of the Climate Model Intercomparison Project (CMIP3 and CMIP5). This work was supported by the Deutsche Forschungsgemeinschaft (DFG) through project DO1038/5-1, the ARC Centre of Excellence in Climate System Science (CE110001028), the RACE Project of BMBF and the NACLIM Project of the European Union.

Chapter 5

Summary

In this work the changes of the tropical atmospheric circulation under global warming were addressed and the main achievements are:

In chapter 2 an explanation for the largest part of the large scale SLP changes in CMIP3 models under global warming is found:

- Tropical SLP changes are strongly linked to inhomogeneous tropospheric temperature changes (stronger than to (sea) surface temperature), also in the seasonal cycle.
- The predicted inhomogeneous tropospheric warming is ten times smaller than the homogeneous warming. In most CMIP3 models it is mainly caused by the land-sea warming contrast. Thus the troposphere warms strongest over South America and Africa and weakest over the Indo-Pacific region.
- The SLP trends are mostly opposite to the inhomogeneous T_{tropos} warming. A simple physical model is presented that can explain the largest part of the SLP trends under global warming with the inhomogeneous T_{tropos} trends.
- Sensitivity experiments with the ECHAM5 AGCM support our finding that land-sea warming contrast is an important driver of tropical SLP changes under global warming.
- The trends in ERA Interim over the period from 1989 until 2010 show the same strong relationship between SLP and T_{tropos}, but the land-sea contrast is not imprinted in both trend patterns. From this short time record it cannot be determined what part of this trend is due to natural variability and what part is due to climate change.

In chapter 3 the DEOF method is introduced, which allows the detection of changes in the spatial patterns of variability on the basis of EOF-modes:

- This method can be used to compare all modes of variability from climate models with observations or from past climate with future climate.
- This method has two features: The projected explained variances reveal which EOF-modes are most distinct in the two datasets in terms of explained variance. The DEOF patterns are the patterns that have the largest difference in explained variance in the two datasets.

- In well-defined artificial examples it was shown how an intensification, a shift or a multivariate difference can be revealed with the DEOF analysis.
- DEOF analysis is able to reproduce results for literature examples: The northeastward shift of the NAO and the poleward shift of SAM under global warming. Further DEOF analysis revealed small scale changes in the modes of variability where previous studies could not: an eastward shift of the dominant mode of surface temperature in the Northern Hemisphere, an intensification of the PDO and a multivariate change in tropical precipitation.

In chapter 4 the response in mean state and variability of the zonal circulation cells in CMIP3 and CMIP5 MMEns are discussed on the basis of the zonal stream function:

- The trend patterns of the CMIP3 and CMIP5 MMEns show both a weakening of the zonal circulation cells and an eastward shift of the Walker Circulation under global warming.
- The trend patterns have some similarities with the pattern of ENSO associated variability in zonal stream function. Roughly two third of the Walker Circulation trend can be explained by a shift towards El-Nino-like conditions. Compared to the 20th century climate, neutral ENSO conditions at the end of the 21st century correspond to El Nino conditions, with roughly one quarter of the amplitude and eastward shift of an average El Nino.
- ENSO associated variability in zonal stream function exhibits a spatial non-linearity over the Maritime Continent and the West Pacific. Most of the individual climate models have problems to reproduce this non-linearity. A linear relation between the non-linearity of ENSO variability in the zonal stream function and SST could be found: models that tend to have a strong non-linearity in the ENSO associated variability in the zonal stream function also tend to have a strong non-linearity in ENSO associated SST variability.
- The dominant mode of variability shifts eastward under global warming, consistent with the non-linearity of ENSO variability and the El-Nino-like trend.
- These results spread among individual models, but the CMIP3 and CMIP5 MMEns show in nearly all aspects very similar results, despite differences in models, resolution, ensemble size and emission scenarios, which underlines the robustness of these results.
- ERA Interim shows a westward shift and strengthening of the Walker Circulation over the last three decades, contrary to what the CMIP3 and CMIP5 MMEns predict. Three quarter of the trend of the Walker Circulation can be explained by a long-term trend in the dominant mode of variability, but here towards more La-Nina-like conditions.

Author Contributions

The author contributions to the main chapters 2, 3 and 4 are the following:
Tobias Bayr performed all analysis, figures and wrote the manuscripts.
Dietmar Dommenget contributed with ideas and discussions on the analysis, and comments on the manuscripts.
Thomas Martin also contributed to chapter 4 with ideas and discussions on the analysis, and comments on the manuscript.

List of Figures

List of Tables

Bibliography

Bala, G., K. Caldeira, R. Nemani, L. Cao, G. Ban-Weiss, and H.-J. Shin (2011), Albedo enhancement of marine clouds to counteract global warming: impacts on the hydrological cycle, *Climate dynamics*, *37*(5-6), 915–931.

Bayr, T., and D. Dommenget (2013a), The Tropospheric Land–Sea Warming Contrast as the Driver of Tropical Sea Level Pressure Changes, *Journal of Climate*, *26*(4), 1387–1402, doi: 10.1175/JCLI-D-11-00731.1.

Bayr, T., and D. Dommenget (2013b), Comparing the spatial structure of variability in two datasets against each other on the basis of EOF-modes, *Climate Dynamics*, doi:10.1007/s00382-013-1708-x.

Bengtsson, L., and K. I. Hodges (2009), On the evaluation of temperature trends in the tropical troposphere, *Climate Dynamics*, *36*(3-4), 419–430, doi:10.1007/s00382-009-0680-y.

Bjerknes, V., R. Rubenson, and A. Lindstedt (1898), Über einen Hydrodynamischen Fundamentalsatz und seine Anwendung besonders auf die Mechanik der Atmosphäre und des Weltmeeres, *Kongl. Sven. Vetenskaps Academiens Handlinger*, *31*, 1–35.

Bretherton, C., M. Widmann, V. Dymnikov, J. M. Wallace, and I. Bladé (1999), The effective number of spatial degrees of freedom of a time-varying field, *Journal of Climate*, *12*(7), 1990–2009.

Chung, C. T. Y., S. B. Power, J. M. Arblaster, H. a. Rashid, and G. L. Roff (2013), Nonlinear precipitation response to El Niño and global warming in the Indo-Pacific, *Climate Dynamics*, doi:10.1007/s00382-013-1892-8.

Clement, A. C., R. Seager, M. A. Cane, and S. E. Zebiak (1996), An ocean dynamical thermostat, *Journal of Climate*, *9*(9), 2190–2196.

DiNezio, P. N., A. C. Clement, G. A. Vecchi, B. J. Soden, B. P. Kirtman, and S.-K. Lee (2009), Climate Response of the Equatorial Pacific to Global Warming, *Journal of Climate*, *22*(18), 4873–4892, doi:10.1175/2009JCLI2982.1.

DiNezio, P. N., A. Clement, G. a. Vecchi, B. Soden, a. J. Broccoli, B. L. Otto-Bliesner, and P. Braconnot (2011), The response of the Walker circulation to Last Glacial Maximum forcing: Implications for detection in proxies, *Paleoceanography*, *26*(3), n/a–n/a, doi: 10.1029/2010PA002083.

DiNezio, P. N., G. a. Vecchi, and A. C. Clement (2013), Detectability of Changes in the Walker Circulation in Response to Global Warming, *Journal of Climate*, p. 130114154537002, doi:10.1175/JCLI-D-12-00531.1.

Dommenget, D. (2007), Evaluating EOF modes against a stochastic null hypothesis, *Climate Dynamics*, *28*(5), 517–531.

Dommenget, D. (2009), The Ocean's Role in Continental Climate Variability and Change, *Journal of Climate*, *22*(18), 4939–4952, doi:10.1175/2009JCLI2778.1.

Dommenget, D., and J. Flöter (2011), Conceptual understanding of climate change with a globally resolved energy balance model, *Climate Dynamics*, pp. 1–23–23, doi:10.1007/s00382-011-1026-0.

Dommenget, D., and M. Latif (2002), A Cautionary Note on the Interpretation of EOFs., *Journal of Climate*, *15*(2), 216–225.

Dommenget, D., T. Bayr, and C. Frauen (2013), Analysis of the non-linearity in the pattern and time evolution of El Niño southern oscillation, *Climate Dynamics*, *40*(11-12), 2825–2847, doi:10.1007/s00382-012-1475-0.

Flohn, H. (1975), Tropische Zirkulationsformen im Lichte der Satellitenaufnahmen, *Bonner Meteorologische Abhandlungen*, *21*, 1–82.

Frauen, C., and D. Dommenget (2010), El Niño and La Niña amplitude asymmetry caused by atmospheric feedbacks, *Geophysical Research Letters*, *37*(18), L18,801, doi:10.1029/2010GL044444.

Furtado, J. C., E. Di Lorenzo, N. Schneider, and N. A. Bond (2011), North Pacific Decadal Variability and Climate Change in the IPCC AR4 Models, *Journal of Climate*, *24*(12), 3049–3067, doi:10.1175/2010JCLI3584.1.

Galton, F. (1907), Vox Populi, *Nature*, *75*(1949), 450–451, doi:10.1038/075450a0.

Gill, A. E. (1980), Some simple solutions for heat-induced tropical circulation, *Quarterly Journal of the Royal Meteorological Society*, *106*(449), 447–462, doi:10.1002/qj.49710644905.

Held, I. (1993), Large-scale dynamics and global warming, *Bulletin of the American Meteorological Society*, *74*(2), 228–241.

Held, I. M., and B. J. Soden (2006), Robust responses of the hydrological cycle to global warming, *Journal of Climate*, *19*(11), 5686–5699, doi:10.1175/JCLI3990.1.

Hoerling, M. P., A. Kumar, and M. Zhong (1997), El Niño, La Niña, and the Nonlinearity of Their Teleconnections, *Journal of Climate*, *10*(8), 1769–1786, doi:10.1175/1520-0442(1997)010<1769:ENOLNA>2.0.CO;2.

Hu, Z., and Z. Wu (2004), The intensification and shift of the annual North Atlantic Oscillation in a global warming scenario simulation, *Tellus A*, *56A*(2), 112–124.

Hu, Z., M. Latif, and E. Roeckner (2000), Intensified Asian summer monsoon and its variability in a coupled model forced by increasing greenhouse gas concentrations, *Geophysical Research*, *27*(17), 2681–2684.

Hu, Z.-Z., A. Kumar, B. Jha, and B. Huang (2012), An Analysis of Forced and Internal Variability in a Warmer Climate in CCSM3, *Journal of Climate*, *25*(7), 2356–2373.

Hurrell, J. W., and H. V. Loon (1997), Decadal variations in climate associated with the North Atlantic Oscillation, *Climatic change*, *36*(3-4), 301–326.

Jolliffe, I. (2002), *Principal component analysis*, 2nd edn ed., 354–363 pp., Springer, New York.

Joshi, M. M., J. M. Gregory, M. J. Webb, D. M. H. Sexton, and T. C. Johns (2008), Mechanisms for the land/sea warming contrast exhibited by simulations of climate change, *Climate Dynamics*, *30*(5), 455–465, doi:10.1007/s00382-007-0306-1.

Kang, I.-S. (2002), El Niño and La Niña sea surface temperature anomalies: Asymmetry characteristics associated with their wind stress anomalies, *Journal of Geophysical Research*, *107*(D19), 4372, doi:10.1029/2001JD000393.

Keeley, S. P. E., M. Collins, and A. J. Thorpe (2008), Northern hemisphere winter atmospheric climate: modes of natural variability and climate change, *Climate Dynamics*, *31*(2-3), 195–211, doi:10.1007/s00382-007-0346-6.

Kidston, J., S. M. Dean, J. A. Renwick, and G. K. Vallis (2010), A robust increase in the eddy length scale in the simulation of future climates, *Geophysical Research Letters*, *37*(3), 1–4, doi:10.1029/2009GL041615.

Knutson, T. R., and S. Manabe (1995), Time-Mean Response over the Tropical Pacific to Increased C0 2 in a Coupled Ocean-Atmosphere Model, *Journal of Climate*, *8*(9), 2181–2199, doi:10.1175/1520-0442(1995)008<2181:TMROTT>2.0.CO;2.

Kosaka, Y., and S.-P. Xie (2013), Recent global-warming hiatus tied to equatorial Pacific surface cooling, *Nature*, *advance on*, doi:10.1038/nature12534.

Krueger, A. F., and J. S. Winston (1974), A Comparison of the Flow Over the Tropics During Two Contrasting Circulation Regimes, *Journal of the Atmospheric Sciences*, *31*(2), 358–370, doi:10.1175/1520-0469(1974)031<0358:ACOTFO>2.0.CO;2.

Krzanowski, W. J. (1979), Between-Groups Comparison of Principal Components, *Journal of the American Statistical Association*, *74*(367), 703–707, doi:10.1080/01621459.1979.10481674.

Kuzmina, S. I. (2005), The North Atlantic Oscillation and greenhouse-gas forcing, *Geophysical Research Letters*, *32*(4), 1–4, doi:10.1029/2004GL021064.

Latif, M., and N. S. Keenlyside (2009), El Niño/Southern Oscillation response to global warming, *Proceedings of the National Academy of Sciences*, *106*(49), 20,578–20,583.

Luo, J.-J., W. Sasaki, and Y. Masumoto (2012), Indian Ocean warming modulates Pacific climate change, *Proceedings of the National Academy of Sciences*, (i), doi:10.1073/pnas.1210239109.

L'Heureux, M. L., S. Lee, and B. Lyon (2013), Recent multidecadal strengthening of the Walker circulation across the tropical Pacific, *Nature Climate Change*, *3*(4), 1–6, doi:10.1038/nclimate1840.

Matsuno, T. (1966), Quasi-geostrophic motions in the equatorial area, *J. Meteor. Soc. Japan*, *44*(1), 25–43.

McHugh, M., and J. Rogers (2005), Multi-model representation of the North Atlantic Oscillation in the 20th and 21st centuries, *Geophysical Research Letters*, *32*(21), 1–4, doi: 10.1029/2005GL023679.

Meehl, G. A., C. Covey, T. Delworth, M. Latif, B. McAvaney, J. F. B. Mitchell, R. J. Stouffer, and K. E. Taylor (2007a), THE WCRP CMIP3 Multimodel Dataset: A New Era in Climate Change Research, *Bulletin of the American Meteorological Society*, *88*(9), 1383, doi:10.1175/BAMS-88-9-1383.

Meehl, G. A., et al. (2007b), Global Climate Projections, in *Climate Change 2007: The Physical Science Basis. Contribution of Working Group I to the Fourth Assessment Report of the Intergovernmental Panel on Climate Change*, chap. 10, pp. 747–846, Cambridge University Press.

Meng, Q., M. Latif, W. Park, N. S. Keenlyside, V. A. Semenov, and T. Martin (2011), Twentieth century Walker Circulation change: data analysis and model experiments, *Climate Dynamics*, pp. 1–17, doi:10.1007/s00382-011-1047-8.

Miller, R. L., G. A. Schmidt, and D. T. Shindell (2006), Forced annular variations in the 20th century Intergovernmental Panel on Climate Change Fourth Assessment Report models, *Journal of Geophysical Research*, *111*(D18), 1–17, doi:10.1029/2005JD006323.

North, G. R., T. L. Bell, and R. F. Cahalan (1982), Sampling Errors in the Estimation of Empirical Orthogonal Functions, *Monthly Weather Review*, *110*(July), 699–606.

Osborn, T. J. (2004), Simulating the winter North Atlantic Oscillation: the roles of internal variability and greenhouse gas forcing, *Climate Dynamics*, *22*(6-7), 605–623, doi:10.1007/s00382-004-0405-1.

Park, W., N. S. Keenlyside, M. Latif, A. Ströh, R. Redler, E. Roeckner, and G. Madec (2009), Tropical Pacific Climate and Its Response to Global Warming in the Kiel Climate Model, *Journal of Climate*, *22*(1), 71–92, doi:10.1175/2008JCLI2261.1.

Petoukhov, V., and V. A. Semenov (2010), A link between reduced Barents-Kara sea ice and cold winter extremes over northern continents, *Journal of Geophysical Research*, *115*(D21), D21,111, doi:10.1029/2009JD013568.

Philander, S. (1990), El Niño, La Niña, and the southern oscillation, *Academic press San Diego*, *46*.

Philip, S., and G. J. van Oldenborgh (2009), Significant Atmospheric Nonlinearities in the ENSO Cycle, *Journal of Climate*, *22*(14), 4014–4028, doi:10.1175/2009JCLI2716.1.

Power, S. B., and G. Kociuba (2010), The impact of global warming on the Southern Oscillation Index, *Climate Dynamics*, *37*(9-10), 1745–1754, doi:10.1007/s00382-010-0951-7.

Power, S. B., and G. Kociuba (2011), What caused the observed 20 th century weakening of the Walker circulation?, *Journal of Climate*, p. 110629145325000, doi:10.1175/2011JCLI4101.1.

Rauthe, M., A. Hense, and H. Paeth (2004), A model intercomparison study of climate change-signals in extratropical circulation, *International Journal of Climatology*, *24*(5), 643–662.

Reichler, T., and J. Kim (2008), How Well Do Coupled Models Simulate Today's Climate?, *American Meteorological Society*, *89*(3), 303–311, doi:10.1175/BAMS-89-3-303.

Rodgers, K. B., P. Friederichs, and M. Latif (2004), Tropical Pacific Decadal Variability and Its Relation to Decadal Modulations of ENSO, *Journal of Climate*, *17*(19), 3761–3774, doi:10.1175/1520-0442(2004)017<3761:TPDVAI>2.0.CO;2.

Roeckner, E., et al. (2003), *The atmospheric general circulation model ECHAM5. PART I: Model description, Report 349*, 140 pp., Max Planck Institute for Meteorology, Hamburg, Germany.

Sengupta, S., and J. S. Boyle (1998), Using Common Principal Components for Comparing GCM Simulations, *Journal of Climate*, *11*(5), 816–830, doi:10.1175/1520-0442(1998)011<0816:UCPCFC>2.0.CO;2.

Simmons, A., S. Uppala, D. Dee, and S. Kobayashi (2007), ERA-Interim: New ECMWF reanalysis products from 1989 onwards, *ECMWF Newsletter*, *110*, 25–35.

Sohn, B. J., and S.-C. Park (2010), Strengthened tropical circulations in past three decades inferred from water vapor transport, *Journal of Geophysical Research*, *115*(D15), D15,112, doi:10.1029/2009JD013713.

Solomon, A., and M. Newman (2012), Reconciling disparate twentieth-century Indo-Pacific ocean temperature trends in the instrumental record, *Nature Climate Change*, *2*(9), 691–699, doi:10.1038/nclimate1591.

Stephenson, D. B., V. Pavan, M. Collins, M. M. Junge, and R. Quadrelli (2006), North Atlantic Oscillation response to transient greenhouse gas forcing and the impact on European winter climate: a CMIP2 multi-model assessment, *Climate Dynamics*, *27*(4), 401–420, doi:10.1007/s00382-006-0140-x.

Sutton, R., B. Dong, and J. Gregory (2007), Land/sea warming ratio in response to climate change: IPCC AR4 model results and comparison with observations, *Geophysical research letters*, *34*(2), 2701.

Taylor, K. E., R. J. Stouffer, and G. a. Meehl (2012), An Overview of CMIP5 and the Experiment Design, *Bulletin of the American Meteorological Society*, *93*(4), 485–498, doi:10.1175/BAMS-D-11-00094.1.

Thorpe, A. J., H. Volkert, and M. Ziemianski (2003), The Bjerknes' Circulation Theorem: A Historical Perspective, *Bulletin of the American Meteorological Society*, *84*(4), 471–480, doi:10.1175/BAMS-84-4-471.

Tokinaga, H., S.-P. Xie, A. Timmermann, S. McGregor, T. Ogata, H. Kubota, and Y. M. Okumura (2012a), Regional Patterns of Tropical Indo-Pacific Climate Change: Evidence of the Walker Circulation Weakening*, *Journal of Climate*, *25*(5), 1689–1710, doi:10.1175/JCLI-D-11-00263.1.

Tokinaga, H., S.-P. Xie, C. Deser, Y. Kosaka, and Y. M. Okumura (2012b), Slowdown of the Walker circulation driven by tropical Indo-Pacific warming., *Nature*, *491*(7424), 439–43, doi:10.1038/nature11576.

Vecchi, G. A., and B. J. Soden (2007), Global Warming and the Weakening of the Tropical Circulation, doi:10.1175/JCLI4258.1.

Vecchi, G. A., B. J. Soden, A. T. Wittenberg, I. M. Held, A. Leetmaa, and M. J. Harrison (2006), Weakening of tropical Pacific atmospheric circulation due to anthropogenic forcing., *Nature*, *441*(7089), 73–76, doi:10.1038/nature04744.

Vecchi, G. A., A. Clement, and B. J. Soden (2008), Examining the Tropical Pacific's Response to Global Warming, *Eos Transactions American Geophysical Union*, *89*(9), 81, doi:10.1029/2008EO090002.

Wallace, J. M., and D. S. Gutzler (1981), Teleconnections in the geopotential height field during the Northern Hemisphere winter, *Monthly Weather Review*, *109*(4), 784–812.

Yu, B., and F. W. Zwiers (2010), Changes in equatorial atmospheric zonal circulations in recent decades, *Geophysical Research Letters*, *37*(5), L05,701.

Yu, B., F. W. Zwiers, G. J. Boer, and M. F. Ting (2012), Structure and variances of equatorial zonal circulation in a multimodel ensemble, *Climate Dynamics*, doi:10.1007/s00382-012-1372-6.

Yu, J.-Y., and S. T. Kim (2011), Reversed Spatial Asymmetries between El Niño and La Niña and their Linkage to Decadal ENSO Modulation in CMIP3 Models, *Journal of Climate*, p. 110506133859050, doi:10.1175/JCLI-D-11-0024.1.

Publications

1. Dommenget, D., **Bayr, T.**, and Frauen, C. (2013), Analysis of the non-linearity in the pattern and time evolution of El Nino southern oscillation, *Climate Dynamics, 40*(11-12), 2825-2847, doi:10.1007/s00382-012-1475-0.

2. **Bayr, T.**, and Dommenget, D. (2013a), The Tropospheric Land–Sea Warming Contrast as the Driver of Tropical Sea Level Pressure Changes, *Journal of Climate, 26*(4), 1387–1402, doi:10.1175/JCLI-D-11-00731.1.

3. **Bayr, T.**, and Dommenget, D. (2013b), Comparing the spatial structure of variability in two datasets against each other on the basis of EOF-modes. *Climate Dynamics*. doi:10.1007/s00382-013-1708-x.

4. Dommenget, D., Haase, S., **Bayr, T.**, and Frauen, C. (2013), Analysis of the Slab Ocean El Nino Atmospheric Feedbacks in Observed and Simulated ENSO Dynamics, *Submitted to Climate Dynamics*.

5. **Bayr, T.**, Dommenget, D. and Martin, T. (2013), The Eastward Shift of the Walker Circulation in Global Warming and its relationship to ENSO variability, *to be submitted*.

Danksagung

Mein Dank gilt all denen, die mich im Laufe meiner Doktorarbeit unterstützt haben.

Zu allererst will ich **Dietmar Dommenget** für die sehr gute Betreuung danken, die auch über die große Entfernung zwischen Melbourne und Kiel sehr gut geklappt hat. In den vielen Diskussionen habe ich wichtige Anregungen und Ideen erhalten und er hat mir gezeigt, wie wichtig es in der Wissenschaft ist, alles, aber auch wirklich alles, kritisch zu hinterfragen. Und ich bin ihm sehr dankbar, dass er mir einen zweimonatigen Forschungsaufenthalt an der Monash Universität in Melbourne ermöglicht hat.

Vielen Dank auch an ...

... **Mojib Latif**, **Thomas Martin** und **Wonsun Park** für hilfreiche Diskussionen und die zusätzliche Betreuung hier in Kiel.

... **Martin Claus** und **Sabine Haase** für die Unterstützung bei der Aufbereitung der CMIP3 und CMIP5 Daten.

... **Jan Harlaß** für die nette Bürogemeinschaft unter dem Dach der Alten Botanik und das Korrekturlesen der Dissertation.

... **alle Mitarbeiter** der Maritimen Meteorologie für die schöne gemeinsame Zeit am GEOMAR in Kiel.

... die **Deutsche Forschungsgemeinschaft** für die Finanzierung (DO1038/5-1).

... die **Heldenreise**, **GfK** und **Meditation** für Inspiration, Ausgleich und Entspannung.

... **meine Freunde** für die Unterstützung.

Diese Arbeit wurde mit der Textverarbeitung LaTeX angefertigt.

Erklärung

Hiermit bestätige ich, dass ich die vorliegende Dissertation - abgesehen von der Beratung durch meinen Betreuer - selbstständig verfasst und keine anderen als die angegebenen Quellen und Hilfsmittel verwendet habe. Ich versichere, dass diese Arbeit noch nicht zur Erlangung eines Doktorgrades an anderer Stelle vorgelegen hat. Ich erkläre, dass die vorliegende Arbeit gemäß der Grundsätze zur Sicherung guter wissenschaftlicher Praxis der Deutschen Forschungsgemeinschaft erstellt wurde.

Kiel, September 2013

(Tobias Bayr)